Production of ground-state $^{23}Na^{40}K$ molecules in the quantum-degenerate regime

Marcel Duda

München 2022

Production of ground-state $^{23}Na^{40}K$ molecules in the quantum-degenerate regime

Dissertation
an der Fakultät für Physik
der Ludwig-Maximilians-Universität München

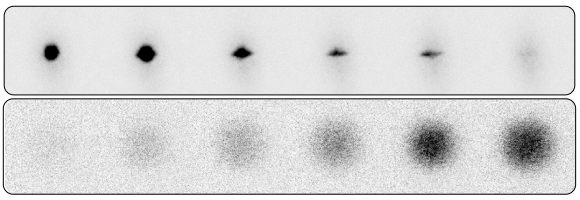

vorgelegt von

Marcel Duda

München, den 13. Juni 2022

Erstgutachter: Prof. Dr. Immanuel Bloch
Zweitgutachter: Prof. Dr. Francesco Scazza
Datum der mündlichen Prüfung: 26.07.2022

Zusammenfassung

Die Präparation und Manipulation ultrakalter atomarer Gase hat das Feld der atomaren, molekularen und optischen Physik revolutioniert. Unter der Annahme, dass ultrakalte Moleküle eine ähnliche Rolle spielen werden, wurde eine große Anstrengung unternommen, polare Moleküle mit hoher Phasenraumdichte herzustellen. Aufgrund der vielfältigen internen Struktur der Moleküle sind sie für Anwendungen in der Quantenchemie, Präzisionsspektroskopie und Quantensimulation interessant. Die Rotations- und Vibrationsfreiheitsgrade, die Moleküle so interessant machen, erschweren jedoch ihre effiziente Kühlung. Bislang führen Methoden zur direkten Kühlung von Molekülen zu Phasenraumdichten, die sechs Größenordnungen unterhalb des quantenentarteten Bereichs liegen. Im Rahmen dieser Doktorarbeit wird ein anderer Ansatz verwendet, bei dem Moleküle aus ultrakalten Atomen zusammengesetzt werden, in der Hoffnung, dass das Gas seine Entartung während der Zusammensetzung beibehält. Die Assoziation von Feshbach-Molekülen, die mit hohem Verlust und Erwärmung einhergeht, stellt die größte Limitierung bei der Herstellung entarteter Molekülgase dar.

In dieser Dissertation berichte ich über die erste Herstellung von ^{23}Na^{40}K-Grundzustandsmolekülen im quantenentarteten Regime. Dazu erzeugen wir eine Mischung aus einem Bose-Einstein-Kondensat (BEC) aus ^{23}Na-Atomen und einem entarteten Fermi-Gas aus ^{40}K-Atomen. Mithilfe einer speziesabhängigen Dipolfalle können wir die Dichten der beiden Spezies angleichen, da die Falle das Fermi gas im Vergleich zum BEC stärker komprimieren kann. Dank dieser Vorbereitung können wir die Atome aus dem BEC mit einer Effizienz von 80 % zu NaK*-Feshbach-Molekülen verbinden. Wir zeigen, dass die Produktion der Moleküle als Phasenübergang von einem polaronischen Kondensate zu einem molekularen Fermi-Gas verstanden werden kann. Unsere Methode erlaubt uns große und kalte Molekülwolken herzustellen, die hervorragende Ausgangsbedingungen für die Evaporation von Grundzustandsmolekülen bieten.

Abstract

The production and manipulation of ultracold atomic gases have revolutionized the field of atomic, molecular, and optical physics. Based on the premise that ultracold molecules will have a similar impact, with exciting applications in quantum chemistry, precision spectroscopy, and quantum simulation, several major efforts have been undertaken to reach high phase space densities of polar molecules. However, the rich internal structure that makes molecules interesting also prevents their efficient cooling. To date, methods to directly cool molecules produce molecular clouds with phase space densities that are six orders of magnitude below the quantum-degenerate regime. An alternative approach used in this Ph.D. work to producing molecular samples, is by assembling molecules from ultracold atoms with the hope that the molecules inherit the degeneracy of the atoms. However, the association of Feshbach molecules, which is accompanied by loss and heating, represents the major limitation in producing degenerate molecular samples.

In this dissertation, I report on the first production of ground-state ^{23}Na^{40}K molecules in the quantum-degenerate regime. The procedure starts with creation of a mixture of a ^{23}Na Bose–Einstein condensate (BEC) and a degenerate Fermi gas of ^{40}K atoms. To mitigate the interspecies loss during the association, which is mainly caused by the excess density of the BEC, we use a species-dependent dipole trap that confines the Fermi gas more strongly than the BEC and matches their densities. In this density-matched Bose–Fermi mixture, we can associate 80% of the atoms in the BEC into NaK* Feshbach molecules. We show that the association process can be understood as a quantum phase transition from a polaronic condensate to a Fermi gas of molecules. Ultimately, we can produce large and cold molecular samples that provide excellent starting conditions for the evaporative cooling of ground-state molecules.

List of publications

The following articles have been published in the context of this thesis:

- Roman Bause, Ming Li, Andreas Schindewolf, Xing-Yan Chen, Marcel Duda, Svetlana Kotochigova, Immanuel Bloch, and Xin-Yu Luo: *Tune-Out and Magic Wavelengths for Ground-State* ^{23}Na^{40}K *Molecules*. Physical Review Letters 125, 023201 (2020). DOI: 10.1103/PhysRevLett.125.023201

- Roman Bause, Andreas Schindewolf, Renhao Tao, Marcel Duda, Xing-Yan Chen, Goulven Quéméner, Tijs Karman, Arthur Christianen, Immanuel Bloch, and Xin-Yu Luo: *Collisions of ultracold molecules in bright and dark optical dipole traps*. Physical Review Research 3, 033013 (2021). DOI: 10.1103/PhysRevResearch.3.033013

- Roman Bause, Akira Kamijo, Xing-Yan Chen, Marcel Duda, Andreas Schindewolf, Immanuel Bloch, and Xin-Yu Luo: *Efficient conversion of closed-channel-dominated Feshbach molecules of* ^{23}Na^{40}K *to their absolute ground state*. Physical Review A 104, 043321 (2021). DOI: 10.1103/PhysRevA.104.043321

- Xing-Yan Chen, Marcel Duda, Andreas Schindewolf, Roman Bause, Immanuel Bloch, and Xinyu-Yu Luo: *Suppression of Unitary Three-body Loss in a Degenerate Bose–Fermi Mixture*. Physical Review Letters 128, 153401 (2022). https://doi.org/10.1103/PhysRevLett.128.153401

- Marcel Duda, Xing-Yan Chen, Andreas Schindewolf, Roman Bause, Jonas von Milczewski, Richard Schmidt, Immanuel Bloch, and Xin-Yu Luo: *Transition from a polaronic condensate to a degenerate Fermi gas of heteronuclear molecules*. Arxiv preprint: https://arxiv.org/abs/2111.04301

- Andreas Schindewolf, Roman Bause, Xing-Yan Chen, Marcel Duda, Tijs Karman, Immanuel Bloch, and Xin-Yu Luo: *Evaporation of microwave-shielded polar molecules to quantum degeneracy*. Arxiv preprint: https://arxiv.org/abs/2201.05143

- Marcel Duda, Xing-Yan Chen, Roman Bause, Andreas Schindewolf, Immanuel Bloch, and Xin-Yu Luo: *Long-lived fermionic Feshbach molecules with tunable p-wave interactions*. Arxiv preprint: https://arxiv.org/pdf/2202.06940.pdf

Contents

A generation of graduate students worked on these ideas but did not reach quantum degeneracy either.

—K.-K. Ni

1 The quest for degenerate polar molecules

From atoms to polar molecules

The first realization of Bose–Einstein condensation (BECs) in 1995 [1, 2] has started a new chapter in atomic, molecular and optical physics. Atomic gases were cooled to temperatures where the constituents exhibit collective properties vastly different from classical gases. Initially, the experimental effort was directed toward studying these phenomena. This includes the observation of interference between BECs [3] and studying their spatial coherence [4]. Similarly, fermionic atoms have been cooled to quantum degeneracy leading to the observation of Fermi pressure [5–7], an effect which is known to stabilize neutron stars from collapse [8]. Fermi pressure results from the intrinsic properties that fermions can occupy one specific quantum state only once.

In the following decades, the toolbox to cool, trap and manipulate atomic systems has been intensely developed. Through these technical developments, cold-atom systems have found applications in many-body physics, quantum optics, quantum information processing, and quantum simulation[1]. As a result of these advances, it has become possible to detect single atoms with near-unity efficiency [14], assemble them into three-dimensional structures [15] and design experiments that produce Bose–Einstein condensates on the international space station [16].

However, the limitation of ultracold ground-state atoms is that contact interactions dominate. Thus, the community has been looking for platforms that exhibit long-range interactions, such as highly magnetic atoms [17–20], alkali atoms that are excited into high-lying electronic states called Rydberg atoms [21], or polar molecules. Polar molecules are interesting as they offer a compromise between the two aforementioned systems: They have a considerably longer lifetime than Rydberg atoms and a markedly larger dipolar interaction than the magnetic atoms.

Moreover, polar molecules offer a rich internal structure with the additional vibrational and rotational degrees of freedom compared to atoms. Especially interesting is the dipolar interaction which arises from the rotational structure of the molecules. Many applications have been proposed for polar molecules to explore exotic quantum-matter phenomena such as p-wave superfluidity [22–24], supersolidity [25] and Wigner crystallization [26, 27], to extend Hubbard models [28], to use polar molecules for quantum information processing [29–31] and test fundamental symmetries of Nature [32]. However, the prerequisite for

[1] The list of achievements is extensive. To the interested reader, please refer to the review articles in Refs. [9–13] for more information.

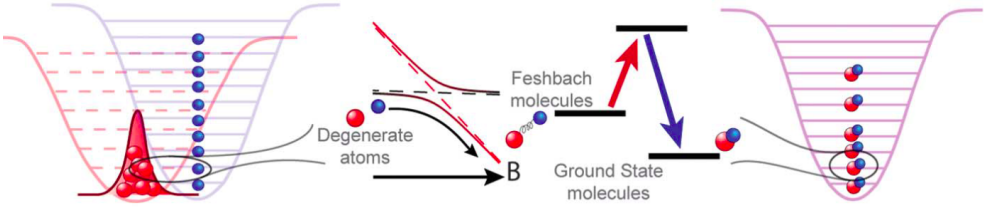

Figure 1.1 – Route towards degenerate ground-state molecules. Starting with a condensed sample of bosonic atoms (red) and a degenerate Fermi gas (blue), Feshbach molecules are associated by sweeping a magnetic field through a Feshbach resonance. The weakly bound molecules are then coherently transferred into the ground state by using STIRAP. This figure is adapted from [43].

many of these proposals is to reach the quantum-degenerate regime.

The first degenerate sample of polar molecules

First attempts to directly cool and trap molecules date back to 1998 [33, 34]. Approaches to produce cold molecular samples are, for example, by using Stark or Zeeman decelerators for molecular beams [35–39], buffer-gas cooling [40] and many others. Another approach is to do laser cooling on molecules. However, since the internal structure of the molecules is more complex than for atoms, it is also more challenging to find closed optical transitions on which laser cooling can be performed [41]. While there has been a tremendous effort in the past years to improve the laser-cooling methods for molecules, the largest phase-space density that has been reported so far for yttrium monoxide is approximately 10^{-6} [42], still six orders of magnitude away from reaching degeneracy.

Another approach to producing polar molecules is to associate two different species of ultracold atoms. Whereas trapping alkali atoms and cooling them into the deeply degenerate regimes is established, the association process into molecules is the main challenge of this approach. In the seminal work by Ni *et al.* [44], the authors managed to produce a sample of 3×10^4 ^{40}K^{87}Rb molecules at a temperature of $T = 350\,\mathrm{nK}$. The approach relies on creating weakly bound Feshbach molecules which are then transferred into the rotational, vibrational and electronic (rovibronic) ground state by Stimulated Raman Adiabatic Passage (STIRAP). This tremendous success improved the phase space density by 11 orders of magnitude compared to previous results. Still, due to Feshbach association efficiencies of $10-15\%$, one to two orders of magnitude were still missing to enter the degenerate regime.

Stimulated by this first success and quantum degeneracy within reach, many different groups attempted a similar route to produce bialkali molecules in the rovibronic ground state, including species like ^{87}Rb^{133}Cs [45, 46], ^{23}Na^{40}K [47–49], ^{23}Na^{87}Rb [50], ^{23}Na^{6}Li [51], ^{23}Na^{39}K [52] and ^{23}Na^{133}Cs [53, 54]. However, one of the bottlenecks in all of these systems is the association of weakly bound Feshbach molecules. While reasonably efficient for thermal gases, the association becomes considerably worse when the atoms are degenerate. This was particularly shown in Bose–Fermi mixtures [55]. A sort of "conventional

wisdom", as Kang-Kuen Ni calls it in her article [56], got established that degenerate bosons and fermions cannot be associated, which was backed up by the experimental observations [57, 58]. This was attributed to the fact that the overlap of Bose–Fermi mixtures in phase space, which becomes worse when the mixture is degenerate, dictates the association efficiency. To overcome the low association efficiency accompanied by strong particle loss, association in optical lattices [59, 60] was attempted. The hope was that inelastic collisions would be under control by only loading one atom of each species into a lattice site. The challenge in this approach is to ensure a high filling of the lattice for both species. Ultimately, this approach has not yet produced degenerate molecular samples.

A decade after the production of ground-state ^{40}K^{87}Rb molecules, the team led by Jun Ye at JILA produced a degenerate sample of ground-state molecules [43]. Using a small but pure BEC of Rb atoms and a Fermi gas of K atoms, the authors associated half of the bosons into KRb* Feshbach molecules before transferring them into the rovibronic ground state. Still, many questions concerning the nature of the association are not answered. What are the limiting factors in the association? How can this procedure be adopted, given that no other experiment succeeded in producing degenerate molecules thereafter? How can the association from the BEC be efficient when previous experiments considered it to be impossible?

This thesis

This thesis describes how to associate a degenerate sample of molecules from double-degenerate Bose–Fermi mixtures. We show that the limitation of the Feshbach association is the mismatch of the densities between the bosons and the fermions, where in particular, the excess density of the BEC leads to strong interspecies loss. We solve this problem by employing a dipole trap that matches the densities of the species leading to the efficient association of Feshbach molecules. By observing the molecule-formation process, we clearly show that atoms from the BEC can bind with the atoms from the Fermi gas to produce molecules. Moreover, we show that this process can be understood in a quantum many-body framework, where the bosons and the fermions mutually interact, build up pairing correlations and form molecules. Our measurements provide strong evidence for a quantum phase transition from a polaronic phase to a molecular phase closely related to the polaron-to-molecule transition in the Fermi-polaron problem.

The thesis is structured as follows: Chapter 2 contains fundamental concepts of scattering theory and explains how resonant scattering behavior leads to tunable interactions between atoms and the emergence of molecular bound states. After introducing important quantities for trapped Bose and Fermi gases, I will discuss mixtures of interacting bosons and fermions. The description of the experimental setup can be found in Chapter 3, with an overview of the experimental sequence and specific methods and upgrades relevant to this work. In particular, I will discuss the characterization of the Feshbach resonance at 78.3 G which we use for the association of weakly bound molecules. Since inelastic collisions represent a significant limitation to reaching quantum degeneracy in our system, the measurements of various loss processes around the 78.3-G Feshbach resonance are presented in Chapter 4. This in-

cludes atomic three-body loss, inelastic collisions between Feshbach molecules and atoms, and inelastic collisions between Feshbach molecules. In addition, I will present measurements of elastic collisions between Feshbach molecules, which were observed for the first time during this Ph.D. work. In Chapter 5, I will guide the reader through the steps to successfully associate Feshbach molecules in double-degenerate Bose–Fermi mixtures. I will show that the Feshbach association can efficiently convert atoms into molecules in thermal mixtures by ramping the magnetic field through a Feshbach resonance. I will then focus on the association in double-degenerate Bose–Fermi mixtures showing that efficient creation of NaK^* molecules necessitates density-matched Bose–Fermi mixtures at low densities. I will then discuss the characterization of the Fermi degeneracy of Feshbach and ground-state molecules, especially when the molecules are noninteracting and can undergo loss. The interpretation of the efficient association of Feshbach molecules in terms of a quantum phase transition from a polaronic phase to a molecular phase, where the condensate fraction is the order parameter, is presented in Chapter 6. Specifically, I will show how the order parameter as a function of the interaction strength remarkably agrees with theoretical calculations supporting the scenario of a quantum phase transition from a polaronic condensate to a degenerate Fermi gas of molecules.

2 Interacting Bose–Fermi mixtures

2.1 Atomic interactions: The Good, the Bad and the Tunable

Gases of neutral atoms are far more interesting than ideal gases, whose constituents are treated as noninteracting point-like particles. Atoms interact with each other through scattering processes, where the interatomic potential is often described as a Lennard–Jones-type potential of the following form

$$V_{\mathrm{LJ}}(r) = \frac{C_{12}}{r^{12}} - \frac{C_6}{r^6} \tag{2.1}$$

with the coefficients C_{12} and C_6. The first term describes a strong repulsion at short interatomic distances r, when the electronic orbitals of atoms overlap. The second term is the van der Waals potential which comes from a small dipole moment that is mutually induced by the approaching atoms.

Scattering processes can be elastic, leading to a redistribution of kinetic energies. These are often considered "good" collisions because they are useful for evaporative cooling of ultracold atomic gases. Collisions can also be inelastic where the *overall* kinetic energy of the of the particles before and after the collision is altered. Inelastic collision processes require the existence of multiple collision channels, as realized for two colliding atoms that change their hyperfine states due to the collision. For trapped atomic gases, inelastic collisions are typically considered "bad" as the additional kinetic energy leads to the loss of the atoms from the trap. However, when multiple collision channels are involved, resonant scattering is possible when the energies of the collision channels energetically approach each other. These so-called Feshbach resonances allow to tune the interactions between the atoms and enable the binding of the atoms into molecules. Before discussing the case of these resonant collisions, we consider the case of two particles interacting in elastic collisions.

2.1.1 Scattering in a central potential

The problem of two scattering particles can be solved in the in the center-of-mass frame. To this end, we consider an incoming plane wave with a relative wavevector $\boldsymbol{k}$ colliding with the interaction potential $V(\boldsymbol{r})$ which has a finite range. The time-independent Schrödinger equation for the relative motion can be written as

$$\left(\frac{\hbar^2\boldsymbol{k}^2}{2\mu} + V(\boldsymbol{r})\right)\Psi(\boldsymbol{r}) = E\Psi(\boldsymbol{r}), \tag{2.2}$$

where μ is the reduced mass of the colliding particles, $\Psi(\boldsymbol{r})$ is the wavefunction and E is the energy in the system. In the collision region, the structure of the wavefunction strongly depends on the nature of the potential $V(\boldsymbol{r})$, and typically the solution of this equation is therefore examined away from the collision region. When the potential $V(\boldsymbol{r})$ decays sufficiently fast with the interatomic distance like the potential in Equation (2.1), the solution of $\Psi(\boldsymbol{r})$ to Equation (2.2) can be approximated as a running wave. According to this so-called Born approximation, the scattered wavefunction can be described as a sum of a transmitted and a scattered wave written in spherical coordinates, i.e.,

$$\Psi(r,\theta,\phi) = e^{ikr\cos(\theta)} + f(k,\theta,\phi)\frac{e^{ikr}}{r}. \tag{2.3}$$

Here, we assume that the incoming wave propagates in the direction $z = r\cos(\theta)$. The proportionality with $1/r$ in the second term ensures that the total flux of energy is independent of the radius r. The scattering amplitude $f(k,\theta,\phi)$ is generally not isotropic and depends on the wavevector. Since the scattering potentials are considered to be radially symmetric, the wavefunction can be decomposed into partial waves with the spherical harmonics $Y_{l,m}(\theta,\phi)$. Moreover, due to the symmetry of the plane wave, we can further simplify the angular dependence to $Y_{l,0} = \sqrt{(2l+1)/4\pi}\,P_l(\cos(\theta))$, where $P_l(\cos(\theta))$ are the Legendre polynomials, and the scattering amplitude reduces to $f(k,\theta)$. We can therefore expand the scattering wavefunction into partial waves as

$$\Psi(\boldsymbol{r}) = \sum_{l=0}^{\infty} \frac{\Psi_l(r)}{r} P_l(\cos(\theta)), \tag{2.4}$$

The function $\Psi_l(r)$ fulfills the radial Schrödinger equation

$$-\frac{\hbar^2}{2\mu}\frac{\mathrm{d}^2\Psi_l(r)}{dr^2} + \left(\frac{\hbar^2 l(l+1)}{2\mu r^2} + V(r)\right)\Psi_l(r) = E\Psi_l(r), \tag{2.5}$$

where we identify an extra term containing the centrifugal barrier $\hbar^2 l(l+1)/2\mu r^2$.

For collisions in the ultracold regime ($k \to 0$), the dominating contribution to the collisions comes from $l = 0$ (s-wave). The terms with $l > 0$ do not contribute to the collision process as the particles reflect from the centrifugal barrier before they feel the presence of the van der Waals potential. However, when the collision involves identical fermions, the wavefunction to describe them is anti-symmetric $\Psi(\boldsymbol{r}) = -\Psi(-\boldsymbol{r})$, which limits the partial wave expansion to odd values of l. Thus, identical fermions at sufficiently small temperatures, the dominating collision channel results from p-wave collisions ($l = 1$). Due to the suppressed s-wave collisions from fermionic atoms, evaporatively cooling a single fermionic species is not practical. Luckily, evaporative cooling of spin-polarized fermions can be realized with a coolant. For example, in Bose–Fermi mixtures, the fermions can be sympathetically cooled by the bosons [61]. Experiments working only with fermions need to produce mixtures with different hyperfine states for efficient cooling [5].

For s-wave scattering, in the regime far from the collision region, the radial wavefunction

takes the form

$$\Psi_0(r) \simeq A\left(\sin(\delta_0(k)) + kr\cos(\delta_0(k))\right), \tag{2.6}$$

where $\delta_0(k)$ is the phase shift as a result of the collision which can either delay or advance the spherical wave, and the scattering amplitude near the collisional threshold $k \to 0$ is given by

$$f_0(k) \simeq \frac{-a}{1 + \mathrm{i}ka - r_{\mathrm{eff}}k^2a}, \tag{2.7}$$

where we have introduced the scattering length a as

$$a = -\lim_{k\to 0}\frac{\tan\delta_0(k)}{k}. \tag{2.8}$$

Equation (2.7) is called the effective-range expansion, where the term r_{eff} is the effective range which depends on the precise nature of the interaction potential of the colliding particles. In many cases, the effective range of the potential is considered to not be significantly contributing to the scattering process and the scattering can be described solely by scattering length.

A similar treatment of the scattering problem can be done for p-wave collisions where one solves the Schrödinger equation for $l = 1$. In this case, the Legandre polynomial $P_1(\cos(\theta)) = \cos(\theta)$ and, thus, scattering amplitude contains a dependence on θ. It can be shown that the scattering amplitude $f(k,\theta)$ is not radially symmetric anymore [62]. Instead of the scattering length a, the scattering volume $V_p(k) = a_p^3(k)$ is the relevant quantity defined as [63]

$$V_p(k) = -\lim_{k\to 0}\frac{\tan\delta_1(k)}{k^3}. \tag{2.9}$$

It might come as a surprise that in Section 4.3.2, we discuss the collisions between identical fermionic Feshbach molecules in terms of the interspecies scattering length a instead of the scattering volume. The reason is that the scattering length of the Feshbach molecules can be related to the interspecies scattering length [64], making the interspecies scattering length a convenient quantity to work with.

2.1.2 Scattering cross-section and rate coefficients

Within the framework of this thesis, we are often not concerned about the angular resolution of the collision which we obtain from the scattering amplitude, but rather the collision rate. To this end, we can define differential cross-section and the total cross-section given by

$$\frac{\mathrm{d}\sigma}{\mathrm{d}\Omega} = |f(k,\theta)|^2, \tag{2.10}$$

$$\sigma = \int |f(k,\theta)|^2 \mathrm{d}\Omega, \tag{2.11}$$

where Ω is the solid angle. For indistinguishable particles, the scattering amplitude for bosons should be replaced such that $f(k,\theta) \to f(k,\theta) + f(k,\pi-\theta)$ while for fermions it

should be replaced by $f(k,\theta) \to f(k,\theta) - f(k,\pi-\theta)$ as the scattering between two particles with the final angle θ or $\theta - \pi$ is equivalent. We can then write the scattering amplitude $f(k,\theta) = \sum_{l=0}^{\infty}(2l+1)f_l(k)[P_l(\cos(\theta)) - P_l(\cos(-\theta)]$. The general equation for the scattering cross-section for identical bosons and fermions is respectively given by

$$\sigma_B(k) = \frac{8\pi}{k^2}\sum_{\text{even}\,l}^{\infty}(2l+1)\sin^2\delta_l(k), \tag{2.12}$$

$$\sigma_F(k) = \frac{8\pi}{k^2}\sum_{\text{odd}\,l}^{\infty}(2l+1)\sin^2\delta_l(k). \tag{2.13}$$

In the low temperature limit $k \to 0$, the scattering cross-section can be written as

$$\sigma_B(k) = \frac{4g\pi a^2}{1+k^2a^2}, \tag{2.14}$$

where g accounts for the symmetrization requirements. If the two colliding particles are in different internal quantum states, $g = 1$ and if the two particles are in the same internal quantum state $g = 2$. Note that even when the scattering length diverges, Equation (2.14) will yield a finite cross-section $\sigma_B(k) = 4g\pi/k^2$.

Note that we have limited our discussion to a single-channel model, meaning that every scattering process is purely elastic. When several collision channels are involved, inelastic collisions are possible. The scattering length $\tilde{a}_\alpha(k) = \tilde{\alpha}_\alpha(k) - i\tilde{\beta}_\alpha(k)$ then becomes complex [65], and the rate coefficients of the elastic and inelastic scattering lengths are given by the diagonal elements of the S-matrix $S_{\alpha\alpha} = e^{2i\eta_\alpha}$ for channel α [66]. Hence, the scattering amplitude in Equation (2.7) without the effective range can be generalized to

$$f_\alpha(k_\alpha) = \frac{1}{1+k_\alpha^2|\tilde{a}_\alpha(k_\alpha)|^2 + 2k_\alpha\tilde{\beta}_\alpha(k_\alpha)}, \tag{2.15}$$

and the scattering length in Equation (2.8) can be written as

$$\tilde{a}_\alpha(k_\alpha) = -\frac{\tan\eta_\alpha(k_\alpha)}{k_\alpha} = \frac{1}{ik_\alpha}\frac{1-S_{\alpha\alpha}(k_\alpha)}{1+S_{\alpha\alpha}(k_\alpha)}, \tag{2.16}$$

where k_α is the wavevector in the collision channel with energy E_α. Then the rate coefficients of inelastic and elastic collisions can be written as

$$K^{\text{el}} = \frac{2ghk_\alpha}{\mu}|\tilde{a}_\alpha(k_\alpha)|^2 f_\alpha(k_\alpha), \tag{2.17}$$

$$K^{\text{inel}} = \frac{2gh}{\mu}\tilde{\beta}_\alpha(k)f_\alpha(k), \tag{2.18}$$

respectively. While a precise determination of the elastic and inelastic scattering rates depend on the interatomic scattering potential, we can write down the general scaling relations for s-wave and p-wave collisions in the ultracold temperature regime in terms of the scattering length [64, 66]. Here $K = \sigma\bar{v}$ is the rate coefficient of the collisions, where σ is the cross-

section and $\bar{v}$ is the relative velocity between the particles:

$$K_{l=0}^{\text{el}} \propto ka^2 \tag{2.19}$$

$$K_{l=1}^{\text{el}} \propto k^5 a^6 \tag{2.20}$$

$$K_{l=0}^{\text{inel}} \propto a \tag{2.21}$$

$$K_{l=1}^{\text{inel}} \propto k^2 a^3 \tag{2.22}$$

From the relation in Equations (2.19)-(2.22), we see that *s*-wave inelastic collisions do not scale with k, while the elastic collisions scale with $k \sim \sqrt{T}$, where T is the temperature of the sample. Moreover, *p*-wave collisions have a strong scaling with the temperature and the scattering length.

2.1.3 Feshbach resonances

According to the discussion in Section 2.1.1, we might get the impression that for low temperatures and *s*-wave dominated collisions, the scattering behavior of atoms is determined by the interatomic potential. However, what makes the collision behavior interesting is the coupling between different scattering states. The scattering states or scattering channels arise from the set of internal quantum numbers associated with the collision.

In a two-channel scattering model, as shown in Figure 2.1a, we define one scattering state as the open or entrance channel, which is populated before the scattering event. The other is the closed channel, which is defined to host a bound state. We assume that these states can couple to each other and that they obtain a *different* shift in energy when a magnetic field is applied (Zeeman shift). The energy E_{coll} is associated with the collision process and typically much smaller than the energy scale related to the potential of the open and the closed channel. Thus, it is possible to tune the magnetic field to the Feshbach resonance, where the bound state is resonant with the scattering state in the entrance channel. The coupling between the scattering states persists even when the two channels couple to each other off-resonantly, which modifies the scattering length of the open channel in the vicinity of the Feshbach resonance. For an isolated Feshbach resonance, the scattering length as a function of the magnetic field is given by

$$a(B) = a_{bg}\left(1 - \frac{\Delta}{B - B_0}\right), \tag{2.23}$$

where B_0 is the resonant magnetic field, Δ the width of the Feshbach resonance and a_{bg} is the background scattering length (see Figure 2.1b). The behavior described by Equation (2.23) shows that the sign and the magnitude of the scattering length can be arbitrarily changed, and far away from the resonance the scattering length approaches the background scattering length a_{bg}, which signifies the contribution to the scattering resulting from the interatomic van der Waals potential.

Moreover, as a result of the existence of the bound state, it is possible to associate two atoms into a molecule which are then called Feshbach molecules. These molecules exist

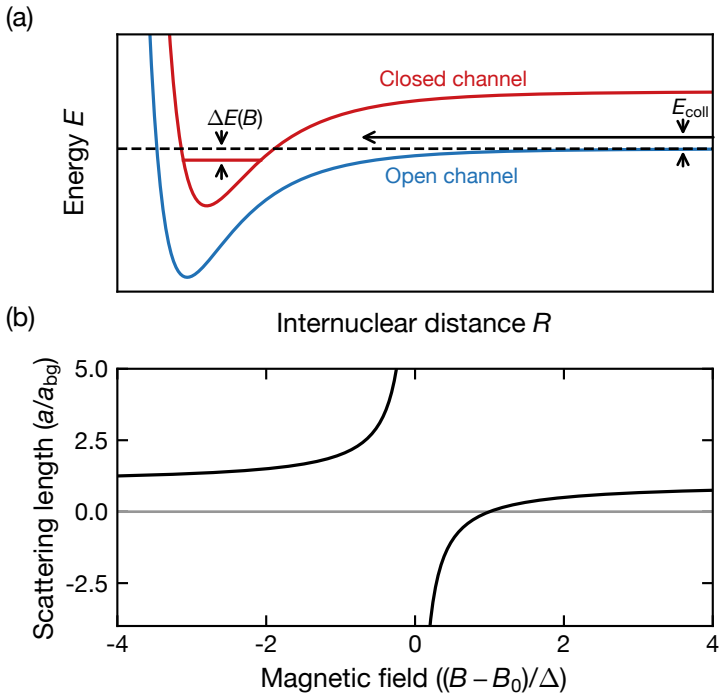

Figure 2.1 – A magnetically tunable Feshbach resonance. (a) Two-channel model. The open channel contains the entrance collisions channel and the energy E. The closed channel corresponds to a different set of quantum numbers than the open channel, and it contains a bound state. By changing the magnetic field B, the energy difference $\Delta E = E_{\text{bound}} - E_{\text{coll}}$ between the bound state and entrance collision channel can be tuned. (b) Scattering length a as function of magnetic field B. When the magnetic field is on resonance $B = B_0$, the scattering length diverges. Far from the resonance such that $|B - B_0| \gg \Delta$, the scattering length approaches the background scattering length a_{bg}.

when the scattering length $a > 0$. The binding energy close to the resonance is given by $E_b = -\hbar^2/2\mu a^2$. A few more comments on Feshbach resonances that are relevant for the upcoming chapters in this thesis:

- In the idealized two-channel model, the scattering length as a function of the magnetic field in Equation (2.23) is plotted for an isolated Feshbach resonance. In typical cold-atom systems, many scattering states can couple to the entrance channel, each resulting in a Feshbach resonance. If two Feshbach resonances are close by, the scattering length is typically described by a model of overlapping resonances as discussed in Section 3.6.

- Feshbach resonances can be divided into broad and narrow. This is characterized by $s_{\text{res}} = 0.956 R_{\text{vdW}}/R^*$. Here, R_{vdW} is the van der Waals length which is the typical length scale for the van der Waals potential. R^* is the intrinsic resonance length which is given by the different magnetic moment between the open and the closed channel [12]. It signifies how sharp the closed and the open channel intersect. We consider the Feshbach resonance to be broad for $s_{\text{res}} \gg 1$ and narrow for $s_{\text{res}} \ll 1$. For broad resonances one can safely assume that the scattering length is a good parameter to describe the resonance, which is not the case for narrow Feshbach resonances [67].

- In most of this thesis, we assume that the scattering behavior is entirely described by the scattering length. According to Equation (2.7), this approximation is valid if $kr_{\text{eff}} \ll 1$. This is typically the case in the Na-K system and breaks down only when the scattering length is close to zero. For more details on the theoretical predictions on the scattering in Na-K and the calculation of r_{eff}, see Ref. [68].

2.2 Quantum gases in harmonic traps

2.2.1 Degenerate quantum gases

The constituents of ultracold quantum gases can be unambiguously divided into bosons and fermions. In fact, every elementary or composite particle is either a fermion or a boson. Elementary or composite particle possessing an integer spin are called bosons, while particles with a half-integer spin are called fermions. The symmetrization of antisymmetrization postulate for bosons or fermions, respectively, leads to the mean occupation number of a single-particle energy eigenstate $|i\rangle$ with energy E_i given by

$$\langle n_i \rangle = \frac{1}{e^{(E_i-\mu)/k_B T} \mp 1} \equiv f(E_i), \tag{2.24}$$

where μ is the chemical potential, k_B is the Boltzmann constant, and T is the temperature of the system. For $(E_i - \mu) \gg k_B T$, which is realized when the density of the particles is low or when the temperature is high. In the thermal regime, the distributions in Equation (2.24)

approach a Maxwell-Boltzmann distribution which is given by

$$f(E_i) = e^{-(E_i-\mu)/k_BT}, \tag{2.25}$$

leading to the same distribution function for the bosons and fermions is the same. However, in the degenerate regime, which can be reached when the temperature of the gas is reduced or the density increased, the term ∓ 1 in Equation (2.24) becomes relevant, and the behavior between bosons and fermions changes. Qualitatively speaking, for degenerate bosons, the occupation of low-energy states is expected to be enhanced compared to a classical gas. In contrast, in gases with Fermi degeneracy, the occupation of lower energy states is suppressed compared to a classical gas.

One typically speaks of the degenerate regime when the interparticle distance $d = n^{-1/3}$ is comparable to the de Broglie wavelength of a particle with mass m given by

$$\lambda_{\mathrm{dB}} = \sqrt{\frac{2\pi\hbar^2}{mk_BT}}. \tag{2.26}$$

The de Broglie wavelength associates a wavelength to the particles in the context of the wave-particle duality. When the phase space density $n\lambda_{\mathrm{dB}}^3 > 1$, the waves that describe the particles overlap and interfere and the particles exhibit collective phenomena.

2.2.2 Trapped thermal gases

We consider a noninteracting Bose or Fermi gas in the thermal regime trapped in a harmonic potential. Accordingly, the Hamiltonian of a single particle of mass m, momentum $\boldsymbol{p}$ and position $\boldsymbol{r}$ can be written as

$$H(\boldsymbol{p},\boldsymbol{r}) = \frac{p_x^2+p_y^2+p_z^2}{2m} + \frac{m}{2}\left(\omega_x^2x^2+\omega_y^2y^2+\omega_z^2z^2\right). \tag{2.27}$$

Here, ω_i is the trapping frequency in the i-th direction. In order to calculate the thermodynamic quantities of the bosons in the harmonic potential, it is convenient to change from the representation of discrete energies E_i to a continuous density of energy eigenstates. This is a good approximation if the thermal energy k_BT of the system is much larger than the largest energy spacing in the harmonic potential, i.e., when $k_BT/\hbar \gg \mathrm{Max}(\omega_x,\omega_y,\omega_z)$. Hence, we can write the distribution of bosons according to their energy E and their chemical potential μ as

$$f(E) = \frac{1}{e^{(E-\mu)/k_BT}}. \tag{2.28}$$

Within the approximation, we also define the density of states as a function of the energy E [69] as

$$g(E) = \frac{E^2}{2(\hbar\bar{\omega})^3}, \tag{2.29}$$

where $\bar{\omega} = (\omega_x \omega_y \omega_z)^{1/3}$ is the geometric-mean trapping frequency. The chemical potential is implicitly fixed by the relation that integration over all energy states equals to the number of atoms, i.e.,

$$N = \int g(E) f(E) \mathrm{d}E. \tag{2.30}$$

To calculate the density and momentum distribution of the thermal gas, we combine Equation (2.27) and Equation (2.28), to rewrite the probability distribution $f(E)$ in terms of the momentum and position of the fermions $f(\boldsymbol{r}, \boldsymbol{p})$. To obtain the density distribution $n(x,y,z) = \int f(\boldsymbol{r}, \boldsymbol{p}) \mathrm{d}^3\boldsymbol{p}$, we integrate over the momenta $\boldsymbol{p}$ and obtain

$$n(x,y,z) = N \left(\frac{m\bar{\omega}^2}{2\pi k_B T} \right)^{3/2} e^{-\frac{m(\omega_x^2 x^2 + \omega_y^2 y^2 + \omega_z^2 z^2)}{2k_B T}}. \tag{2.31}$$

Similarly, we calculate the momentum distribution $n(p_x, p_y, p_z) = \int f(\boldsymbol{r}, \boldsymbol{p}) \mathrm{d}^3\boldsymbol{r}$ by integrating over the

$$n(p_x, p_y, p_z) = N \left(\frac{1}{2\pi m k_B T} \right)^{3/2} e^{-\frac{(p_x^2 + p_y^2 + p_z^2)}{2mk_B T}}. \tag{2.32}$$

2.2.3 Trapped Bose gases

We treat the system of degenerate bosons with the Hamiltonian in Equation (2.27) and the Bose distribution

$$f(E) = \frac{1}{e^{(E-\mu)/k_B T} - 1}. \tag{2.33}$$

Again, we can relate the number particles and the chemical potential according to Equation (2.30). However, this time the number of particles obtained by this procedure only accounts for the thermal bosons. With more bosons in the system the chemical potential increases until $\mu = E$, where we require that $\mu = 0$ for each additional particle that we put into the system, otherwise, the distribution in Equation (2.33) becomes negative and thus unphysical. Given a specific temperature, there is a critical particle number above which all other atoms will thus occupy the lowest energy state macroscopically, leading to the phenomena of Bose–Einstein condensation. The overall number of particles is then given by $N = N_{\mathrm{BEC}} + N_{\mathrm{th}}$, where N_{th} is the number of thermal bosons and N_{BEC} is the number of atoms in the BEC. Given a number of bosons N, we can also define a critical temperature for Bose–Einstein condensation T_c. The critical temperature for Bose–Einstein condensatation according to the geometric mean trapping frequency $\bar{\omega}$ and the total number of bosons N given by [70]

$$k_B T_c \cong 0.940 \hbar \bar{\omega} N^{1/3}. \tag{2.34}$$

For $T < T_c$, we relate T/T_c to the condensate fraction $\beta = N_{\mathrm{BEC}}/N$ according to

$$\frac{T}{T_c} = (1-\beta)^{1/3}. \tag{2.35}$$

Equation (2.35) can be used as a thermometer for partially condensed bosons. For instance, about half of the bosons are in the ground state for $T \approx 0.8T_c$.

While in absence of interactions for a pure BEC, the wavefunction of the condensate does not depend on the number of particles in the BEC [70], it changes for an interacting BEC and depends whether the interactions between the atoms are attractive of repulsive. We obtain the density of the BEC from the Gross–Pitaevskii equation

$$\left[-\frac{\hbar^2}{2m}\Delta + V(\boldsymbol{r}) + g_{BB}\, n(\boldsymbol{r}) \right] \psi(\boldsymbol{r}) = \mu\, \psi(\boldsymbol{r}), \tag{2.36}$$

where $V(\boldsymbol{r})$ is the term due to the harmonic confinement in Equation (2.27), $g_{BB} = 2\pi\hbar^2 a_{BB}/\mu_{BB}$ is the coupling parameter, a_{BB} is the boson-boson scattering length and μ_{BB} the reduced mass of the bosons. Under typical experimental conditions, the kinetic energy is much smaller the trapping potential and the boson-boson interactions. In the Thomas–Fermi approximation, where the kinetic energy of the BEC is ignored, Equation (2.36) can be solved and the density of the BEC can be described by

$$n(x,y,z) = \left(\frac{15 N_{\mathrm{BEC}}}{8\pi R_x R_y R_z} \right) \mathrm{Max}\left(1 - \frac{x^2}{R_x^2} - \frac{y^2}{R_y^2} - \frac{z^2}{R_z^2}, 0 \right), \tag{2.37}$$

where R_i is the Thomas-Fermi radius in the i-th direction which is given by

$$R_i = a_{\mathrm{ho}} \left(\frac{15 N a_{BB}}{a_{\mathrm{ho}}} \right)^{1/5} \frac{\bar{\omega}}{\omega_i}, \tag{2.38}$$

and $a_{\mathrm{ho}} = \sqrt{\hbar/m\bar{\omega}}$ is the harmonic-oscillator length. Thus, the density of the BEC can be described by an inverted parabola whose size is characterized by the Thomas-Fermi radius R_i. Beyond R_i, the density of condensed bosons vanishes. Note that the density of the bosons contains no information on the temperature of the sample. However, the thermal bosons still follow a Maxwell-Boltzmann density distribution according to Equation (2.31). Thus, when working with a partially condensed bosonic sample, one can extract the temperature from the thermal distribution. It can be shown that the momentum distribution also takes the form of the inverted parabola in Equation (2.38), where one rescales the Thomas–Fermi radii according to the time of flight [71].

2.2.4 Trapped Fermi gases

We treat a trapped degenerate Fermi gas with the Fermi–Dirac distribution given by

$$f(E) = \frac{1}{e^{(E-\mu)/k_B T} + 1}. \tag{2.39}$$

At zero temperature, Equation (2.39) takes the form of a step function where the distribution probability is unity until $E = \mu$. Once the energy is larger than the Fermi energy $E_F = \mu(T \to 0)$, the occupation probability is zero. We can relate E_F to the number of fermions

N by [72]

$$N = \int_0^\infty f(E)g(E)dE = \int_0^{E_F} g(E)dE = \frac{E_F}{6(\hbar\bar{\omega})^3}, \tag{2.40}$$

such that

$$E_F = \hbar\bar{\omega}(6N)^{1/3}. \tag{2.41}$$

We obtain an analogous relation to Equation (2.34) by relating the Fermi energy to the Fermi temperature $E_F = k_B T_F$, such that

$$k_B T_F \cong 1.817\hbar\bar{\omega}N^{1/3}. \tag{2.42}$$

The Fermi temperature sets a temperature scale when a Fermi gas deviates from the classical behavior[1]. Combining Equation (2.41) and Equation (2.30), we can relate the fugacity $\zeta = e^{\mu/k_B T}$, temperature and Fermi temperature by

$$\mathrm{Li}_3(-\zeta) = -\frac{1}{6(T/T_F)^3}, \tag{2.43}$$

where $\mathrm{Li}_n(x)$ is the polylogarithmic function of n-th order.

To calculate the density and momentum distribution, we combine Equation (2.27) and Equation (2.39) to rewrite the probability distribution in terms of the momentum and position of the fermions $f(\boldsymbol{r},\boldsymbol{p})$. According, the density is given by

$$n(x,y,z) = -\left(\frac{mk_BT}{2\pi\hbar^2}\right)^{3/2}\mathrm{Li}_{3/2}\left(-\zeta e^{\frac{-m(\omega_x^2x^2+\omega_y^2y^2+\omega_z^2z^2)}{2k_BT}}\right). \tag{2.44}$$

Similarly, the momentum distribution is given by

$$n(p_x,p_y,p_z) = -\left(\frac{k_BT}{2\pi m\bar{\omega}^2}\right)^{3/2}\mathrm{Li}_{3/2}\left(-\zeta e^{-\frac{p_x^2+p_y^2+p_z^2}{2mk_BT}}\right). \tag{2.45}$$

2.2.5 Phase separation and collapse

After having discussed trapped bosons and fermions individually, we look at the behavior of degenerate Bose and Fermi gases in a harmonic trap which interact with each other. We consider that the interactions between bosons and fermions can be tuned with the interspecies scattering length a_{BF}, whereas the interactions between the bosons can be described by the boson-boson intraspecies scattering length a_{BB}. We limit our discussion to single-component fermionic gases where the Pauli exclusion principle suppresses the collisions between the fermions.

Trapped atomic Bose–Fermi mixtures were discussed for the first time by K. Mølmer in Ref. [73], where the author studied the stability of the mixture against phase separation or collapse as a function of the interspecies interaction with a mean-field approach. Here, phase separation refers to the spatial separation of the bosons and the fermions, whereas

[1] Practically, we can see the effect of Fermi pressure for $T \lesssim 0.6\,T_F$

collapse refers to the divergence of the density of one of the species. The evolution of the density profiles of Bose–Fermi mixtures are studied as a function of the interspecies scattering lengths a_{BF}, which is attractive (repulsive) when $a_{BF} < 0$ ($a_{BF} > 0$). At the same time, the boson-boson interaction is considered to be repulsive, i.e., $a_{BB} > 0$.

In the noninteracting case ($a_{BF} = 0$), the bosons and fermions decouple from one another. The densities in the mixture are given by the densities of the individual species (see Figure 2.2a) as discussed in the previous chapters. As the interspecies interactions become attractive, the density of both species increases in the center of the trap (see panel (b)). In the case of strong attractive interactions $a_{BF} \ll -a_{BB}$, the densities of the mixture diverge signifying collapse. In contrast, repulsive interactions cause the Fermi gas to deplete from the center, being pushed to the peripherals of the trap (panel (c)). Once, $a_{BF} \gg a_{BB}$, the bosons and fermions are spatially separated and a new stable equilibrium is realized by the system.

Within the mean-field approximation, a criterion for instability towards collapse or spatial separation has been established by Viverit *et al.* [75] given by

$$n_F^{1/3} > \frac{(6\pi^2)^{2/3}}{12\pi} \frac{\mu_{BF}^2 a_{BB}}{m_B m_F a_{BF}^2}, \tag{2.46}$$

where $\mu_{BF} = (m_B m_F)/(m_F + m_B)$ is the reduced mass for a boson of mass m_B colliding with a fermion of mass m_F. Here, n_F is the density of the fermions. Collapse and phase separation have also been studied in more recent theoretical works [76, 77]. While the criterion for instability differs between the methods, generally for $|a_{BF}| \gtrsim a_{BB}$ the mixtures becomes unstable.

The phenomena of collapse and phase separation have been confirmed in experiments. The behavior of a ^{40}K-^{87}Rb mixture was probed for $a_{BF} = -284\,a_0$ while $a_{BB} = 100\,a_0$ [78]. The authors observed that the attractive interaction enhances the density and results in a substantial loss of atoms. Around the same time, another investigation in a ^{40}K-^{87}Rb mixture in Florence [79] observed the collapse of the BEC. They also studied the regime of Bose–Fermi repulsion and saw the loss of atoms and survival of the condensate. The authors attribute the survival of the BEC to phase separation because interspecies inelastic collisions reduce once the BEC and Fermi gas are spatially separated. While phase separation and collapse have been investigated with quite some detail, they mask more interesting physics expected in Bose–Fermi mixtures, such as molecule formation.

2.3 Molecule formation in Bose–Fermi mixtures

Initial studies of Bose–Fermi mixtures in solid-state physics were captured by so-called Fröhlich or Holstein models [80, 81], where the interactions between the fermionic electrons are mediated by bosonic phonons. Theoretical investigations of the Fröhlich model predict a rich phase diagram featuring polaron formation [82–84], boson-induced superfluidity [85] to boson softening and phase separation [86]. These models, which are calculated by mean-field inspired approaches, neglect the pairing of bosons and fermions into compos-

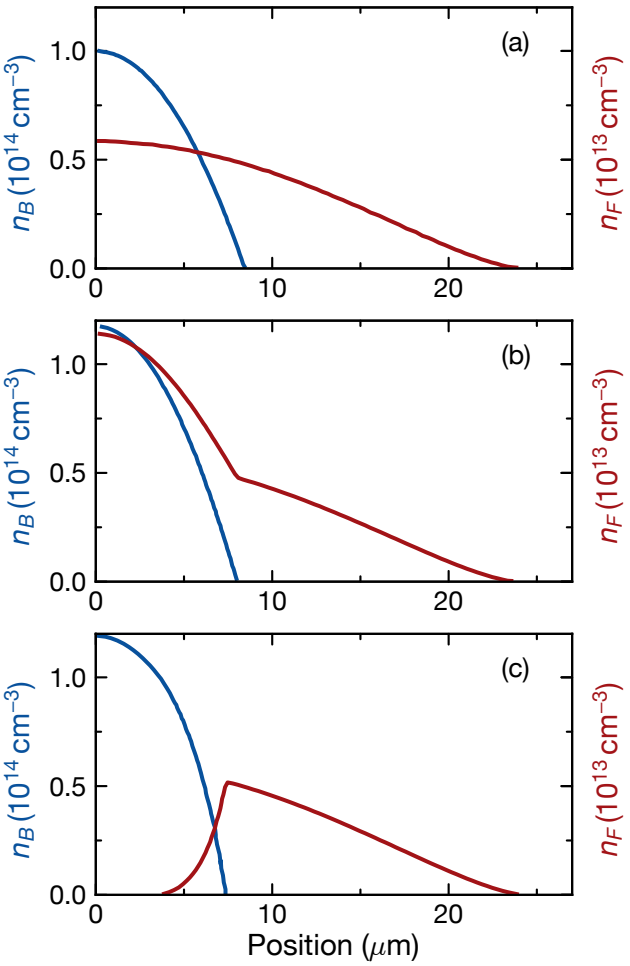

Figure 2.2 – Density profile of a Bose–Fermi mixture at different interactions. The densities of bosons (blue) and fermions (red) are shown for $T = 0$ for (a) a noninteracting mixture ($a_{BF}/a_{BB} = 0$), (b) attractive interactions ($a_{BF}/a_{BB} = -2.9$), (b) repulsive interactions ($a_{BF}/a_{BB} = 2.9$). This calculation is based on a full Gross–Pitaevskii equation for the bosons and a Thomas–Fermi approximation for the fermions. The figure is adapted from [74].

ite fermionic particles, an important feature of atomic Bose–Fermi mixtures.

The Hamiltonian for Bose–Fermi mixtures in terms of a single-channel model, where the molecules exist in the open channel[2], is described by [87]

$$H = \sum_{\mathbf{p}} \varepsilon^c_{\mathbf{p}} c^\dagger_{\mathbf{p}} c_{\mathbf{p}} + \sum_{\mathbf{p}} \varepsilon^d_{\mathbf{p}} d^\dagger_{\mathbf{p}} d_{\mathbf{p}} + \frac{U}{V} \sum_{\mathbf{p},\mathbf{p}',\mathbf{q}} c^\dagger_{\mathbf{p}+\mathbf{q}} c_{\mathbf{p}} d^\dagger_{\mathbf{p}'-\mathbf{q}} d_{\mathbf{p}'}, \tag{2.47}$$

where $c^\dagger_{\mathbf{p}}$ and $d^\dagger_{\mathbf{p}}$ are the fermionic and bosonic annihilation operators, respectively. The first two terms capture the kinetic energy of the mixture, where the free dispersion relation of the fermionic and bosonic particles are respectively given by $\varepsilon^c_{\mathbf{p}} = \mathbf{p}^2/2m_F$ and $\varepsilon^d_{\mathbf{p}} = \mathbf{p}^2/2m_B$. The last term describes the contact interaction between the bosons and the fermions, where V is the system volume and the interaction strength U is given by

$$U^{-1} = \mu_{BF}/2\pi a_{BF}\hbar^2 - V^{-1} \sum_{\mathbf{k}} 1/(\varepsilon^c_{\mathbf{k}} + \varepsilon^d_{\mathbf{k}}), \tag{2.48}$$

where μ_{BF} is the reduced mass of the boson-fermion atom pair.

The existence of the bound state complicates the phase diagram of Bose–Fermi mixtures. The theoretical challenge is to extend the Fröhlich model to include the pairing into molecules. Since the molecules are fermions, they evade mean-field approaches and are more challenging to describe than bosons [88]. Thus, before considering the system of a large sample of bosons and fermions, we simplify the discussion to a single bosonic impurity interacting with its fermionic environment.

This will be important to understand the association of molecules from degenerate Bose–Fermi mixtures. The presence of the fermionic bath dresses the single boson. As a consequence, the impurity is described by the notion of quasiparticles called polarons, and the picture of Feshbach association discussed in Section 2.1.3 is modified.

2.3.1 Impurity limit: The Fermi polaron

The idea of polarons dates back to the 1930s when Lev Landau realized that electrons moving in a dielectric crystal will displace the atoms from their equilibrium position, which leads to defects in the crystal [89]. While the concept of polarons was first studied in the context of solid-state physics, ultracold atoms provide an exciting playground to investigate the physics of polarons [90–92].

To this end, one needs to create a system of two (or more) interacting types of particles, differing in at least one quantum number. Furthermore, strong population imbalance is needed such that the interactions between the impurities can be neglected. While this is not a realistic situation in the experiment, we consider a single impurity of one species immersed in a bath of the other species for the discussion below.

[2] For narrow Feshbach resonances, one can also use a two-channel model Hamiltonian. The two-channel Hamiltonian with an infinitely broad Feshbach resonance is equivalent to the single-channel Hamiltonian in Equation (2.47).

While in the noninteracting system, the impurity can be described by its intrinsic properties, this changes as the interactions are turned on, leading to an adiabatic change compared to the noninteracting ground state. The impurity will be dressed by the excitations of the surrounding medium so that the impurity can be described as a quasiparticle with renormalized energy, mobility and mass. While discussing the case of the Fermi polaron, we note that fermions immersed into a bosonic bath can be described by the Bose polaron.

The physics of the Fermi polaron can be captured a by a variational wavefunction that approximates the eigenstate of the Hamiltonian in Equation (2.47). The so-called Chevy Ansatz [93] for the zero-momentum polaron is given by

$$|\text{Pol}\rangle = \alpha_0 d_0^\dagger |\text{FS(N)}\rangle + \sum_{\mathbf{kq}} \alpha_{\mathbf{kq}} d_{\mathbf{q}-\mathbf{k}}^\dagger c_{\mathbf{k}}^\dagger c_{\mathbf{q}} |\text{FS(N)}\rangle \tag{2.49}$$

where α_0 and $\alpha_{\mathbf{kq}}$ denote the variational parameters and $|\text{FS(N)}\rangle$ denotes a Fermi sea containing N fermions. Here, $d_{\mathbf{q}}$ and $c_{\mathbf{q}}$ are the annihilation operators for bosons and fermion with momentum $\mathbf{q}$, respectively. The first term describes the coherent part of the polaronic wavefunction. The quasiparticle weight is defined as the square-overlap with the coherent part of the quasiparticle wavefunction, i.e., $Z = |\alpha_0|^2$. For $Z = 1$, the bosonic impurity is fully decoupled from the Fermi gas. For $Z < 1$, there is a finite number of particle-hole excitations of the Fermi sea, which originate from the finite interactions between impurity and the Fermi sea. This is captured by the second term in Equation (2.49), where the summation is executed for all momenta fulfilling $|\mathbf{k}| > k_F$ and $|\mathbf{q}| < k_F$, which assures that no hole is generated within the Fermi sea and the corresponding particle lies outside. Here, $k_F = \sqrt{2m_F E_F/\hbar^2}$ is the Fermi wavevector. As illustrated in Figure 2.3, the ground state of the system is expected to be a superposition of the unperturbed Fermi sea and a bosonic impurity with a particle-hole excitation where a particle within the Fermi sea can be excited from momentum $\mathbf{q}$ to momentum $\mathbf{k}$, while the impurity carries the energy of $\mathbf{q}-\mathbf{k}$.

In a similar fashion, the molecular state can be described by an Ansatz with a variational parameter $\beta_{\mathbf{k}}$

$$|\text{Mol}\rangle = \sum_{\mathbf{k}} \beta_{\mathbf{k}} c_{-\mathbf{k}}^\dagger d_{\mathbf{k}}^\dagger |\text{FS(N-1)}\rangle\,, \tag{2.50}$$

where a fermion is paired with the bosonic impurity to form a molecule. The summation is executed for all momenta fulfilling $|\mathbf{k}| > k_F$ and $|\mathbf{q}| < k_F$, which assures that a hole is generated within the Fermi sea and the corresponding particle lies outside.

The minimization of the energy functionals $\lambda_{\text{Pol}}(E) = \langle \text{Pol}|H - E|\text{Pol}\rangle$ and $\lambda_{\text{Mol}}(E) = \langle \text{Mol}|H - E|\text{Mol}\rangle$ with respect to the variational parameters allows to determine the renormalized dispersion relations for the polaron and the molecule, respectively. While minimizing the functional for the molecules provides one solution, for the polaron one finds two solutions. The lower-lying state is referred to as the *attractive polaron* while the higher lying state is the *repulsive polaron* [94].

In Figure 2.4, one can see the spectrum of the Fermi-polaron problem with three branches corresponding to the attractive (red) and repulsive (blue) polaron as well as the molecule (gray). The ground state of the system is either given by the attractive polaron or by the

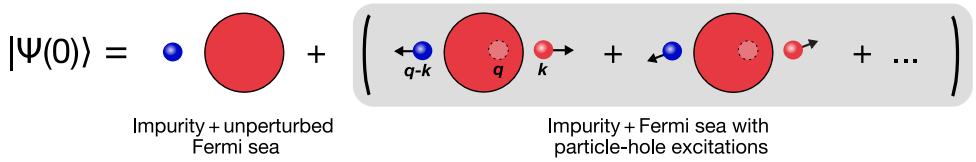

Figure 2.3 – Illustration of the polaron wavefunction according to the Chevy Ansatz. The first term shows the unperturbed Fermi sea (red) and a bosonic impurity (blue). The term contained in the gray shaded area illustrates the sum over the various particle-hole excitations for an impurity with zero momentum ($p = 0$). The excited particles are shown in red, while the hole is shown in light red.

molecular state, depending on the interaction strength. In the regime of attractive interparticle interaction, the bosonic impurity deforms the Fermi sea by attracting the fermionic atoms, leading to a lower energy of the now dressed boson with respect to the energy of the bare energy of the bosonic impurity. At some interaction, the attractive polaron is an excited state of the system and the molecule is the ground state. Unlike the two-body picture discussed in Section 2.1.3, where the molecular state is the ground state at unitarity $1/(k_F a_{BF}) = 0$, the polaron-to-molecule transition occurs for $1/(k_F a_{BF}) > 0$. The repulsive polaron is always an excited state of the system, where the bosonic impurity repels the fermions leading to higher energy compared to the non-dressed case. In the weak-coupling limit $1/(k_F a_{BF}) \to \infty$, the repulsive polaron is a well-defined quasiparticle. However, when the energy of the repulsive polaron becomes larger than the Fermi energy of the bath, the repulsive polaron decays into the lower-lying molecular state [94].

At last, we note that already with the simple variational Ansatz considering one particle-hole excitation captured by Equations (2.49)-(2.50), one can qualitatively reproduce the spectrum shown in Figure 2.4. By considering more particle-hole excitations, one can improve the predictions of the spectrum, which can, for example, shift the predicted polaron-to-molecule transition point.

The Fermi-polaron problem has already been explored in experiments. In two-component Fermi gases[3], the Fermi polaron has been studied with two different hyperfine states of the same fermionic atom with a large number imbalance. Properties of attractive and repulsive Fermi polarons were examined, including their effective mass [95, 96], energy [96–99], thermodynamics [100], equation of state [101], and formation dynamics [102]. Recently, the quasiparticle weight of the Fermi polaron has been mapped out, where a phase transition from attractive polarons to molecules has been established [103].

2.3.2 Beyond the Fermi-polaron limit

After this excursion into the limit of a single boson in a Fermi sea, we return to the problem of Bose–Fermi mixtures where both species have a finite density. In light of our goal to associate atoms in degenerate Bose–Fermi mixtures into molecules, we want to understand

[3] Note that in the limit of a single impurity, it does not matter whether the particle is a boson or a fermion.

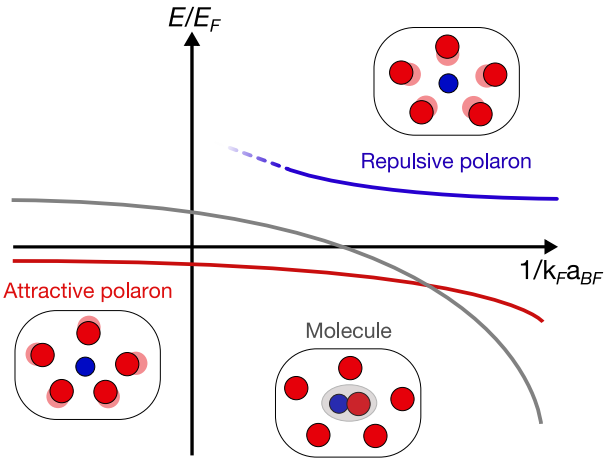

Figure 2.4 – Spectrum of the Fermi-polaron problem as a function of the dimensionless interaction strength $1/k_F a_{BF}$. Energy of the attractive (red line), repulsive (blue line) polaron and molecule (gray line). The insets illustrate the behavior of the polaron and molecule states in a Bose–Fermi mixture with one bosonic impurity (blue) in a large sample of fermions (red).

whether the polaron-to-molecule transition persists for a finite density of bosons. Studies of the energy spectrum of the repulsive Fermi polaron in Ref. [104] show that the energy of the repulsive polaron only exhibits a negligible shift when the concentration of the bosons compared to the fermions is changed from about 20% to 60%. This suggests that the picture of the Fermi polaron holds even for a substantial impurity density.

Experimentally, the polaron-to-molecule transition in the equal-density regime when both species are degenerate has been unexplored until our work in Ref. [105]. In contrast, various theoretical works have studied the equal-density Bose–Fermi mixtures. When $n_B \leq n_F$, where n_B is the density of the bosons and n_F is the density of the fermions, the studies identify two phases. One is a phase where the bosons are condensed and a regime where all the bosons are bound into molecules, and the condensate is fully depleted. According to all the theoretical investigation in Refs. [106–110] studying the phase diagram of Bose–Fermi mixtures, the following scenarios are possible when going from the condensed phase into the molecular phase:

- There is a *second-order quantum phase transition* where the depletion of the bosonic condensate fraction is continuous until it vanishes at the critical interaction strength.
- There is a *first-order quantum phase transition* with a phase-separation region between the phase featuring a condensate and the phase featuring molecules. Here, phase separation refers to a region of interaction strengths where locally the condensate fraction discontinuously becomes zero while other regions might still have a condensate.
- A *collapse* occurs and there is no stable region connecting the phase featuring the condensate and the molecular phase.

In the works of Ludwig *et al.* in Ref. [108], the authors consider a two-channel model of Bose–Fermi mixtures in the limit of an infinitely broad Feshbach resonance. In contrast to our experiment, the authors investigate the transition behavior by starting in the molecular phase and entering the condensate phase. Instead of tuning the scattering length, they change the chemical potential in their calculations, thus fixing the ratio of a_{BF}/a_{BB}. They find that the system is only stable for sufficiently large Bose–Bose repulsion a_{BB}. Moreover, they find that a large a_{BB} favor a second-order phase transition while low a_{BB} favor a first-order phase transition.

In the works of Bertaina *et al.* in Ref. [109], the authors use Monte Carlo methods to map out the phase diagram. They consider a boson-boson repulsion, which is about two orders of magnitude larger than in our experiment, to ensure that collapse is not an issue. According to their calculations, there is a first-order quantum phase transition with a phase separation region. The phase-separation region shrink as the density ratio of the boson to fermion density n_B/n_F is reduced.

The same group has also published another calculation in Ref. [110] where they characterize the condensed phase, irrespective of whether it represents the ground state. The authors use Monte Carlo methods and diagrammatic approaches to map out the phase diagram. Here, a considerably weaker boson-boson repulsion is used, which is comparable to typical mixture experiments. Interestingly, the authors do not address the question of the order of the phase transition. However, this work is very useful for us because we can compare our data of the condensate fraction as a function of the interaction strength to the calculations.

This short overview of the literature on the phase transition in Bose–Fermi mixtures finalizes our discussion on the problem of trapped Bose–Fermi mixtures with interactions. We have seen that in the impurity limit, quasiparticle formation occurs and that for sufficiently strong interactions, the quasiparticle transitions into a molecule. Theoretical studies suggest that a polaron-to-molecule transition extends beyond the impurity limit and that the process can be understood as a phase transition of unknown order. In the following, we discuss the experimental setup that allows us to produce a double-degenerate Bose–Fermi mixture as a starting point for the production of molecules.

Great acts are made up of small deeds.

—Lao Tzu

3 Experimental setup

The NaK-machine is a dual-species experimental apparatus whose construction has started more than a decade ago. With each generation of Ph.D. students, the experiment has been adapted to overcome the challenges of that generation. The challenge during this Ph.D. work was to adapt the experimental machine to produce degenerate molecules. In this chapter, I will first give an overview of the experimental apparatus and sequence. This will give the reader a foundation to understand the measurements presented in the upcoming chapters. In addition, I will then describe the upgrades to the experimental machine to produce and density-match a double-degenerate Bose–Fermi mixture before focusing on the methods to characterize our samples.

3.1 Overview of the vacuum system

The heart of the experiment is the vacuum system shown in Figure 3.1, which was built up by the first generation of members of this experiment, and has been almost unchanged since its first assembly. The design considerations are discussed in detail in the Ph.D. theses of Nikolaus Buchheim, Zhenkai Lu and Frauke Seeßelberg [111–113].

The vacuum setup consists of two oven sections, one for the Na atoms and one for the K atoms. The Na oven is designed to minimize maintainance of the Na source. This is done by allowing for the reflow of Na atoms into the oven when the experiment is not running. Accordingly, we did not need to exchange the Na source since 2013 [111]. In comparison, the team at the NaK-machine in Hannover working with bosonic NaK molecules exchanges their Na source every year. The K oven contains a sample where the fermionic isotope ^{40}K has been enriched to 3%. Both oven sections have ion pumps. The setup has a 2D-MOT section and a Zeeman slower section to precool the K and the Na atoms, respectively, which connect with a differential tube to the main chamber. The cooling stages to the microkelvin regime for both species are performed in the main chamber. The experiments are conducted in the glass cell (also called "science cell") attached to the main chamber. Inside the glass cell are four electric field rods that can create electric fields and electric-field gradients. The electric field can be used to polarize the molecules. Each oven can be separated from the rest of the machine by closing vacuum valves. To keep the pressure in the experimental chambers at $\sim 10^{-11}$ mbar, this section has an additional ion and titanium-sublimation pump, however, we have not made use of the sublimation since at least 2018.

Typical of any cold-atom or cold-molecule experiment are magnetic field coils, which for illustration purposes, are not shown in Figure 3.1. We can apply magnetic fields and magnetic-field gradient with magnetic field coils around the main chamber and the glass cell. In the main chamber, the direction of the currents in the so-called main coils is chosen

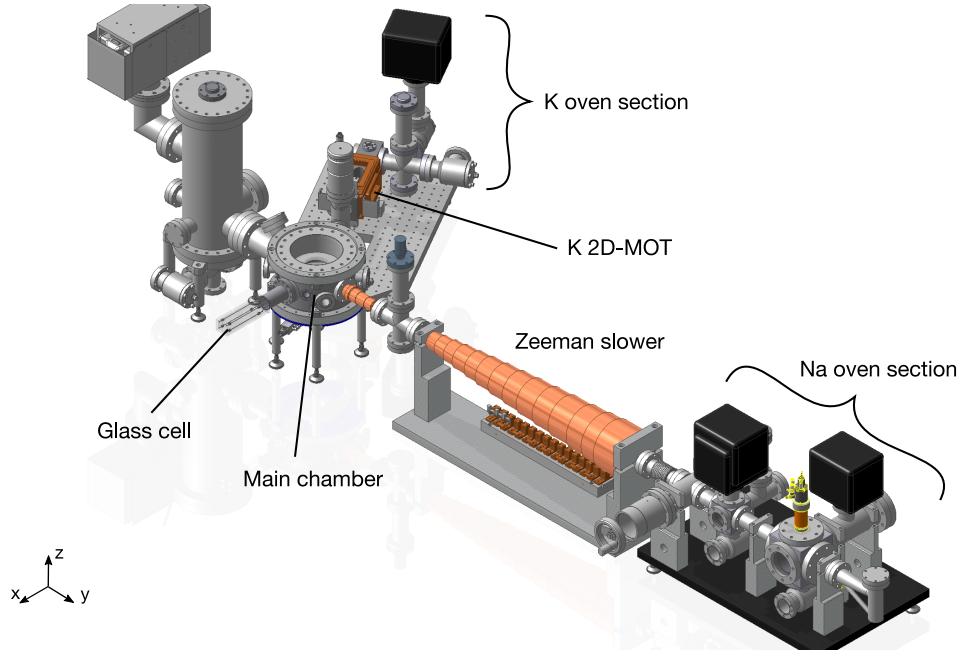

Figure 3.1 – The vacuum system of the NaK polar molecules machine. The oven sections for Na and K are connected to the main chamber via a Zeeman slower for ^{23}Na and a 2D-MOT chamber for ^{40}K. In the main chamber, the two species are loaded into a 3D-MOT. After the evaporation in the magnetic trap, the atoms are transported into the glass cell, where the experiments are performed. The coordinate system shown at the bottom of the figure will be used throughout this thesis where x points in the transport direction, y in the Zeeman-slower direction, and z in the vertical direction.

to produce magnetic-gradient fields, while the bias coils generate small offset magnetic fields in all spatial direction. This is important to control the position of zero magnetic field for the MOT or the magnetic trap which might be shifted by Earth's magnetic field or stray fields from various devices in the lab. Around the glass cell, there are two pairs of coils. The so-called Feshbach coils produce homogeneous magnetic fields, for example, for the Feshbach association. The auxiliary coils are used to produce magnetic-field gradients for levitation or remove atoms from the trap by applying a strong gradient pulse.

3.2 Experimental sequence

The best way to get to know the experiment is to experience it as the atoms do. To this end, I will describe the experimental sequence reporting the typical numbers and temperatures in the different stages to create ground-state molecules in the quantum-degenerate regime.

After the ^{23}Na and ^{40}K atoms leave their respective oven section, they are precooled before entering the main chamber. The ^{23}Na atoms are precooled in the axial direction as they traverse the Zeeman slower, while the ^{40}K atoms are transversely cooled in a two-

dimensional MOT (2D-MOT) stage. In the main chamber, the atoms are then loaded into a three-dimensional MOT. In order to avoid interspecies losses during the loading and cooling stages in the MOT, we intentionally displace the two clouds from one another by slightly misaligning the MOT beams. This is necessary to achieve a compromise between the number of Na and K atoms.

After loading the MOT for about 6 s, the magnetic field gradient is decreased from 13 G/cm to 7 G/cm and cooling is performed in the compressed-MOT configuration (CMOT). Typically, the compression in the MOT stage refers to a spatial compression and is used to mode-match the atomic cloud with the following sequence. In our experiment, we found out that the most efficient loading of the magnetic trap is achieved when reducing the magnetic field gradient and thus compressing the sample in momentum space. Following the CMOT stage, the gradient is turned off to perform sub-Doppler gray-molasses cooling[1] on the D_1-line for ^{23}Na [114]. During the gray molasses, the ^{40}K atoms are cooled in optical molasses [115]. After laser-cooling, we optically pump the atoms into the their respective low-field seeking states $|F,m_F\rangle = |2,2\rangle$ and $|F,m_F\rangle = |9/2,9/2\rangle$ in ^{23}Na and ^{40}K.

Both species are then transferred into an optically-plugged magnetic quadrupole trap by quickly ramping the magnetic-field gradient to 60 G/cm. Since the optical pumping is not perfect and the magnetic gradient is sufficiently large, some low-field seeking hyperfine states of each species can be trapped inside the magnetic trap. All states except for the hyperfine-stretched states need to be removed to prevent loss and heating due to spin-exchanging collisions during the evaporation. To this end, the magnetic-field gradient is ramped from 60 G/cm to the spin-purification gradient of about 8 G/cm, such that only the states $|2,2\rangle$ and $|9/2,9/2\rangle$ in ^{23}Na and ^{40}K, respectively, remain trapped. The spin-purification gradient is maintained for 2 s during which the unwanted spin states are pulled out of the trap due to gravity. Since the two states do not share the same magnetic moment, we commonly select the ratio between ^{23}Na and ^{40}K atoms by changing the spin-purification gradient. Note that an alternative way to change the ratio of the species comes from tuning the duration of the MOT loading for K atoms.

After the spin purification, the magnetic-field gradient is adiabatically increased to 250 G/cm which increases the density of the sample and leads to an efficient evaporation. As a result of the adiabatic compression, the temperature of the mixture at the start of the evaporation is increased to 1 mK. Subsequently, radio-frequency forced evaporation takes place, where we ramp down the magnetic-field gradient and transfer the hottest ^{23}Na atoms by a radio-frequency field to an untrappable hyperfine state. Since the spin-polarized ^{40}K atoms cannot undergo evaporative cooling, they get sympathetically cooled by the ^{23}Na cloud. After the evaporation, there are about 1.6×10^8 ^{23}Na atoms and 1.0×10^6 ^{40}K atoms at a temperature of 6 μK.

We load this mixture into an optical dipole trap while the residual magnetic field gradient is ramped down. In the so-called transport trap, the Na atoms undergo the hyperfine-state

[1] The gray molasses cooling has been implemented into the experiment to compensate for a continuous reduction of the number of Na atoms in the magnetic trap from 2018 until 2021 and was crucial for the first production of degenerate Feshbach molecules. An unexplained event in the summer of 2021 led to a sudden increase in the number of Na atoms such that the gray molasses was not needed.

transfer $|2,2\rangle \rightarrow |1,1\rangle$ in order to mitigate spin-exchanging collisions inside the trap. This transport trap is formed by two 1064-nm laser beams that intersect at an angle of about 2.6°. In comparison to a single transport beam, the axial confinement is larger, which helps during the transport as described in Section 3.3.2. Overall, 2×10^7 Na atoms and 6×10^5 K atoms are loaded into the transport trap.

After the transport from the main chamber to the glass cell, the mixture is transferred into a crossed optical dipole trap formed by one of the transport beams and an additional 1550-nm beam. At the start of the optical evaporation, we have 6×10^6 Na atoms and 2×10^5 K atoms at a temperature of about 1 µK. Optical evaporation is performed by exponentially ramping down the beam powers of the 1064-nm and 1550-nm beam. The magnetic field during the evaporation is 90 G.

For the experiments in which we associate the double-degenerate mixture into molecules, an additional 785-nm optical dipole trap is ramped on during the evaporation, which confines the ^{40}K atoms more strongly than the ^{23}Na atoms (see Section 3.4). After decompressing the 1550/1064-nm crossed-optical dipole trap, the confinement is dominated by the 785-nm optical dipole trap. As a result, a degenerate Fermi gas of 2.3×10^5 ^{40}K atoms is density-matched with more than 5×10^4 condensed ^{23}Na atoms.

The density-matched degenerate Bose–Fermi mixture is the starting point for the association of degenerate NaK* Feshbach molecules as discussed in Chapter 5. In short, after the optical evaporation, we change the hyperfine state of the K atoms with a series of radio-frequency sweeps from $|9/2,9/2\rangle \rightarrow |9/2,-9/2\rangle$ before ramping the magnetic field through an interspecies Feshbach resonance at 78.3 G which transfers the unbound atoms into Feshbach molecules. We typically produce 5×10^4 Feshbach molecules at a temperature of about 100 nK. We then transfer the Feshbach molecules into the rovibronic ground state by Stimulated Rapid Adiabatic Passage (STIRAP).

3.3 Optical traps

In this section, I will discuss the optical traps used in the setup. Both, the upgrade of the optical trap that transports the atoms and the species-dependent trapping potential for the Feshbach association were crucial steps towards improving the Feshbach association and obtain degenerate samples.

3.3.1 Atoms and molecules in an optical trap

In the presence of a light field, a particle (atom or molecule) experiences a force due to the interaction of the particle's dipole moment with the light field. This force comes from a gradient in the interaction potential $U(x,y,z)$, which is given by

$$U(x,y,z) = \alpha I(x,y,z), \tag{3.1}$$

where α is the real part of the dipole polarizability [9] and $I(x,y,z)$ is the light intensity. For now, we ignore the imaginary part of the polarizability, which corresponds to particle

absorbing photons and leads to heating of the particles. If the trap is far-detuned from any transitions, the real part of the polarizability dominates over the imaginary one.

3.3.1.1 Circular Gaussian beam

Before discussing how we calculate the trap parameters in the experiment for real dipole traps, we consider a simple example: a focused circular Gaussian beam propagating in the z-direction with waist w_0. Here, circular refers to the fact that the waist of the Gaussian beam is the same in all directions perpendicular to the propagation direction. Accordingly, we can write the intensity of the Gaussian beam I in cylindrical coordinates as

$$I(r,z) = I_0 \left(\frac{1}{1+(z/z_R)^2} \right) \exp\left(\frac{-2r^2}{w_0^2 (1+(z/z_R)^2)} \right), \tag{3.2}$$

where I_0 is the peak intensity. The Rayleigh length z_R is given by $z_R = (\pi w_0^2)/\lambda$ where λ is the beam's wavelength. We also consider that the trapping light is red-detuned to the transition that we use for trapping, i.e., the frequency of the laser beam $\nu = c/\lambda$ is smaller than the transition frequency. Then $\alpha < 0$, and the Equation (3.1) describes a potential with a minimum $U_0 = U(r = 0, z = 0)$ where U_0 is the trap depth. Typically, the atoms reside in the minimum of the trap, meaning the temperature of the particles is considerably smaller than the trap depth, and we approximate the potential around the minimum as a harmonic potential of the following form:

$$U_{\text{harm}}(r,z) \approx -U_0 + U_0 \left(\frac{2r^2}{w_0^2} + \frac{z^2}{z_R^2} \right). \tag{3.3}$$

For a particle of mass m, the equation of motion in this harmonic potential in the direction $r_i = \{r, z\}$ is

$$m\ddot{r}_i = -\frac{\mathrm{d}U_{\text{harm}}}{\mathrm{d}r_i}. \tag{3.4}$$

and the trapping frequencies are

$$\omega_r = \sqrt{\frac{4U_0}{m w_r^2}}, \tag{3.5}$$

$$\omega_z = \sqrt{\frac{2U_0}{m z_R^2}} \tag{3.6}$$

in the radial direction r and the axial direction z, respectively.

3.3.1.2 Simulation for the experiment

For the actual dipole traps we use in the experiment, we use a computer simulation to compute the trapping frequency of a specific species in the dipole trap we are interested in. In

contrast to our easy example in Section 3.3.1.1, our dipole traps are made of up to four different laser beams of different wavelengths that are propagating in different directions and have an elliptical beam shape. The beam waists in the simulation typically are taken from measured beam waists or calculated by Gaussian beam propagation based on the optical setup. We then calculate the trapping potential as the sum of contributions from each individual beam such that

$$U(x,y,z) = \sum_{\text{beam}} \alpha_{\text{beam}} I_{\text{beam}}(x,y,z). \tag{3.7}$$

We assume that all the trapping beams are focused in the same spot. For each species we calculate the trapping potential and obtain the trapping frequencies from the second derivative of the potential around its minimum, i.e.,

$$\omega_{r_i} = \sqrt{\mathrm{d}^2 U(x,y,z)/\mathrm{d}r_i^2/m}. \tag{3.8}$$

Here, m is the mass of the particle we are interested in and $r_i = x,y,z$ are three spatial directions as shown in Figure 3.1. The assumption that all foci coincide is not necessarily given in the experiment. Nevertheless, we align and calibrate the traps for each critical measurement, and the trapping frequencies typically agree with the simulation.

We calculate the polarizabilities of alkali atoms in a light field with frequency ω with the formula

$$\alpha = -\frac{3\pi c^2}{2\omega_0^3}\left(\frac{\Gamma}{\omega_0-\omega}+\frac{\Gamma}{\omega_0+\omega}\right), \tag{3.9}$$

where ω_0 is the nearest atomic transition frequency and Γ the natural linewidth of that transition [9]. In our experiment, the frequencies of the trapping beams are near-infrared and the closest transitions contributing to the polarizability for both the Na and K atoms come from the D-lines. The transition frequencies and their respective natural linewidths can be found for Na atoms in Ref. [116] and for K atoms in Ref. [117]. All other transitions are much further detuned to the D-lines such that their contribution to the trapping potential is negligible.

To calculate the trapping parameters of the Feshbach molecules, we make the atom-pair approximation that the polarizability of the Feshbach molecules equals the sum of its atomic constituents, i.e., $\alpha_{\text{NaK}^*}(\omega) = \alpha_{\text{Na}}(\omega) + \alpha_{\text{K}}(\omega)$. A comparison between the polarizabilities, based on the atom-pair approximation and based on a calculation for a Feshbach molecule in the last vibrational level $v = 75$ of the $X^1\Sigma^+$-potential, shows that the discrepancy between the polarizabilities is less than 3% for a broad range of frequencies [118]. In this case, the trap depth is given by

$$U_{\text{NaK}^*} = U_{\text{Na}} + U_{\text{K}}, \tag{3.10}$$

and the trapping frequency $\omega_{r_i,\text{NaK}^*}$ for the Feshbach molecules is given by

$$\omega^2_{r_i,\text{NaK}^*} = \frac{m_{\text{K}}\omega^2_{r_i,\text{K}} + m_{\text{Na}}\omega^2_{r_i,\text{Na}}}{m_{\text{K}} + m_{\text{Na}}}. \tag{3.11}$$

Note that Equations (3.10)-(3.11) are only valid for the case where photoassociation lines

have no significant contribution to the polarizability. The polarizability of the ground-state molecules needs to be calculated independently which we deduce from Ref. [118] for the wavelengths 1064 nm and 1550 nm. The ground-state polarizabilities around 785 nm were provided to us by Nadia Bouloufa-Maafa [119].

3.3.2 Optical transport

The NaK-machine, like many experiments that need optical or mechanical access, is built with several experimental chambers which are separated by several tens of centimeters. One of the limitations in the achievable phase space density of these experiments is the optical transport, and consequently, considerable experimental effort within the ultracold-atom community has been made to optimize the atomic transport. Methods of transport include the translation of magnetic fields [120, 121], shifting tightly-focused laser beams [122–125] and transport via a moving lattice [126–128].

Until the beginning of 2019, one tightly focused 1064-nm beam transported the atomic mixture of ^{23}Na and ^{40}K from the main chamber into the glass cell. The limitation of this transport method boils down to a compromise between increasing the trap depth (thus the confinement) for efficient loading and transport at the cost of increased interspecies loss. This interspecies loss happens predominantly during the loading of the transport trap when ^{23}Na cloud is still in the hyperfine state $|F, m_F\rangle = |2, 2\rangle$ before it gets transferred into $|1, 1\rangle$.

My first project during this Ph.D. work was to improve the atom transport by decreasing the overall confinement of the trap while increasing the confinement in the direction of the transport. By using two optical beams intersecting at a small angle, we project the typically strong radial confinement of the individual trapping beams onto the direction of the transport [129]. To reduce the confinement and keep the same trap depth, we needed more optical power compared to the previous setup.

3.3.2.1 ALS-laser powered transport trap

The previous transport trap was composed of a single transport beam with a waist of 40 µm. The optical power of 7.5 W was derived from a Innolight Mephisto MOPA 18W. In 2018, during an upgrade to implement a two-dimensional horizontal lattice, we bought a fiber laser from Azurlight Systems (ALS IR-1064-50), providing 50 W at a wavelength of 1064 nm. Scott Eustice, the Master's student who built the two-dimensional horizontal lattice, designed the optics such that the lattice and the transport can be powered by the same laser [130]. During the upgrade of the optical transport, we then inserted a waveplate inside a rotation mount with a stepper motor to split the power between the transport and the horizontal-lattice beams. This is possible as the horizontal lattice beams are not needed during the transport stages or the optical evaporation, and only small powers are required in the transport trap when the atoms or molecules are loaded into the optical lattice.

One of the first problems that we encountered during the testing phases of the upgrade was that we could not provide sufficient power to the transport beam. Due to the increased beam size from 40 µm × 40 µm to about 50 µm × 100 µm, we required at least 21 W of optical

power in the transport beams to maintain the trap depth compared to the previous transport setup. When using the photonic crystal fiber AeroGUIDE POWER-15-PM from NKT Photonics with a fiber length of 5 m and a mode field diameter of 12.6 µm, the transmission efficiency reduced significantly once the transmission power exceeded 15 W. This reduction did not result from thermal lensing, as alignment did not improve the transmitted power. We could quickly attribute the effect to Stimulated Brillouin Scattering (SBS), a nonlinear effect that leads to the back-reflection of the injected power favored by a small mode field diameter and long fibers [131]. An indicator that SBS was limiting our transmission efficiency was an instant increase of the back-reflected power from the fiber once the transmission efficiency dropped. We measured this by inserting a glass plate before the fiber and detecting the power-dependent back reflection. By switching to a shorter fiber, for instance, we currently use Alphanov LMA-PM-15 with a length of 2.5 m, we get 21 W of optical power onto the optics board to generate the crossed optical transport trap.

3.3.2.2 Optical setup

The optics to produce the crossed optical transport trap are depicted in Figure 3.2. After beam-shaping, the beam is split using a waveplate mounted inside a rotation mount with a stepper motor and a polarizing beamsplitter (PBS) (Thorlabs PBS12-1064-HP). While loading the atoms into the transport beam and also during the transport, the position of the rotation waveplate is set such that the trap is in a crossed configuration. This maximizes the axial confinement of the trap for efficient transport. Once the transport of the mixture is completed, the stepper motor moves by 22.5° within 1 s to create a single beam before optically evaporating the mixture.

The reason for rotating the waveplate before the evaporation is that the imperfect polarization splitting of the PBS with an extinction ratio of 3370:1 causes a weak lattice along the vertical direction. We noticed this problem only in November 2019, about half a year after implementing the optical transport. When evaporating the atomic mixture into the deeply degenerate regime, we observed that the cloud started to split in the presence of the crossed optical transport beam, and the splitting distance of about 25 µm agrees with the expected lattice spacing for two beams with a wavelength of $\lambda = 1064\,\mathrm{nm}$ and an intersection angle of $\theta = 2.6°$.

After the splitting cube, the transport beams propagate in parallel with a displacement of 19 mm and are focused by a lens (Newport SPX055AR.10) such that they intersect at their common waist position. To make the trap movable for transport, we image the trap in a 4f configuration into the vacuum system. This 4f imaging system is made of two lenses (Newport SPX058AR.10) with focal length of 500 mm each, such that the image is created at a distance of 2 m. By changing the distance between the object and the first lens of the 4f imaging system with an air-bearing translation stage (Aerotech MTC150P), we also change the distance between the second lens and the image. Preliminary tests showed that when placing the two imaging lenses at a distance of twice the focal length, the beam waists changed by about one percent for a transport distance of about 30 cm. So in the experiment, where we transport the atoms over a distance of about 27 cm, no significant change in the beam waists occurs.

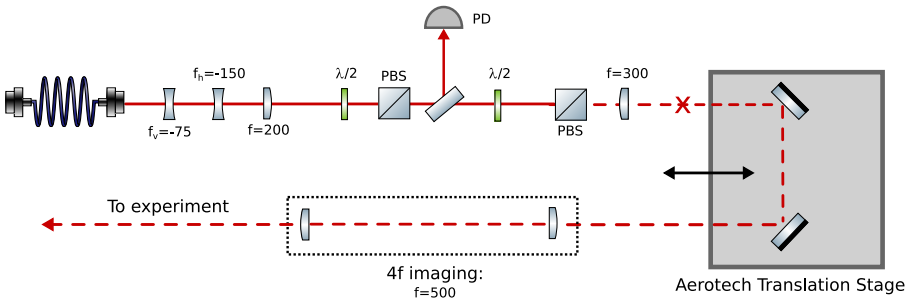

Figure 3.2 – Optics for creating and beam-shaping the transport trap. A collimated beam is magnified by a telescope, followed by polarization cleaning. The beam then transmits through a beam sampler, where a small fraction of the power is directed towards a photodiode for intensity stabilization. After the beam sampler, we use a waveplate in a motorized rotation mount and a polarizing beam splitter (PBS) to split the power into two independent optical paths. These two beams propagate in parallel onto a lens that focuses the beams, and a crossed transport trap forms (indicated by the red cross). In their focus, the beams have an elliptical beam shape with waists of about 50 µm and 100 µm in the vertical and the horizontal direction, respectively. This trap is imaged into the vacuum chamber using a 4f imaging system. We achieve transport by moving an Aerotech translation stage.

3.3.3 Intensity stabilization at low powers

During the optical evaporation in the glass cell, the transport power is reduced by almost four orders of magnitude. In particular, the transport trap is decompressed before the Feshbach association with double-degenerate Bose–Fermi to reduce the critical loss (see Section 5.4.2). This necessitates a photodiode with almost four orders of magnitude dynamic range. Using one photodiode is typically not good enough: With a maximum voltage of about 10 V, we would need to detect signals of about 1 mV which would be buried in the noise floor of the photodiode. Therefore, some experiments in our group use photodiodes with different gains, which can be switched during the sequence and allow intensity stabilization over a large range of powers. We have instead decided to use a photodiode (Hamamatsu G8370-01) soldered to a precision high-speed logarithmic amplifier (Texas Instruments LOG114). The logarithmic amplification of the photocurrent allows us to change the powers of the transport trap over more than three orders of magnitude from 21 W, during the transport, down to about 5 mW, allowing us to associate the atoms into Feshbach molecules in the presence of a shallow crossed optical dipole trap.

3.3.4 Performance of the new transport trap

To benchmark the performance of the transport trap, we image the Na and K atoms in two different stages of the sequence. One is after loading the transport trap from the magnetic trap, and the other after the transport into the glasscell has been completed. Prior to the transport upgrade, we only used to look at the loading of the transport trap and did not detect the atoms after the transport.

Table 3.1 – Details of the transport beam. The trap parameters for the crossed transport trap and the previously used single-beam transport trap. The crossed optical dipole trap has an elliptical beam shape. The smaller beam waist (higher trapping frequency) refers to the vertical direction (z-direction in Figure 3.3), and the larger beam waist (lower trapping frequency) to the direction of the Zeeman slower (y-direction). We have labeled the waists with w_v and w_h to represent the waists in the vertical and the horizontal direction, respectively.

Transport trap	Crossed	Single-beam
Laser power (W)	21	7.5
Beam waists (μm)	$(w_v, w_h) = (48, 100)$	$(w_v, w_h) = (40, 40)$
Trap depth	U/k_B (μK)	
$U_{0,\mathrm{Na}}$	370	200
$U_{0,\mathrm{K}}$	145	78
Trap frequencies	$(\omega_x, \omega_y, \omega_z)$ (Hz)	
$\omega_{i,\mathrm{Na}}$	$2\pi \times (34, 730, 1520)$	$2\pi \times (8, 1340, 1340)$
$\omega_{i,\mathrm{K}}$	$2\pi \times (42, 884, 1840)$	$2\pi \times (10, 1626, 1626)$

In the new transport trap, we managed to increase the number of loaded Na atoms by about 50% under the condition that the number of K atoms remains the same. With the single-beam transport trap we usually loaded 1×10^7 Na atoms, while with the new transport trap this was improved to 1.5×10^7 Na. Note that the numbers reported here refer to a condition where we had about 1.2×10^8 Na atoms after the evaporation in the magnetic trap. We attribute the improvement in the transport loading mainly to the increased trap depth of the new transport at full power by a factor two compared to the single-beam transport trap (see Table 3.1). However, since also the overall confinement has increased leading to stronger interspecies loss in the loading stages, we do not expect that the number of atoms loaded into the trap increases linearly with the trap depth. The performance of the transport loading could be further improved by reducing the loading time into the transport trap. When doing this, one should be careful that a faster loading of the transport trap does not lead to an increased shot-to-shot fluctuations in the atom numbers and thus unstable experimental conditions.

Unfortunately, we did not produce a comparison of the transport efficiencies of the single-beam and the crossed-beam transport trap. Instead we performed a measurement of the round-trip efficiency which constitutes a transport to the glass cell and back. With the crossed transport trap we measure a round-trip efficiency of 50% for the Na atoms while Niko Buchheim reports a one-way efficiency of 65% in his Ph.D. thesis [111].

To conclude, with the new transport trap we have managed to improve the loading into the transport beam while the transport efficiency has only improved marginally. Still, the improved conditions of the mixture in the glass cell was the crucial step towards producing double-degenerate Bose–Fermi mixtures.

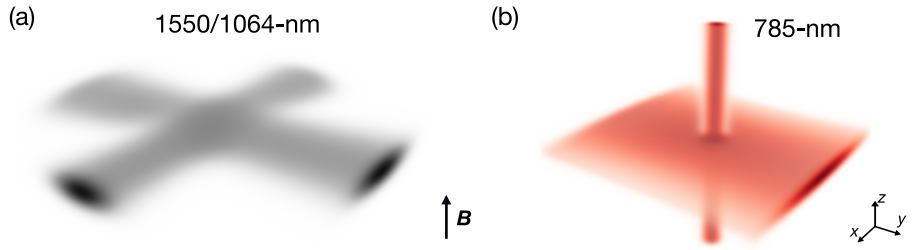

Figure 3.3 – Overview of the optical traps used in this thesis. (a) 1550/1064-nm trap: Crossed dipole trap composed of one 1064-nm beam propagating along the x-direction with a tilt of $\theta = 1.3°$ in the x/z-plane, and a 1550-nm beam along the y-direction with a tilt of $\theta = 18.5°$ in the x/y-plane. (b) 785-nm trap: The species-dependent compression trap for K atoms formed by a vertical beam propagating along the z-direction and a light sheet propagating along the y-direction.

3.4 Crossed dipole traps

In this section, I will discuss the crossed optical dipole traps used in our experiments. After initial attempts to try the Feshbach association in a three-dimensional optical lattice similar to the works in Ref. [60, 132], by creating a Mott insulator of Na atoms and a band insulator of K atoms, we decided to do the molecule production in optical dipole traps. Our improved transport trap and successful creation of a degenerate molecular KRb sample by the JILA team [43], gave us the incentive that we would also be able to create degenerate molecules in bulk.

3.4.1 1550/1064-nm trap

The 1550/1064-nm crossed optical dipole trap is the traditional trap used in our experiment, composed of one of the 1064-nm transport beams and a 1550-nm crossing beam along the y-direction. We have used this dipole trap to investigate the loss behavior of atoms and molecules in the vicinity of the 78.3-G Feshbach resonance discussed in Chapter 4 and for the association of thermal Bose–Fermi mixtures (see Section 5.2).

After the atomic mixture is transported into the glass cell, the 1550-nm light is ramped on to provide stronger confinement for the atoms along the transport direction. The transport trap is decompressed to create a trap where the confinement in both horizontal directions becomes comparable. Afterward, the waveplate rotator directs the power into a single 1064-nm beam. As part of the transport upgrade in Section 3.3.2, the beam parameters of the 1550-nm beam have been changed from a circular beam shape with a waist of $w_0 = 100\,\mu$m to an elliptical beam shape to match the vertical beam size of the transport beams. The beam parameters, polarizabilities and trapping frequencies are listed in Table 3.2.

In April 2022, we replaced the 1550-nm beam path with 1064 nm derived from the Mephisto MOPA 18W. Historically, we used the 1550-nm light because we hoped that the light would be red detuned from any electronic transition of ground-state molecules

Table 3.2 – Details of the 1550/1064-nm crossed optical dipole trap. The polarizabilities of the atoms are obtained from Equation (3.9). The polarizability for the NaK* Feshbach molecules can derived from the atom-pair approximation in Equation (3.10) as no photoassociation lines are expected at 1550 nm and 1064 nm. The polarizability of the NaK ground-state molecules is taken from Ref. [118]. The tabulated trap depths and trap frequencies are given for the power P_{1064} =0.73 W of 1064-nm and P_{1550} =1.5 W of 1550-nm light, the typical trap powers before the optical evaporation. The values w_v and w_h are the beams waists in the vertical and horizontal direction with reference to the propagation direction of the beam, respectively.

Beam	Transport beam (1064 nm)	Crossing beam (1550 nm)
Beam waists (μm)	$(w_v, w_h) = (48, 100)$	$(w_v, w_h) = (52, 148)$
$\alpha_{\mathrm{K}}\,(\mathrm{Jm}^2/\mathrm{W})$	1.84×10^{-36}	1.16×10^{-36}
$\alpha_{\mathrm{Na}}\,(\mathrm{Jm}^2/\mathrm{W})$	7.21×10^{-37}	5.84×10^{-37}
$\alpha_{\mathrm{NaK}}\,(\mathrm{Jm}^2/\mathrm{W})$	1.85×10^{-36}	1.34×10^{-36}
Trap depth	$U/k_B\,(\mu\mathrm{K})$	
$U_{0,\mathrm{K}}$	23.2	
$U_{0,\mathrm{Na}}$	10.2	
U_{0,NaK^*}	33.5	
$U_{0,\mathrm{NaK}}$	23.8	
Trap frequencies	$(\omega_x, \omega_y, \omega_z)\,(\mathrm{Hz})$	
$\omega_{i,\mathrm{K}}$	$2\pi \times (99.4, 166.0, 447.3)$	
$\omega_{i,\mathrm{Na}}$	$2\pi \times (92.7, 137.2, 389.7)$	
$\omega_{i,\mathrm{NaK}^*}$	$2\pi \times (97.0, 156.1, 427.1)$	
$\omega_{i,\mathrm{NaK}}$	$2\pi \times (82.8, 132.0, 362.6)$	

[118, 133]. However, the 1550-nm has generally caused problems for the lifetime of the ground-state molecules, both in the former one-dimensional vertical lattice or in the three-dimensional lattice in the presence of the 1550-nm crossing beam. It should be noted that we have never figured out why the 1550-nm light was reducing the lifetime of the molecules.

3.4.2 785-nm trap

The 785-nm species-dependent dipole trap was implemented into our experimental setup to efficiently associate double-degenerate Bose–Fermi mixtures into molecules. As explained in Section 5.4, the association in the 1550/1064-nm crossed dipole trap led to an inefficient association of Feshbach molecules due to a bad overlap and strong collisional loss. The bad spatial overlap arises from the different quantum statistics of the Na and K atoms. When condensed, the size of the Na cloud decreases, and consequently the density significantly increases. To compensate for that and improve the overlap between the K and the Na atoms, we need to use a dipole trap that has comparably large polarizability for the K atoms.

Initially, we used the compression light to compress the Fermi gas but also to improve its degeneracy. In this case, the compression was performed in the horizontal directions by adiabatically compressing the fermions, which are sympathetically cooled by the Na atoms producing degenerate Fermi gases with a temperature of $T \sim 0.15\,T_F$. However, once we implemented a light sheet to also compress the Fermi gas along the vertical direction to density-match it with the BEC in all spatial directions, we did not manage to reduce the temperature below $T \sim 0.2\,T_F$. Irrespective of that, the density-matching by using a species-dependent dipole trap allowed us to create degenerate Feshbach molecules. In this section, I will mainly describe the 785-nm trap that was used for the degenerate Feshbach molecule association in Ref. [105] whose properties are tabulated in Table 3.3.

3.4.2.1 Selecting the wavelength

We need to find a wavelength that strongly confines the degenerate Fermi gas of K atoms compared to the BEC of Na atoms to match their densities. Since Na atoms have D-line transitions at a wavelength of about 589 nm [116], it is quite natural in our system to choose a near-infrared wavelength for the trap. Thus, we can tune the frequency of the trap to be arbitrarily close detuned from the D-lines in K atoms while the detuning from the D-lines of the Na atoms will always be large. At the same time, we need to ensure that the chosen wavelength does not lead to absorptive heating of the K atoms by the trap light.

In addition, we need to consider further that near-infrared wavelengths are in a frequency regime where both the Feshbach and ground-state molecules have optical transitions to other states. The light can lead to photoassociation of the Feshbach molecules. Such photoassociation lines have been measured by Jee Woo Park and colleagues in Ref. [134] from the NaK team at MIT. Similarly, for ground-state molecules one needs to be aware of optical transitions into the $A^1\Sigma^+$ or $b^3\Pi$ manifold. To get a preliminary idea of the spectrum, we can look at the polarizabilities of ground-state ^{23}Na^{39}K-molecules calculated in [118]. Using an isotope shift of $\Delta\lambda = -11\,\mathrm{cm}^{-1}$ (see Equation 3.31a in Ref. [135]), we can use the spectrum for our fermionic molecules.

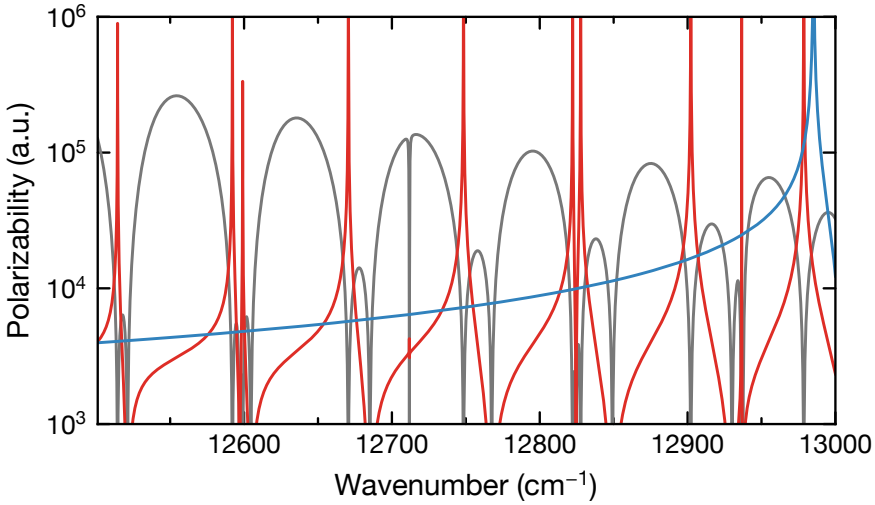

Figure 3.4 – Polarizabilities of ^{23}Na^{39}K molecules. The absolute value of the real part of the polarizabilities is shown for molecules in the absolute ground (red) and the Feshbach state (blue). The gray line shows the ratio of the real-to-imaginary polarizability for the ground-state molecules. The intersections of the red and blue lines can be referred to as magic frequencies between ground-state and Feshbach molecules. The data has been provided to us by Nadia Bouloufa-Maafa [119] and can be adapted to ^{23}Na^{40}K molecules, when shifting the data by $\Delta\lambda = -11\,\mathrm{cm}^{-1}$. Note that the polarizability of Feshbach molecules is plotted in absence of photassociation lines. Such photoassociation lines have been measured in Ref. [134]. The polarizabilities are given in atomic units (a.u.) where $1\,\mathrm{a.u.} = h \times 4.6883572 \times 10^{-2}\,\mathrm{Hz}/(\mathrm{W}/\mathrm{cm}^2)$.

Ultimately, we chose to work with a frequency that produces the same potential for the Feshbach and ground-state molecules. In this case the trap depth does not need to be adjusted when transferring the Feshbach molecules into the rovibronic ground state. Thus, we have measured the effect of the compression light on the Fermi degeneracy for various magic frequencies, and only for the magic frequency at around 775 nm did we notice a heating effect on the K atoms. Eventually, we made the choice to use a wavelength of $\lambda = 785.45\,\text{nm}$ for the compression which provides sufficient confinement for the K atoms to allow for the density matching for efficient Feshbach-molecule association. The parameters for the trap are tabulated in Table 3.3.

3.4.2.2 The optical setup

The species-dependent optical trap comprises a vertical beam and a light sheet. The light for the trap is generated by a titanium-sapphire laser (Coherent MBR 110) pumped at 532 nm with a Lighthouse Sprout. The wavelength can be tuned freely by tens of nanometers by changing the birefringence filter on the laser. This was advantageous for the starting phases of the project where we tried to find the optimal wavelength for the compression of the K atoms.

The light sheet which provides the vertical confinement for the mixture is based on the optical setup of the cap beams that Renhao Tao built during his Master's thesis in our experiment [136]. This setup was used during the investigation of the sticky collisions in a box trap formed by a ring beam and two cap beams [137]. After this project had been completed, we adapted the optical setup, in particular, we removed the mask which was used to create the cap beams and inserted a telescope to increase the enlarge the vertical waist of the light sheet. Using an imaging system and a Raspberry-Pi camera (Pi Camera NoIR V2), we monitor the position of the trap and obtain the beam parameters.

The compression beam that provides the confinement in the horizontal direction propagates along the vertical direction and is focused onto the atoms by a high-resolution objective. This beam propagates close to the optical axis of the imaging system such that it hopefully only has a small angle with the vertical axis. To align the compression beam independently from the imaging path, we had to insert a D-shaped mirror into the imaging path. The sharp edge on the left hand side in Figure 3.5a results from the D-shaped mirror obstructing a part of the image. Due to the spatial constraints in the optical setup, our main strategy to obtain the beam parameters is from the trapping frequencies.

3.5 Absorption imaging and analysis

After performing the experiment of interest, we destructively detect our atomic and molecular samples by absorption imaging. The sample is released from the trap and illuminated with a short light pulse after time of flight. The atoms absorb a part of the light pulse and create a shadow that is imaged onto a CCD camera (Allied Vision Manta G-145). We have built up different image paths for absorption imaging: The absorption images of atoms in the main chamber are predominantly used to determine and improve the atom numbers up

Table 3.3 – Details of the 785-nm crossed optical dipole trap. The polarizabilities of atoms are obtained from Eq. (3.9) whereas the polarizability of the Feshbach molecules from the atom-pair approximation. The polarizability of the ground-state molecules is assumed to be the same as for the Feshbach molecules. The tabulated trap depths and trap frequencies are given for a power of 20 mW in the vertical beam and 200 mW in the light sheet, the conditions for the trap in which we associate degenerate Feshbach molecules.

Beam	Vertical beam (785.45 nm)	Lightsheet (785.45 nm)
Beam waists (μm)	$(w_x, w_y) = (57, 45)$	$(w_z, w_x) = (30, 450)$
$\alpha_{\mathrm{K}}\,(\mathrm{Jm}^2/\mathrm{W})$	2.13×10^{-35}	
$\alpha_{\mathrm{Na}}\,(\mathrm{Jm}^2/\mathrm{W})$	1.14×10^{-36}	
Trap depth	$U/k_B\,(\mu\mathrm{K})$	
$U_{0,\mathrm{K}}\,(\mu\mathrm{K})$	1.5	
$U_{0,\mathrm{Na}}\,(\mu\mathrm{K})$	0.11	
$U_{0,\mathrm{NaK}^*}\,(\mu\mathrm{K})$	1.4	
Trap frequencies	$(\omega_x, \omega_y, \omega_z)\,(\mathrm{Hz})$	
$\omega_{i,\mathrm{K}}$	$2\pi \times (72.0, 90.1, 187.2)$	
$\omega_{i,\mathrm{Na}}$	$2\pi \times (22.8, 28.8, 62.1)$	
$\omega_{i,\mathrm{NaK}^*}$	$2\pi \times (60.0, 73.8, 153.5)$	

until the loading of the transport beam. For the experiments performed in the glass cell, we have imaging paths to detect the sample from the vertical and horizontal direction as shown in Figure 3.5.

3.5.1 Optical density

To obtain the thermometric quantities of our atomic and molecular samples, we first need to obtain the optical density. According to the Beer-Lambert law, the two-dimensional image of the optical density $OD(x,y)$ is given by

$$OD(x,y) = -\ln\left(\frac{A(x,y)-D(x,y)}{L(x,y)-D(x,y)}\right) \tag{3.12}$$

using three different images: an image with atoms in the presence of the imaging beam $A(x,y)$, the image without atoms in the presence of the imaging beam $L(x,y)$, and the dark image $D(x,y)$ without the atoms and the imaging beam. Note that the coordinates $\{x,y\}$ take discrete values as the camera that images the cloud is discretized by its pixels. It is important to take the dark image $D(x,y)$ to account for the ambient light, which the atoms might not absorb but impinges on the CCD camera. We can obtain the column-integrated averaged density of the sample in a pixel by

$$n(x,y) = OD(x,y)/\sigma, \tag{3.13}$$

where $\sigma = \sigma_0/(1+\delta^2)$ is the scattering cross-section which depends on the detuning Δ compared to the natural linewidth Γ, specifically $\delta = 2\Delta/\Gamma$. The scattering cross-section for resonant light of wavelength λ_0 is given by $\sigma_0 = 3\lambda_0^2/(2\pi)$. These relations can be obtained from a calculation of a two-level system and are valid in the regime where the probe intensity is much smaller than the saturation intensity $I_{\text{sat}} = (\hbar\omega^3\Gamma)/(12\pi c^2)$.

However, working with low imaging intensities constitutes a problem when working with dense atomic clouds. Most of the light then gets absorbed by the cloud and only a small fractions of the photons impinge onto the CCD camera. In this case, we cannot reliably obtain the optical density shot noise and readout noise. Instead, we image the sample with light intensities $I \gtrsim I_{\text{sat}}$. To account for saturation effects, we rewrite Equation (3.12) [138] as

$$OD(x,y) = -\ln\left(\frac{A(x,y)-D(x,y)}{L(x,y)-D(x,y)}\right) + \left(\frac{(L(x,y)-A(x,y))E_{\text{photon}}\, g_{\text{CCD}}}{T_{\text{light}}\,(I_{\text{sat}}/A_{\text{px}})\, t_{\text{pulse}}}\right), \tag{3.14}$$

where T_{light} is the ratio of the light after passing through the cloud that is transmitted to the camera, $I_{\text{sat}}/A_{\text{px}}$ is the light power over the pixel area A_{px} which is determined by the magnification M and the size of a pixel by $A_{\text{px}} = (l_{\text{px}}/M)^2$ for a square pixel. t_{pulse} is the duration of the pulse, $E_{\text{photon}} = h\nu$ is the energy per photon with imaging frequency ν, and g_{CCD} is the gain of the CCD-camera at the specific wavelength used.

To obtain the optical density in the glass cell for the atoms according to Equation (3.14),

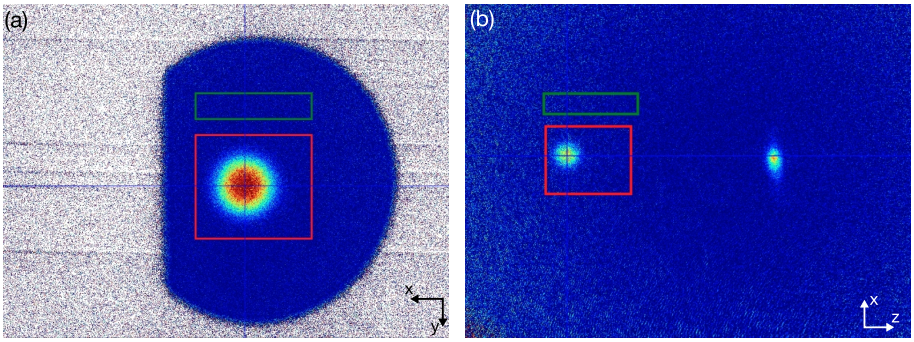

Figure 3.5 – Example pictures of the optical density in the vertical and horizontal imaging as shown by the image analyzer. (a) Vertical imaging of a thermal K cloud. The image shows the optical density image $OD(x,y)$ for a K cloud after evaporation in the crossed optical dipole trap after a time of flight of 20 ms. The aperture of the image clipped along the path of the imaging. The straight cut on the left-hand side results from a D-shaped mirror which sends the vertical compression beam for K atoms into the glass cell. (b) Horizontal imaging of Feshbach molecules and Na atoms with a small condensed fraction. Using a Stern–Gerlach technique, molecules and atoms are separated during time of flight. After the molecules are dissociated, the absorption image is taken, allowing us to detect Feshbach molecules and residual atoms simultaneously. The image is taken after a time of flight of 18 ms. The red boxes indicate the region of interest (ROI) and the green boxes indicate the reference region. The reference region is used to get the background reading of the optical density. The colors of the image indicate the optical density of the sample and are displayed here in arbitrary units.

we assume $T_{\text{light}} = 0.92$ given a 4%-reflection of the imaging power from the inner and outer surface of the glass cell on the imaging path. The length of the imaging pulses for both atomic species is t_{pulse} =50 µs, the saturation intensities are I_{sat} =1.75 mW/cm^2 [117] and I_{sat} =13.4 mW/cm^2 [116] for K and Na atoms, respectively. The atoms are typically imaged on resonance on the D_2-line for the respective species. Before any important measurement, we calibrate the imaging frequencies to maximize the atom number. For the analysis, however, we assume the imaging wavelength to be $\lambda_{\text{Na}} = 589.16\,\text{nm}$ and $\lambda_{\text{K}} = 766.70\,\text{nm}$. We also assume that the gain of both cameras is the same and that it solely depends on the wavelength, such that $g_{\text{CCD}}(\text{K}) = 0.078\,\frac{\text{counts}}{\text{photon}}$ and $g_{\text{CCD}}(\text{Na}) = 0.109\,\frac{\text{counts}}{\text{photon}}$.

We can image the K and the Na atoms in time of flight for both imaging paths. The absorption images $A(x,y)$ are taken for each species individually. Unless stated differently, the image of the K atoms is taken first, and the image of the Na atoms is taken 1 ms later. We typically specify the time of flight for the image of the K atoms. The images without atoms $L(x,y)$, and the dark image $D(x,y)$ are taken once the atoms have fallen out of the view of the imaging system and once the light has turned off, respectively. While both the vertical and horizontal imaging directions provide complementary information on the samples, we specifically use the horizontal imaging for the simultaneous detection of Feshbach molecules and atoms, which is particularly important in the characterization of the Feshbach association discussed in Chapter 5 and Chapter 6.

3.5.2 Imaging molecules

While I previously discussed how we could infer the optical density from the atoms, I would like to explain how we image the molecules in our experiment. To this end, it is important to note that the Feshbach nor the ground-state molecules are directly imaged in time of flight. As shown for ground-state molecules in Figure 3.6, we first perform the experiment of interest given by the time after the first STIRAP pulse. We then transfer the ground-state molecules into Feshbach molecules (second STIRAP pulse), after which the dipole traps for confining the molecules are turned off. Shortly after turning off the trap, we pulse on a magnetic field gradient of typically 40 G/cm, which separates the atoms from the Feshbach molecules. The magnetic field during this so-called Stern–Gerlach separation, typically between 72.3 G, is chosen such that the magnetic moment of the Feshbach molecules is considerably weaker than the atoms (see Figure 3.10). After the separation in time of flight, the magnetic-field gradient is turned off, and the magnetic field is ramped back through the Feshbach resonance to dissociate the molecules. Afterward, the magnetic field is turned off, and the imaging beams are pulsed for detection. The sequence shown in Figure 3.6 in the absence of the STIRAP pulses can also be understood as the turn-off sequence to detect Feshbach molecules.

3.5.3 Atom and molecule numbers

The two-dimensional images for the optical density $OD(x,y)$ allow us to deduce important quantities of the atomic and molecular clouds. We obtain the number of particles N by summing $OD(x,y)$ over the number of pixels i in the region of interest according to

$$N = \sum_i \frac{OD(x,y)A_{\mathrm{px}}}{\sigma}, \tag{3.15}$$

where σ is the scattering cross-section of the species of interest. Essentially, Equation (3.15) assumes a uniform column-integrated density $n^{(\mathrm{col})} = OD(x,y)/\sigma$ for each pixel, which is a reasonable assumption if the cloud extends over a sufficient number of pixels. Note that using this formula, we obtain the number of K and Na atoms, and the number of Feshbach molecules if we assume that the loss during the dissociation is negligible. For ground-state molecules, we need to correct the number of atoms by the STIRAP efficiency, e.g., the number of molecules from the image of K atoms is $N_{\mathrm{NaK}} = N_{\mathrm{K}}/\eta$. One downside of the horizontal imaging system is that we cannot obtain reliable atom numbers for Na and K atoms from the same experimental run. Given that we work with Na atoms in $m_F = 1$ and K atoms in $m_F = -9/2$, we need opposite polarizations for the imaging beams to image both atoms on their respective cycling transition. However, the imaging beams are combined in such a way that they have the same polarization. We can choose which species we want to image on a cycling transition by changing the direction of the horizontal bias fields. In the vertical imaging direction this is not needed. There the polarizations are of opposite direction and the different parity produces correct numbers for Na and K atoms.

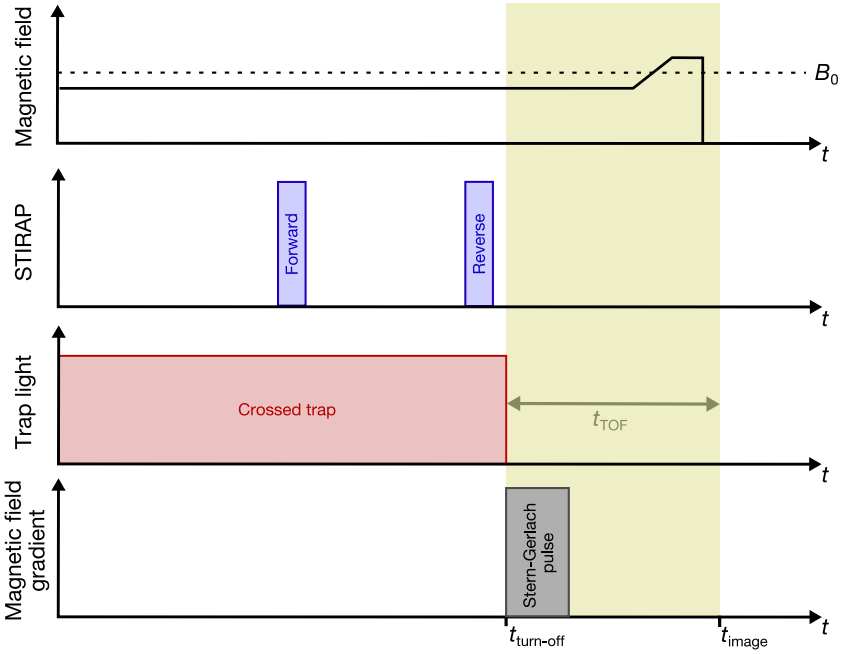

Figure 3.6 – Sketch of a typical sequence to image ground-state molecules. Starting with Feshbach molecules at a magnetic field below the Feshbach resonance ($B < B_0$) in an optical crossed dipole trap, the Feshbach molecules get transferred into the rovibronic ground-state by a forward STIRAP pulse. After the measurement, the molecules are transferred back into Feshbach molecules which are released from the trap. The traps are turned off at $t_{\mathrm{turn-off}}$, starting the time of flight. During the time of flight, we turn on a magnetic field gradient for a short time, exerting a force on the atoms different than that on the Feshbach molecules to separate the two samples. After some time of flight, the magnetic field is ramped above the Feshbach resonance. Shortly after, the magnetic field gets turned off, and the K atoms are imaged at t_{image}. The expansion time is given by $t_{\mathrm{TOF}} = (t_{\mathrm{image}} - t_{\mathrm{turn-off}})$.

3.5.4 Thermal clouds

The momentum distribution of thermal atoms is described by a Gaussian distribution. To probe thermal clouds, we fit the images $OD(x,y)$ with a Gaussian distribution of the form

$$OD_{\text{Gauss}}(x,y) = OD_{\text{peak}} \exp\left[-\frac{(x-x_c)^2}{2\sigma_x^2} - \frac{(y-y_c)^2}{2\sigma_y^2} \right], \tag{3.16}$$

where OD_{peak} is the amplitude of the Gaussian, (x_c, y_c) are coordinates of the cloud center and (σ_x, σ_y) describe the cloud widths. In our fitting routines, we typically fit the set of parameters $(OD_{\text{peak}}, x_c, y_c, \sigma_x, \sigma_y)$. Using the Gaussian width σ_i in the direction i, we obtain the temperature of the sample T_i with

$$T_i = \frac{m\omega_i^2\sigma_i^2}{k_B(1+\omega_i^2 t_{\text{TOF}}^2)}, \tag{3.17}$$

where m is the mass of the species of interest, t_{TOF} the expansion time of the sample, and k_B is the Boltzmann constant. Here, ω_i is the trapping frequency of the sample in the i-th direction.

For the temperature of the molecules, it is important to note that if the molecule dissociation is slow enough, the momentum distribution is still determined by the time of the release from the trap before the dissociation. Thus the temperature in Equation (3.17) is calculated for a mass $m = m_{\text{NaK}}$. However, the temperature might be overestimated if the dissociation of Feshbach molecules is too fast and the dissociation energy influences the momentum distribution [139].

3.5.5 Degenerate bosons

When the temperature of a bosonic sample is below the temperature of condensation $T < T_c$, the bosons follow a bimodal distribution with a thermal and condensed fraction. We fit the images $OD(x,y)$ with a bimodal distribution of the form

$$OD_{\text{bimodal}}(x,y) = OD_{\text{Gauss}}(x,y) + OD_{\text{BEC}} \,\text{Max}\left[0, \left(1 - \left(\frac{x-x_c}{R_x}\right)^2 - \left(\frac{y-y_c}{R_y}\right)^2\right)^{3/2}\right], \tag{3.18}$$

where $OD_{\text{Gauss}}(x,y)$ is the Gaussian distribution from Equation (3.16) for the thermal fraction, OD_{BEC} is the peak density, (x_c, y_c) is the center position of the condensed cloud and (R_x, R_y) are the Thomas-Fermi radii of the condensed bosons. Our fitting ensures that the momentum distribution of the BEC, described by an inverted parabola, is always positive. We obtain the number of thermal bosons N_{th} and the number of atoms in the BEC N_{BEC} [140]

by

$$N_{\mathrm{th}} = (2\pi)\frac{OD_{\mathrm{peak}}}{\sigma_0}\sigma_x\sigma_y, \tag{3.19}$$

$$N_{\mathrm{BEC}} = \left(\frac{8\pi}{15}\right)\frac{OD_{\mathrm{BEC}}}{\sigma_0}R_xR_y, \tag{3.20}$$

where σ_0 is the scattering cross section of the bosons. To get the temperature of the sample, we use the Gaussian widths to the thermal distribution and get temperature according to Equation (3.17).

3.5.6 Degenerate fermions

Once the fermions become degenerate, typically for $T \lesssim 0.6T_F$, their momentum distribution deviates from a Gaussian distribution, and a fit of a degenerate Fermi gas with a Gaussian distribution leads to an overestimation of the temperature due to Fermi pressure. To account for Fermi statistics, we fit the fermionic samples with a Fermi–Dirac distribution

$$OD_{\mathrm{FD}}(x,y) = OD_{\mathrm{FD}} \cdot \mathrm{Li}_2\left(-\zeta\, OD_{\mathrm{Gauss}}(x,y)\right), \tag{3.21}$$

where OD_{FD} is the amplitude, $\mathrm{Li}_2(x)$ is the dilogarithmic function, ζ the fugacity, (x_c, y_c) are coordinates of the cloud center and σ_x, σ_y are the Gaussian width of the cloud. Note, when $\zeta \to 0$, the fitting function approaches a Gaussian distribution. Thus, Equation (3.21) can be used to fit both degenerate and thermal fermionic clouds. We fit the set of parameters $(OD_{\mathrm{FD}}, \zeta, x_c, y_c, \sigma_x, \sigma_y)$ and obtain the reduced temperature from the relation

$$(T/T_F)^3 = -1/(6 \cdot \mathrm{Li}_3(-\zeta)), \tag{3.22}$$

while the absolute temperature in the direction i is extracted according to Equation (3.17). We note the degeneracy of the Fermi gas is extracted mainly from the shape of the cloud. As discussed in Section 5.7, particle loss, for example due to inelastic collisions of molecules, can lead to holes in the Fermi sea. However, since the momentum distribution for noninteracting Fermi gases does not change, the fitted degeneracy does not actually represent the degeneracy of the Fermi gas.

For the microwave-shielding project discussed in Section 5.8, where we evaporate ground-state molecules into the deeply degenerate regime, we have adapted the fitting function in Equation (3.21) [141]. Making use of the detected numbers of fermions and the geometric-mean trapping frequency, we calculate the Fermi temperature according to Equation (2.42) and use the fitting function

$$OD_{\mathrm{FD}'}(x,y) = OD_{\mathrm{FD}'} \cdot \mathrm{Li}_2\left(-\zeta\left(\frac{\bar{T}}{T_F}\right) OD_{\mathrm{Gauss}}(x,y)\right), \tag{3.23}$$

where $\zeta(\bar{T}/T_F)$ is the fugacity based on temperature of the sample $\bar{T} = (T_xT_yT_z)^{1/3}$ and the calculated T_F, and $OD_{\mathrm{Gauss}}(x,y)$ is the Gaussian distribution in Equation (3.16). We fit the

set of parameters $(OD_{\mathrm{FD}'}, x_c, y_c, \sigma_x, \sigma_y)$. Note that since the trapping frequencies and the time of flight are known, we can relate the cloud width σ_i and the temperature T_i in the i-th direction by Equation (3.17).

An advantage of using this fitting function is that small aberrations in the image and shot-to-shot fluctuations do not strongly influence the fitting. With a smaller number of fitting parameters, the error bars in the fitting strongly reduced especially in the regime where the number of molecules in the image was low.

Within the microwave-shielding project, we also investigated another method to fit the wings of degenerate Fermi gases by a Gaussian distribution which has been previously used in Ref. [142]. The idea is that while the low momentum states are dominated by Fermi pressure, the high-momentum states still follow a thermal distribution. The procedure includes fitting the image $OD(x,y)$ with Equation (3.16) and extracting the Gaussian widths σ_x, σ_y. We then exclude the region in image where $(x-x_c)^2+(y-y_c)^2 > (1.5\cdot \mathrm{Max}[\sigma_x,\sigma_y])^2$, and fit the image with the excluded region $OD_{\mathrm{wings}}(x,y)$ with a Gaussian function.

Last, a word of caution: When fitting double-degenerate Bose–Fermi mixtures, it is important to perform the time of flight at a magnetic field where the interspecies interactions are small. In our case, we perform the time of flight at the zero-crossing of the interspecies scattering length at a magnetic field of 80.3 G. In the presence of a BEC, the attractive or repulsive interactions strongly influence the density profile of the fermions in time of flight. In such a case, the cloud shape of the Fermi gases are strongly influenced by the interspecies interactions.

3.6 Characterizing the 78.3-G Feshbach resonance

We have decided to implement magnetoassociation on the 78.3-G s-wave Feshbach resonance between Na atoms in $|1,1\rangle$ and K atoms in $|9/2,-9/2\rangle$. We choose to work with these two hyperfine states because both atoms are in their respective hyperfine stretched state. Thus, the lifetime in this mixture is on the order of ten seconds when the mixture is weakly interacting. The Feshbach resonances accessible with our magnetic-field coils and with this combination of hyperfine states are at magnetic fields of 78.3 G and 89.7 G. While we used the bound state of the 89.7 G-resonance for radio-frequency association, the Feshbach resonance at 78.3 G is considerably more suitable for magnetoassociation. First, it has a resonance width of 5.3 G compared to 9.4 G for the 89.7-G Feshbach resonance. The smaller width allows us to ramp over the Feshbach resonance more quickly while maintaining good control over the interactions. Second, since we need to prepare the Bose–Fermi mixture above 78.3 G for the association, we can tune the interactions and even the sign of the interactions between bosons and fermions as illustrated in Figure 3.9. Consequently, this allows us to perform time of flight at the zero-crossing of the scattering length to obtain reliable thermometric quantities for the atomic mixture and molecules (see discussion at the end of the previous section). Moreover, we can do sympathetic cooling which is more efficient at repulsive than attractive scattering lengths. This section is based on our previous publication

[143].

3.6.1 RF-spectroscopy: Binding energy

In order to perform Feshbach association with the 78.3-G Feshbach resonance, we first need to characterize this resonance. Many of the NaK Feshbach resonances have been previously characterized by loss measurements [144]. Since some of the measured values significantly deviate from the theoretical predictions in [68], we decided to characterize the resonance by measuring the binding energy of the bound state that emerges at the 78.3-G Feshbach resonance.

We determine the magnetic-field dependence of the interspecies scattering length by characterizing the binding energy E_b via radio-frequency spectroscopy at various magnetic fields B between 73.5 G and 78.0 G. Using radio-frequency pulses, we measure the energy difference between molecules in the state $|FB\rangle$ and the atoms in $|A\rangle = |1,1\rangle_{\mathrm{Na}} + |9/2,-9/2\rangle_{\mathrm{K}}$.

Starting with an ultracold mixture of Na atoms in $|1,1\rangle$ and K atoms in $|9/2,-7/2\rangle$ in an optical dipole trap, we can apply a radio-frequency pulse at a given frequency ν to probe a transfer $|9/2,-7/2\rangle \rightarrow |9/2,-9/2\rangle$. Afterward, we turn off the trapping light and separate the K atoms in the state $|9/2,-9/2\rangle$ from the K atoms in $|9/2,-7/2\rangle$ with a magnetic field gradient and detect the number of atoms in both states with absorption imaging. This is needed to obtain the dissociation threshold ν_A. Moreover, we can use ν_A to calibrate the magnetic field. To this end, we compare the ν_A to the expected transition frequency from $|9/2,-7/2\rangle$ to $|9/2,-9/2\rangle$ which is given by the Breit-Rabi formula [145].

The radio-frequency spectroscopy of the weakly bound Feshbach-molecule state $|FB\rangle$ relies on the atom-dimer loss of Feshbach molecules and unbound atoms. By driving the transition $|9/2,-7/2\rangle \rightarrow |FB\rangle$, we associate atoms into molecules that can undergo loss. As we continuously drive this transition and associate atoms into molecules with each Rabi cycle, the loss depletes the detected number of atoms. After that, we release the atoms from the trap and detect the remaining number of unbound Na and K atoms. Since the association of molecules becomes less efficient with increasing binding energy, we increase the length of the radio-frequency pulse and ensure that the lost fraction of the Na and K atoms remains larger than 10% to obtain a detectable signal.

From the radio-frequency spectra, we determine the binding energy of the Feshbach molecules for each magnetic field. The example in Figure 3.7 shows a measurement of the binding energy at 76.5 G. We assume that the number of atoms that get lost in atom-dimer collisions scales proportionally with the number of formed molecules N_{mol}. In this case, the line shape of the radio-frequency spectrum of the bound state can be modeled via Fermi's golden rule as [146]

$$N_{\mathrm{mol}}(\nu) \propto \int_0^\infty \mathrm{d}\varepsilon_r F(\varepsilon_r) h(\varepsilon_r) e^{-(h\nu - E_b - h\nu_A - \varepsilon_r)^2/\sigma^2}. \tag{3.24}$$

Here, ν is the radio-frequency, and $h\nu_A$ is the atomic transition energy. The molecule number N_{mol} is proportional to the product of $h(\varepsilon_r)$, which is the number of colliding pairs per relative kinetic energy interval ε_r, and the Franck–Condon factor $F(\varepsilon_r)$ between the unbound atom

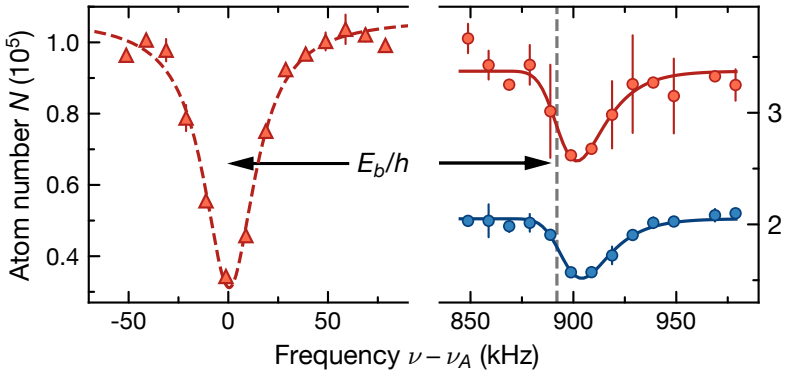

Figure 3.7 – Radio-frequency spectrum to determine the binding energy at 76.5 G. The remaining number of K atoms in the $|9/2,-7/2\rangle$ state from the radio-frequency transfer (red triangles) to the $|9/2,-9/2\rangle$ state at ν_A and its fit (red dashed line) are shown on the left. On the right, the remaining numbers of K atoms (red circles) and Na atoms (blue circles) from radio-frequency loss spectroscopy of the weakly bound Feshbach state $|FB\rangle$ and their fits (red and solid blue lines) are shown. The vertical gray dashed line indicates the transition frequency to $|FB\rangle$ extracted from Equation (3.24) for atoms at rest. The radio-frequency spectrum of $|FB\rangle$ is given relative to the dissociation threshold ν_A.

pair and the bound molecular state. The product is convolved with a Gaussian distribution with the width σ to account for the finite energy resolution. We adapt the simplified Franck–Condon factor $F(\varepsilon_r) \propto \sqrt{\varepsilon_r}(1+\varepsilon_r/E_b)^{-2}$ from Ref. [147]. The function $h(\varepsilon_r)$ is proportional to the Boltzmann factor $e^{-\varepsilon_r/k_BT}$, where the temperature T of the atomic cloud is obtained from time-of-flight images. According to Equation (3.24), we fit functions to the lost number of atoms in the radio-frequency spectra of the bound state, as demonstrated in Figure 3.7. Note that the relative kinetic energy of the associated atoms has to be transferred into the microwave field and therefore increases the transition frequency. The binding energies E_b that we extract from these fits are presented in Figure 3.8 as a function of the magnetic field.

3.6.2 Model for overlapping Feshbach resonances

To determine the scattering length from the binding energy near the interspecies Feshbach resonance, we adapt the model for overlapping Feshbach resonances from Ref. [148] to include the resonance at 89.7 G. The binding energy is given by solving

$$\frac{\sqrt{2\mu E_b}}{\hbar} = \frac{1}{a_{\mathrm{bg}} - \bar{a}} + \frac{1}{\bar{a}} \sum_{i=1,2} \frac{\Gamma_i}{E_b + E_i}, \tag{3.25}$$

where E_1 and E_2 are the energies of the bare molecular state for the resonance at 78.3 G and 89.7 G, respectively, a_{bg} is the background scattering length, $\mu = m_{\mathrm{Na}} m_{\mathrm{K}}/(m_{\mathrm{Na}} + m_{\mathrm{K}})$ is the reduced mass in a Na-K collision, $\bar{a} = 4\pi\Gamma(1/4)^{-2} a_{\mathrm{vdW}} \approx 51\, a_0$ is the mean scattering length, where $\Gamma(x)$ is the gamma function and a_{vdW} is the van der Waals length. The energy

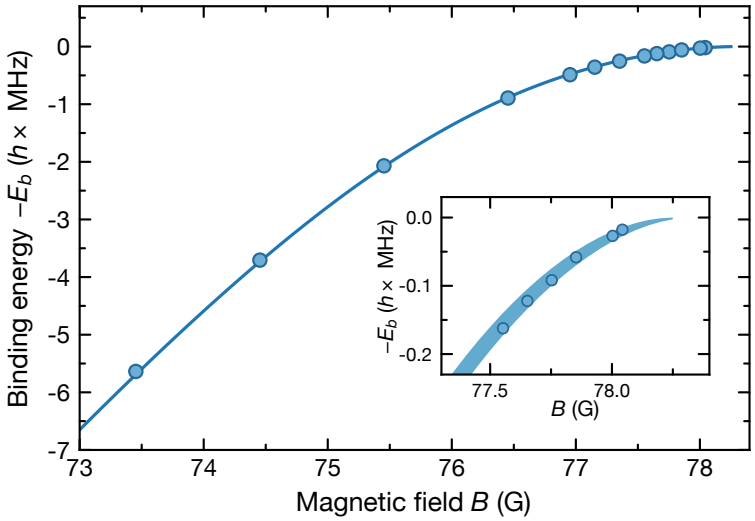

Figure 3.8 – Binding energy E_b of the Feshbach-molecule state $|FB\rangle$ as a function of the magnetic field. The circles mark the fit results from the radio-frequency spectra. The solid line shows the function of Equation (3.25) fitted to these data. Inset: Close-up for binding energies below 200 kHz. The uncertainty of the fit function is smaller than the thickness of the solid line in the main figure. However, it is resolved in the close-up. This uncertainty includes statistical errors of the fit and an uncertainty of 5% of the background scattering length $a_{bg} = -619(31)\,a_0$ [68].

Table 3.4 – Parameters of the Feshbach coupling strengths Γ_i, the differential magnetic moments $\delta\mu_i$, and the crossing of the bare molecular states with the dissociation threshold $B_{c,i}$ which are used to fit the model for overlapping Feshbach resonances described by Equation (3.25). Γ_1 is the only free fit parameter while the others are extracted from a coupled-channel calculation [149].

i	Γ_i/h (MHz)	$\delta\mu_i$ (μ_B)	$B_{c,i}$ (G)	B_i^* (G)	$B_{0,i}$ (G)
1	4.180(9)	1.894	73.92	73.034(4)	78.30(4)
2	1.385	2.085	80.58	80.358(1)	89.7(6)

of the bare molecular states can be tuned magnetically with $E_i = \delta\mu_i(B - B_{c,i})$, where $\delta\mu_i$ is the relative magnetic moment with respect to the dissociation threshold and $B_{c,i}$ is the magnetic field at which the bare molecular state crosses the dissociation threshold. The Feshbach coupling strengths between the open and closed channels are denoted by Γ_i. For an isolated resonance, the Feshbach coupling strength Γ is related to the commonly used Feshbach resonance width Δ as $\Gamma = 2\Delta\delta\mu\,\alpha^{-1}$, where $\alpha = (a - a_{\mathrm{bg}})^2/a_{\mathrm{bg}}\bar{a}$. For overlapping resonances, Γ_i cannot be independently extracted without considering nearby resonances. We fit Equation (3.25) to the binding-energy data to extract the parameters for the two resonances. To avoid overfitting, we take Γ_1 as the only free fit parameter while all other parameters are derived from a coupled-channel calculation [149]. The fitted binding energy is presented in Figure 3.8 as function of the magnetic field. The parameters are tabulated in Table 3.4.

The scattering length a is given by solving [148]

$$\frac{1}{a-\bar{a}} = \frac{1}{a_{\mathrm{bg}}-\bar{a}} + \frac{1}{\bar{a}}\sum_{i=1,2}\frac{\Gamma_i}{E_i}. \tag{3.26}$$

With the parameters extracted from Equation (3.25), we can compute the scattering lengths at different magnetic fields using Equation (3.26). We further rewrite the expression of the scattering length as

$$a(B) = a_{bg}\left(\frac{B-B_1^*}{B-B_{0,1}}\right)\left(\frac{B-B_2^*}{B-B_{0,2}}\right), \tag{3.27}$$

where $a_{bg} = -619\,a_0$ [68] is the background scattering length, $B_{0,1} = 78.3\,\mathrm{G}$ and $B_{0,2} = 89.7\,\mathrm{G}$ are the two resonance positions, and $B_1^* = 73.03\,\mathrm{G}$ and $B_2^* = 80.36\,\mathrm{G}$ are the zero-crossings of the scattering length [143]. The interspecies scattering length as function of the magnetic field is plotted in Figure 3.9.

As shown in Figure 3.10, we can also obtain the absolute energies of the unbound state and the molecular state as a function of the magnetic field. From these energies, we obtain the magnetic moment of the molecules at a specific field by taking the derivative of energy of the bound state shown in Figure 3.10. This knowledge is important to find a magnetic field for levitating the molecules against gravity using a magnetic field gradient. For example, at about 72.3 G the molecules have a vanishing magnetic moment, and close to resonance, the

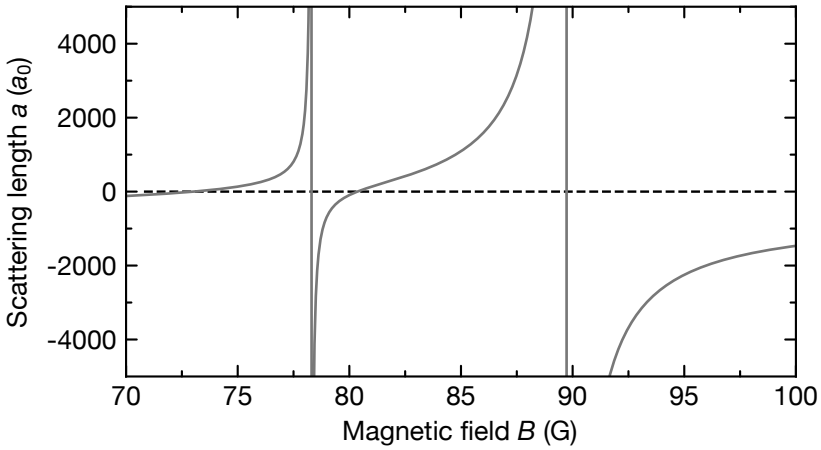

Figure 3.9 – Scattering length as a function of the magnetic field. The solid line shows the function of Equation (3.27).

magnetic moment approaches the sum of the atomic magnetic moments for Na and K atoms.

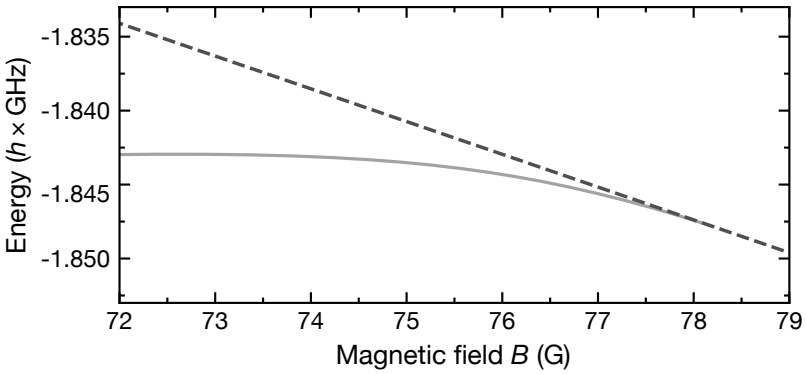

Figure 3.10 – Energies of bare atomic state and Feshbach-molecular state. The dashed line shows the energy of unbound atoms ($|1,1\rangle_{\mathrm{Na}} + |9/2,-9/2\rangle_{\mathrm{K}}$) relative to zero magnetic field where the hyperfine states are energetically degenerate. The energies are obtained from the Breit-Rabi formula [116, 117, 145]. The solid gray line shows the energy of the Feshbach molecules and is obtained by subtracting the binding energy from the bare atomic state.

"Pain is inevitable, suffering is optional"

—Buddhist proverb

4 Collisional loss around the 78.3-G Feshbach resonance

The resonant scattering behavior in the vicinity of Feshbach resonances leads to strong inelastic collisions. Hence, substantial particle loss can occur during the magnetoassociation of atoms into molecules, where the magnetic field is ramped through the Feshbach resonance. As discussed in Section 5.4, we observe that the inelastic collisions are a significant limitation for the Feshbach association efficiency in a double-degenerate Bose–Fermi mixtures due to the enhanced density of bosons. Since it is not clear *ab initio*, which of the collision processes (see Figure 4.1) limit the association efficiency, a considerable effort of my Ph.D. work was directed towards understanding the collisional properties in the Na-K system. To this end, we isolated and characterized the different loss processes close to the 78.3-G interspecies Feshbach resonance, which we use for the Feshbach association. The loss measurements presented in this chapter have been carried out in close collaboration with my co-worker Xingyan Chen. This chapter is based on the publications in Ref. [143, 150] for which we share the first authorship.

4.1 Three-body loss

We study the three-body loss, an inelastic collision process where two Na atoms and one K atom recombine in the short range to form a trimer that breaks up, leading to a deeply bound dimer and a residual Na atom. The kinetic energy of the break-up is sufficient for the atoms to leave the optical dipole trap. In this section, I will describe the characterization of the three-body loss as a function of the Na-K interactions described by the scattering length a. In addition, I will discuss the scaling of the three-body loss on the temperature T of the

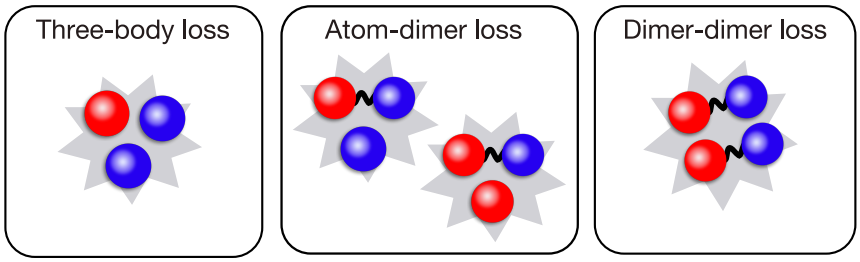

Figure 4.1 – Loss processes occurring during the magnetoassociation that were systematically studied in the course of this Ph.D. work. The Na atoms are shown in blue and K atoms are shown in red. NaK^*-molecules are illustrated with a wiggly line.

mixture and the reduced temperature of the Fermi gas T/T_F in the unitary regime.

4.1.1 Scattering-length dependence

To determine the inelastic three-body collisions, we measure the loss of the atoms in a crossed optical dipole trap as a function of the magnetic field for different hold times. The measurement begins with a trapped mixture of 3×10^5 thermal Na atoms in $|F,m_F\rangle = |1,1\rangle$ and 1.5×10^5 K atoms in $|9/2,-9/2\rangle$ with $T = 0.6\,T_F$. The trapping frequencies for Na and K in the (x,y,z)-direction are $2\pi\times(88,141,357)$ Hz and $2\pi\times(97,164,410)$ Hz, respectively. The interspecies scattering length is varied by tuning the magnetic field around a Feshbach resonance at 78.3 G. The relation between the magnetic field and the scattering length is given by Equation (3.27). To probe the loss for $a>0$ ($a<0$), we prepare the sample at weak interactions below (above) the resonance and ramp the magnetic field to the target value in about 100 µs. Before the ramp, a magnetic-field gradient is turned on to compensate for the gravitational sag between the atomic species to ensure spatial overlap. After a variable hold time, the magnetic field is ramped back within 100 µs to a zero-crossing of the interspecies scattering length close to the initial magnetic field. Subsequently, the atoms are released from the trap and both species are imaged after a time of flight. We obtain the temperature and atom number from the absorption images as described in Section 3.5.

In its simplest form the three-loss L_3 can be obtained by fitting the loss rates of Na and K atoms to the coupled differential equations

$$\frac{\mathrm{d}N_\mathrm{K}}{\mathrm{d}t} = \frac{1}{2}\frac{\mathrm{d}N_\mathrm{Na}}{\mathrm{d}t} = -L_3\int n_\mathrm{Na}^2(\boldsymbol{x})n_\mathrm{K}(\boldsymbol{x})\mathrm{d}^3\boldsymbol{x}, \tag{4.1}$$

where the density of the Na atoms $n_\mathrm{Na}(\boldsymbol{x})$ is given by a Gaussian distribution from Equation (2.31) as these measurements are performed with thermal Na clouds, and a Fermi–Dirac distribution for $n_\mathrm{K}(\boldsymbol{x})$ for the K atoms (see Equation (2.44)).

In addition to the model described by Equation (4.1), we account for anti-evaporative heating, secondary processes and evaporation, leaving us with the following set of differential equations:

$$\frac{\mathrm{d}N_\mathrm{Na}}{\mathrm{d}t} = -(2+\delta)L_3\int n_\mathrm{Na}^2(\boldsymbol{x})n_\mathrm{K}(\boldsymbol{x})\mathrm{d}^3\boldsymbol{x} + \left(\frac{\mathrm{d}N_\mathrm{Na}}{\mathrm{d}t}\right)_\mathrm{ev}, \tag{4.2}$$

$$\frac{\mathrm{d}N_\mathrm{K}}{\mathrm{d}t} = -L_3\int n_\mathrm{Na}^2(\boldsymbol{x})n_\mathrm{K}(\boldsymbol{x})\mathrm{d}^3\boldsymbol{x}, \tag{4.3}$$

$$\frac{\mathrm{d}T}{\mathrm{d}t} = \frac{(\frac{3}{2}-\beta)T+\frac{1}{3}T_h}{N_\mathrm{Na}+N_\mathrm{K}}L_3\int n_\mathrm{Na}^2(\boldsymbol{x})n_\mathrm{K}(\boldsymbol{x})\mathrm{d}^3\boldsymbol{x} + \left(\frac{\mathrm{d}T}{\mathrm{d}t}\right)_\mathrm{ev}. \tag{4.4}$$

Here, β describes the anti-evaporative heating due to the three-body loss, the parameter δ describes the secondary loss, T_h describes the secondary heating, and $\left(\frac{\mathrm{d}N_\mathrm{Na}}{\mathrm{d}t}\right)_\mathrm{ev}$ and $\left(\frac{\mathrm{d}T}{\mathrm{d}t}\right)_\mathrm{ev}$ give the contributions from evaporative cooling.

They anti-evaporative term in Equation (4.4) accounts for fact that the three-body loss predominantly takes place at the bottom of the trap where the density is the highest [151]

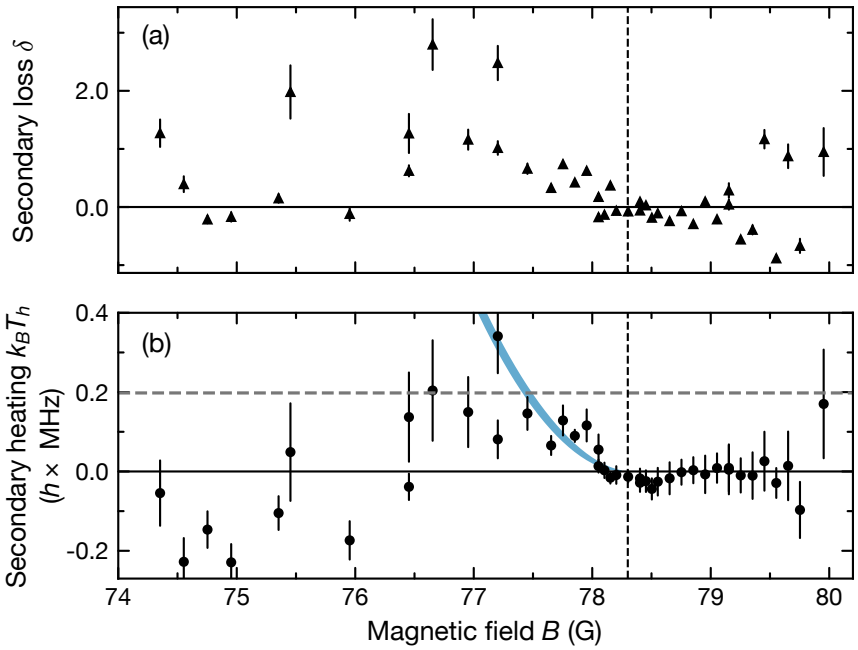

Figure 4.2 – Secondary loss and secondary heating as a function of the magnetic field B. (a) Additional average number of Na atoms that are lost per recombination event due to secondary collisions (black triangles). (b) Average excess energy deposited per recombination event due to secondary collisions (black points). The solid blue line represents the kinetic energy the Na atoms carry away from a three-body collision as given in Equation (4.6) and the gray dashed line indicates the trap depth of the Na atoms. The vertical dashed line marks the resonance position at 78.3 G.

and the energies of the particle are lower than the thermal average. We can account for the anti-evaporation by calculating the averaged potential energy lost per particle which is given by

$$\beta k_B T = \frac{\int n_{\mathrm{Na}}^2(\boldsymbol{x}) n_{\mathrm{K}}(\boldsymbol{x}) (2U_{\mathrm{Na}}(\boldsymbol{x}) + U_{\mathrm{K}}(\boldsymbol{x})) \mathrm{d}^3\boldsymbol{x}}{3 \int n_{\mathrm{Na}}^2(\boldsymbol{x}) n_{\mathrm{K}}(\boldsymbol{x}) \mathrm{d}^3\boldsymbol{x}}, \tag{4.5}$$

where $U_{\mathrm{Na}}(\boldsymbol{x})$ and $U_{\mathrm{K}}(\boldsymbol{x})$ are the trap depths for the respective species. The term in Equation (4.5) is smaller than the averaged thermal energy per particle $(3/2)k_B T$. This can be understood by considering that the integral in the nominator scales with the density of the atoms cubed and strongly favors the center of the trap.

Secondary processes occur when the products of the three-body recombination do not leave the trap and induce additional loss or heating. This process is allowed at scattering lengths $a > 0$ where a bound state with binding energy $E_b = \hbar^2/(2\mu a^2)$ is available, and a Na-Na-K collision leads to the formation of a weakly bound NaK* Feshbach molecule and a residual Na atom. Here, μ is the reduced mass in a Na-K collision process. The release of the binding energy is associated to the dimer formation, which is shared between the dimer and the residual Na atom [152]. Suppose the energy of the Feshbach molecule is lower

than the trap depth. In that case, it can remain in the trap and undergo a collision with an additional Na atom, forming a deeply bound dimer and a residual Na atom. This releases sufficient energy to expel the products from the trap, leading to secondary loss. Secondary loss predominantly affects Na atoms. The collisions between the trapped dimers and K atoms are suppressed by Pauli blocking between the K atom and the weakly bound K atom inside the dimer [153]. As a result of secondary losses, the loss ratio between Na and K atoms is 3:1. We account for the secondary loss with the term δ, chosen as a fitting parameter in the model. Secondary heating occurs when the Na atoms of the primary collision remain in the trap. The trapped Na can thermalize with the Na or K cloud and release an average energy of $k_B T_h$. The shallow dimers do not considerably contribute to secondary heating as inelastic collisions dominate. The extracted parameters for the secondary processes are shown in Figure 4.2. The effective trap depth for the Feshbach molecules in this experiment is $U_{\mathrm{NaK}^*} = h \times 0.5\,\mathrm{MHz}$. For magnetic fields above 75.5 G, the binding energy is comparable to the trap depth. As shown in Figure 4.2a, the average loss of Na atoms per recombination δ vanishes above the Feshbach resonance while it increases below the resonance until 75.5 G. In Figure 4.2b, the secondary heating T_h is compared to the kinetic energy of the Na atom after the recombination, which is given by

$$\frac{m_{\mathrm{Na}} + m_{\mathrm{K}}}{2m_{\mathrm{Na}} + m_{\mathrm{K}}} E_b. \tag{4.6}$$

We find that T_h qualitatively follows Equation (4.6) until it equals the trap depth of the Na atoms. For lower magnetic fields, T_h decreases again since the Na atom can escape the trap after recombination.

The evaporative cooling of Na atoms mitigates the anti-evaporative and secondary heating. Since the Na atoms experience a considerably shallower trap than the K atoms, they sympathetically cool the mixture via evaporation. We consider the evaporation of Na atoms initiated by both Na-Na and Na-K collisions. The evaporation of the Na atoms is then given by

$$\left(\frac{\mathrm{d}N_{\mathrm{Na}}}{\mathrm{d}t}\right)_{\mathrm{ev}} = -\gamma_1 \frac{N_{\mathrm{Na}}^2}{T} - \gamma_2 \frac{N_{\mathrm{Na}} N_{\mathrm{K}}}{T}, \tag{4.7}$$

$$\left(\frac{\mathrm{d}T}{\mathrm{d}t}\right)_{\mathrm{ev}} = -\frac{1}{3}(\xi + \kappa - 3) \frac{\gamma_1 N_{\mathrm{Na}} + \gamma_2 N_{\mathrm{K}}}{N_{\mathrm{Na}} + N_{\mathrm{K}}}, \tag{4.8}$$

$$\gamma_1 = \frac{8}{\pi} \frac{m_{\mathrm{Na}} \bar{\omega}_{\mathrm{Na}}^3}{k_B} a_{BB}^2 e^{-\xi} V_r, \tag{4.9}$$

$$\gamma_2 = \frac{4}{\pi} \frac{m_{\mathrm{K}} \bar{\omega}_{\mathrm{K}}^3}{k_B (a^{-2} + 2\mu U_{\mathrm{Na}} \hbar^{-2})} e^{-\xi} V_r, \tag{4.10}$$

$$\kappa = \left(1 - \frac{P(5,\xi)}{P(3,\xi)}\right) V_r, \tag{4.11}$$

$$V_r = \xi - 4 \frac{P(4,\xi)}{P(3,\xi)}, \tag{4.12}$$

where the first (second) term in Equation (4.7) accounts for evaporation induced by intraspecies (interspecies) collisions. Here $\xi = U_{\mathrm{Na}}/k_B T$ is the truncation parameter for Na, $P(a,\xi)$ is the regularized incomplete Gamma function

$$P(a,\xi) = \frac{\int_0^{\xi} u^{a-1} e^{-u} \mathrm{d}u}{\int_0^{\infty} u^{a-1} e^{-u} \mathrm{d}u}. \tag{4.13}$$

The intraspecies evaporation rate in Equation (4.7) follows from Refs. [154, 155] and is adapted for our case by replacing the collision cross section with $\sigma_{BB} = 8\pi a_{BB}^2$. Here a_{BB} is the intraspecies scattering length of Na. The interspecies evaporation between Na and K atoms (i.e., the sympathetic cooling) is obtained by using the Na-K collision cross section $\sigma_{BF} = 4\pi/(a^{-2} + k^2)$ [156] and replacing the density of Na atoms with the density of the K atoms. Since only collisions with relative kinetic energy larger than the trap depth lead to evaporation [155], we substitute $k \simeq \sqrt{2\mu U_{\mathrm{Na}}}/\hbar$ to obtain the energy-independent cross section $\sigma_{BF} = 4\pi/(a^{-2} + 2\mu U_{\mathrm{Na}}\hbar^{-2})$.

As shown in Figure 4.3, the loss and heating are well described by our model. Minor discrepancies between the data and the model are obtained when neglecting the secondary processes. However, when the evaporation term is ignored, the differences between the model and the data are significant. Secondary loss and secondary heating mainly contribute at short hold times where the three-body recombination rate is large. In contrast, the evaporation term becomes relevant with longer hold times and compensates for heating. We note that throughout the measurements, the loss ratio between Na atoms and K atoms is typically 2:1 or larger due to secondary processes. This strongly indicates that the Na-Na-K collisions are the primary three-body loss process. While three-body recombination of one Na atom and two K atoms is in principle possible, Pauli exclusion principle strongly suppresses this process.

Figure 4.4 summarizes the results of the three-body loss coefficient L_3 as a function of the interspecies scattering length a. The rate coefficient for three-body recombination changes by almost four orders of magnitude between the weakly interacting regime and the unitary regime, where the loss only shows a small dependence on the scattering length. We compare our results to the zero-range theory, which assumes contact interactions [152, 157]. The zero-range theory including finite temperature effects requires averaging over the collision energy distribution. We use the finite-temperature formula for $a < 0$ [157]:

$$L_3(a<0) = 4\pi^2 \cos^3\phi \, \frac{\hbar^7}{\mu^4 (k_B T)^3} \left(1 - e^{-4\eta}\right) \times \int_0^{\infty} \frac{1 - |s_{11}|^2}{|1 + (kR_0)^{-2is_0} e^{-2\eta} s_{11}|^2} \, e^{-\hbar^2 k^2/2\mu k_B T} \, k \, \mathrm{d}k. \tag{4.14}$$

The angle ϕ is defined by $\sin\phi = m_F/(m_B + m_F)$ and R_0 is the three-body parameter. The parameter η characterizes the inelasticity of the collisions. In particular, $(1 - e^{-4\eta})$ quantifies the probability that the incoming wave of the collision is not reflected, leading to loss. For Na-K $s_0 = 0.285$, which is a universal constant describing the Efimov energy spectrum, and

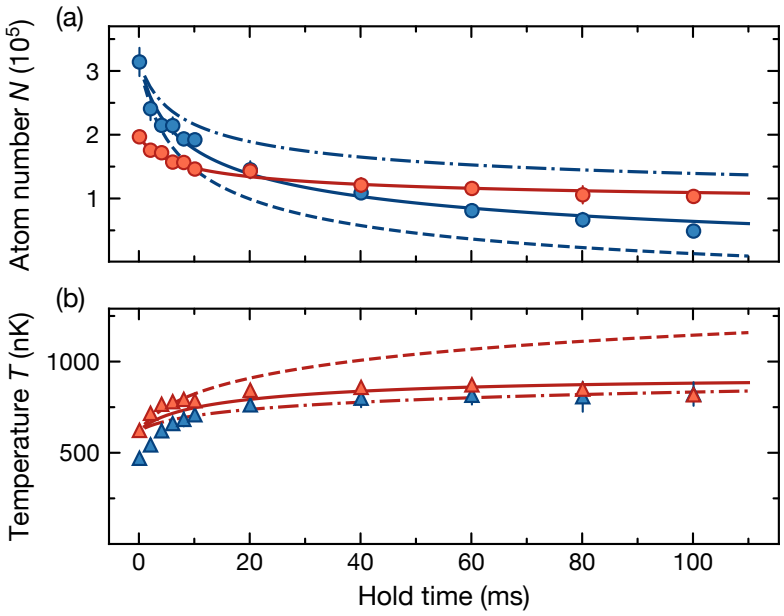

Figure 4.3 – Loss and heating of the atomic mixture at 77.8 G. (a) Atom number of Na (blue circles) and K (red circles) as a function of the hold time. (b) Temperature of Na (blue triangles) and K (red triangles) as a function of the hold time. The solid lines show a fit of the coupled differential equations described by Equations (4.2)-(4.4) where the temperature of the K atoms is assumed to be the temperature of the mixture. The dashed (dash-dotted) lines represent the same solution omitting the evaporation (secondary loss and secondary heating processes).

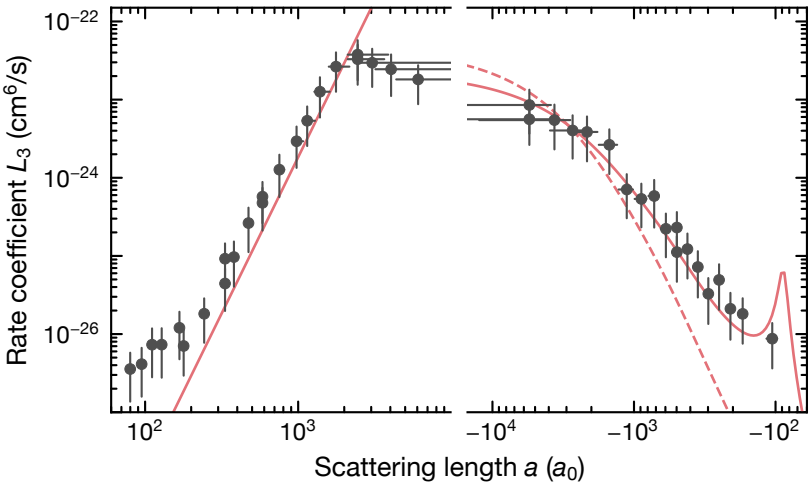

Figure 4.4 – Three-body loss coefficient L_3 versus interspecies scattering length a (gray points). The solid red line shows the numerical result of the fitted zero-range theory, which yields an inelasticity parameter $\eta = 0.02$ and a three-body parameter $R_0 = 70\,a_0$. The red dashed line shows the result with $\eta = 0.02$ but without including Efimov resonances. The error bars in the horizontal direction are a combination of the error resulting from the magnetic field instability of 30 mG and the uncertainty of the model to determine the interspecies scattering length from the magnetic field. The vertical error bars contain an uncertainty of 10% in the trapping frequency and a systematic error resulting from different temperatures of the Na and the K cloud.

s_{11} is a universal function that depends on the dimensionless interaction parameter ka and the mass ratio between the species (see Ref. [157] for more details). Here, k is the three-body collision wave vector which relates to the collision energy as $E_k = \hbar^2 k^2/2\mu$. In the unitary regime, the scattering length diverges and the de-Broglie wavelength determines the scattering properties, and Eq. (4.14) saturates to

$$l_3(E) = \frac{8\pi^2\hbar^4\cos^3\phi}{\mu^3 E^2}(1-e^{-4\eta}), \tag{4.15}$$

where E is the kinetic energy in the three-body center-of-mass frame [157, 158].

For $a > 0$, an analytic expression is not available and thus we use the zero-temperature formula [152]:

$$L_3(a>0) = C_\alpha\left(\frac{\sin^2[s_0\ln(a/a_+)]+\sinh^2\eta}{\sinh^2(\pi s_0+\eta)+\cos^2[s_0\ln(a/a_+)]} + \frac{\coth(\pi s_0)\cosh(\eta)\sinh(\eta)}{\sinh^2(\pi s_0+\eta)+\cos^2[s_0\ln(a/a_+)]}\right)\frac{\hbar a^4}{m_K}, \tag{4.16}$$

where a_+ marks the minima in L_3, typically associated with an Efimov resonance. The

regime we measured is away from any Efimov resonances so the term $\cos[s_0 \ln(a/a_+)]$ is set to zero and the term $\sin[s_0 \ln(a/a_+)]$ is set to one. We find that $\eta \approx 0.02$ and the three-body parameter $R_0 = 35\,a_0$ reproduce the loss in the universal regime on both sides of the resonance.

The fitted R_0 suggests an Efimov resonance at $|a| \approx 35\,a_0$, which is comparable to the van-der-Waals length $a_{\mathrm{vdW}} = 53.3\,a_0$, where the zero-range approximation breaks down and the universal scattering is modified [159–161].

4.1.2 Unitary three-body loss

In the unitarity regime, the three-body loss coefficient according to Eq. (4.15) saturates and scales as $L_3(T) \propto 1/T^2$, which has been confirmed experimentally in non-degenerate systems [155, 162]. While three-body recombinations involving identical particles are enhanced (suppressed) by bunching (anti-bunching) due to Bose [163–165] (Fermi [166, 167]) statistics, it remains an open question how Fermi statistics modify three-body recombination processes that involve only one fermion. Thus, we probe the unitary three-body loss as a function of temperature and Fermi degeneracy.

We use the same experimental sequence as in the previous section, but we fix the probe magnetic field to the pole of the Feshbach resonance. We vary T/T_F by changing the initial number of K atoms and the temperature while keeping the mixture in thermal equilibrium. To achieve the lowest possible T/T_F, we increase T_F by working with $\sim 4 \times 10^5$ K atoms and consequently $\sim 3 \times 10^4$ Na atoms. Since the fraction of lost K atoms is small, T/T_F is modified by less than 10% throughout the loss measurement. In the high-T/T_F regime, we reduce the number of K atoms down to $\sim 2 \times 10^4$. Here, T/T_F is changing during the loss measurement, however, a dependence of the three-body loss on T/T_F is not expected in this regime. The initial temperatures and trap parameters are chosen such that evaporation is negligible. Accordingly, we simplify the model and neglect the effects of anti-evaporative heating ($\beta = 0$). In addition, we consider the secondary processes to be negligible ($\delta = 0$, $T_h = 0$) since we measure resonance. While there was a small but significant difference in the initial temperature between the bosons and fermions in the previous measurements, we now ensure that the mixture is in thermal equilibrium.

The average loss coefficient in an atomic mixture is obtained by averaging over the collision energy distributions $f(E)$, according to

$$L_3 = \int l_3(E) f(E) \mathrm{d}E. \tag{4.17}$$

Here,

$$f(E) = \int \delta(\varepsilon_1 + \varepsilon_2 + \varepsilon_3 - E_{\mathrm{cm}} - E) \times f_B(\boldsymbol{k_1}) f_B(\boldsymbol{k_2}) f_F(\boldsymbol{k_3}) \mathrm{d}^3\boldsymbol{k_1} \mathrm{d}^3\boldsymbol{k_2} \mathrm{d}^3\boldsymbol{k_3}, \tag{4.18}$$

where $\delta(x)$ is the Dirac delta distribution, $f_B(k)$ is the Maxwell–Boltzmann distribution from Equation (2.25) for the Bose gas and $f_F(k)$ is the Fermi–Dirac distribution from Equation (2.39) for the Fermi gas. The kinetic energies of the particles involved are given by ε_i

and the energy in the center of mass E_{cm} is given by

$$\varepsilon_1 = \frac{\hbar^2 \boldsymbol{k_1}^2}{2m_B}, \quad \varepsilon_2 = \frac{\hbar^2 \boldsymbol{k_2}^2}{2m_B}, \quad \varepsilon_3 = \frac{\hbar^2 \boldsymbol{k_3}^2}{2m_F}, \tag{4.19}$$

$$E_{\mathrm{cm}} = \frac{\hbar^2 (\boldsymbol{k_1} + \boldsymbol{k_2} + \boldsymbol{k_3})^2}{2(2m_B + m_F)}. \tag{4.20}$$

To compare the loss for different temperatures, we define a temperature-independent loss coefficient $\Lambda = L_3/T^2$. As shown in Figure 4.5a, the measured rate coefficients are insensitive to changes in T/T_F when $T/T_F \gtrsim 1$. However, for $T/T_F < 1$, a reduction in T/T_F also leads to a suppression of Λ. In particular, a reduction of T/T_F down to 0.4 reduces Λ by a factor of 2.4(4) compared to the non-degenerate regime. To convince ourselves that the reduction of Λ does not simply result from a reduced absolute temperature, we perform the measurements by varying the temperature T of the sample and the Fermi temperature T_F. This way, we can realize the same T/T_F-conditions at different temperatures and vice versa to decouple effects from the temperature and the Fermi degeneracy. As shown in Figure 4.5b, the data for a given T/T_F follow the inverse-square temperature scaling, while for a given temperature L_3 decreases with increasing T_F for low T/T_F. Thus, we have established a reduction of the three-body loss with respect to the simple $1/T^2$-scaling, which depends on T/T_F.

4.1.3 Suppression mechanisms

A natural explanation for the reduction of Λ according to Eq. (4.15) is to account for the Fermi pressure. The velocity distribution of the fermions is strongly influenced by the Fermi temperature in the degenerate regime and not solely determined by the temperature. This is illustrated in Figure 4.6a, where the collision energy of two Fermi gases is shown where one Fermi gas has a ten times higher Fermi temperature than the other. One can clearly see that the average collisional energy is larger for the degenerate Fermi gas, which according to Equation (4.15) will lead to a reduction of the three-body loss. Thus, the average unitary three-body loss decreases as the Fermi energy increases.

We compare the data with the prediction from the zero-range theory as shown in Figure 4.5. We use the local density approximation, which treats the mixture at each spatial coordinate in the trap as a homogeneous gas with temperature T and fugacity ζ. Accordingly, we can define the temperature independent rate coefficient Λ_f according to the few-body scattering theory as

$$\Lambda_f(T/T_F) = \frac{\int n_{\mathrm{Na}}^2(\boldsymbol{x}) n_{\mathrm{K}}(\boldsymbol{x}) \lambda(\zeta(\boldsymbol{x})) \mathrm{d}^3\boldsymbol{x}}{\int n_{\mathrm{Na}}^2(\boldsymbol{x}) n_{\mathrm{K}}(\boldsymbol{x}) \mathrm{d}^3\boldsymbol{x}}. \tag{4.21}$$

Here, $\zeta(\boldsymbol{x})$ is the fugacity under local density approximation, $\lambda(\zeta) = L_3(\zeta)T^2$ is the local reduced loss coefficient where $L_3(\zeta) = \int l_3(E) f(E) \mathrm{d}E$. The increased collision energy by the Fermi pressure leads to a continuous decrease of Λ_f in the degenerate regime. While the model shows a similar qualitative dependence, the experimental data exhibit a substantially larger reduction: the few-body theory suggests considerable reduction only for $T/T_F \lesssim 0.4$.

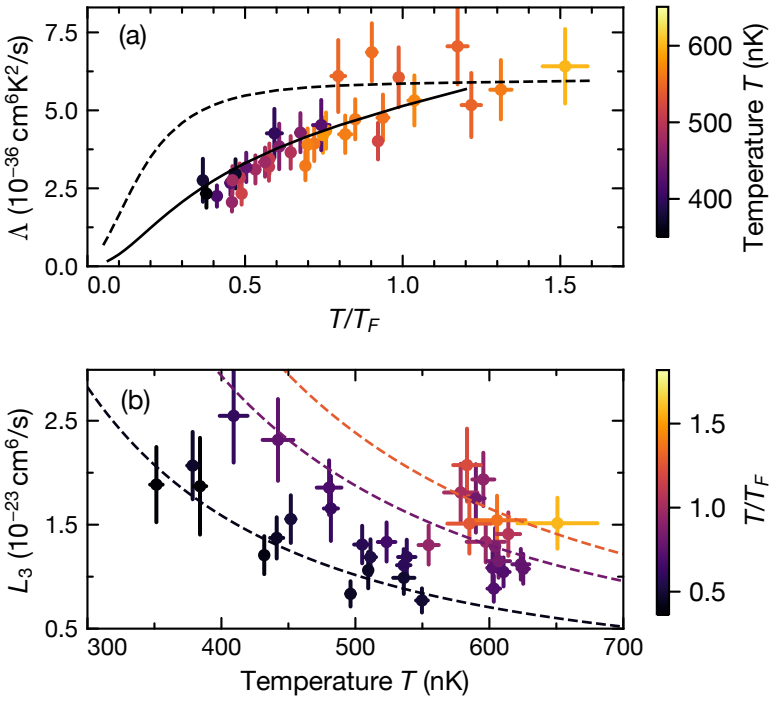

Figure 4.5 – Suppression of unitary three-body loss. (a) Temperature-independent loss coefficient Λ as a function of T/T_F. The color of the data points indicates the temperature of each loss measurement. The dashed line represents the few-body prediction of Λ_f according to Eq. (4.21). The solid line shows the predicted rate coefficient for three-body loss Λ_{RKKY} which includes the RKKY effect in Equation (4.25). (b) Three-body loss coefficient as a function of temperature. The color indicates the reduced temperature T/T_F of the Fermi gas. The dashed lines show the temperature dependence of $L_3 = \Lambda/T^2$ for different T/T_F. The Λ coefficients are obtained by averaging over the data where T/T_F deviates less than 15% from $T/T_F = 0.4$ (black), 0.8 (purple), 1.2 (orange). In this measurement, T is the average temperature for both species. The vertical error bars include the error of the fit of L_3 and a systematic error from the temperature discrepancy between the Na and K clouds. As a result of this temperature mismatch between the K and Na cloud, we estimate a systematic error in Λ of 30%.

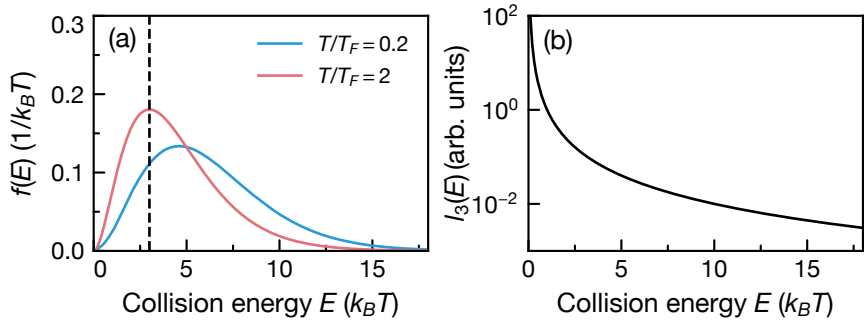

Figure 4.6 – Three-body loss coefficient and collisional energy distribution. (a) The distribution function $f(E)$ for the collisional energy in a Bose–Fermi mixture. We show two scenarios with the same temperature T but different T_F. For a thermal mixture (solid red line), the distribution follows the six-dimensional Boltzmann distribution with an average collision energy of $3k_BT$ (black dashed line). For a mixture with a degenerate Fermi gas (solid blue line), the distribution is shifted towards larger collision energies by the Fermi pressure. (b) Unitary three-body loss coefficient $l_3(E) \propto 1/E^2$, as given by Equation (4.15).

In contrast, the experimental results already show a reduction for $T/T_F \lesssim 1$. Thus, while Fermi pressure does play a significant role in modifying the loss behavior, this effect does not fully explain the suppression. According to the data, the suppression is expected to be more significant at higher T/T_F.

We consider the contribution to the suppression due to many-body effects in this strongly interacting Bose–Fermi mixture. Recently, experiments have observed a modification of the scattering potential of bosons immersed in a Fermi sea [168, 169] and explained this behavior through so-called Ruderman–Kittel–Kasuya–Yosida (RKKY) interactions. These RKKY interactions originate from a coherent three-body scattering process where two bosons obtain an effective long-range interaction by exchanging one fermion. The mediated interaction between two bosons is described by

$$U(R) = -\frac{2m_F g^2 k_F^4}{\hbar^2} \frac{\sin(2k_F R) - 2k_F R\cos(2k_F R)}{(2k_F R)^4}, \tag{4.22}$$

where k_F is the Fermi wavevector and R is the separation between bosons [170, 171]. The interaction strength g is given by the leading order of the contact interaction strength

$$g_0 = \left(\frac{\mu}{2\pi\hbar^2 a} - \frac{2\mu}{(2\pi)^3}\int \mathrm{d}^3\boldsymbol{k}\frac{1}{k^2}\right)^{-1} \tag{4.23}$$

via a regularization procedure [172]. In a degenerate Fermi gas, the momentum integral starts from k_F due to Pauli blocking, which gives

$$g = \left(\frac{\mu}{\hbar^2}\left(\frac{1}{2\pi a} + \frac{k_F}{\pi^2}\right)\right)^{-1}. \tag{4.24}$$

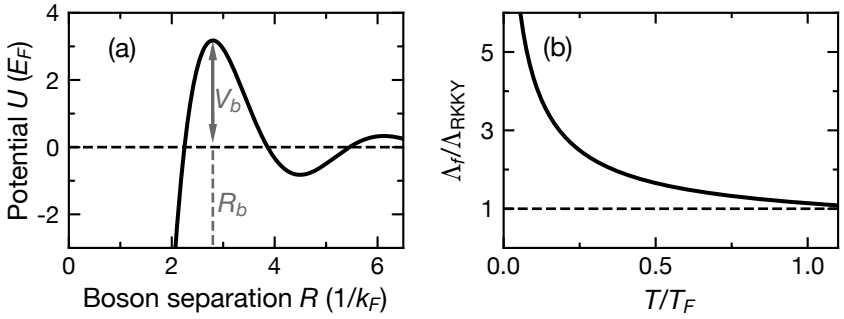

Figure 4.7 – The effect of the RKKY interactions. (a) RKKY potential mediated by fermions between two bosons at unitarity. The potential barrier V_b suppresses the tunneling probability into short range. (b) The suppression factor from the RKKY interactions $\Lambda_f/\Lambda_{\mathrm{RKKY}}$ as a function of T/T_F.

At unitarity where $1/a = 0$, we obtain $g = \frac{\pi^2\hbar^2}{\mu k_F}$, which gives $V_b \approx 3.2\frac{\hbar^2 k_F^2}{2m_F}$ for the mass ratio in our system.

As shown in Figure 4.7a, the RKKY interaction is attractive at short distance and is oscillatory with a length scale π/k_F at long range. At a distance $R_b = 2.8/k_F$, the oscillation gives rise to a barrier of the height $V_b \approx 3.2\,E_F \propto T_F$. When the average distance between bosons is much shorter than R_b, only the short-range attractive interaction plays a role [168, 169]. In our experiment, the bosons are still thermal with an average distance $\gtrsim 0.6\,\mu\mathrm{m}$ larger than $R_b \approx 0.3\,\mu\mathrm{m}$. Therefore, the potential acts in our favor and reduces the probability of two bosons approaching each other. In the low-temperature regime, the tunneling probability through the potential barrier P_T is given by the Bethe–Wigner threshold law $\sqrt{E/V_b} \propto \sqrt{T/T_F}$ [173], which gives rise to the additional suppression in the degenerate regime. Again, we apply the local density approximation to obtain the local tunneling probability $P_T(\zeta(\boldsymbol{x})) = \sqrt{3k_BT/2V_b(\zeta(\boldsymbol{x}))}$ from the potential barrier $V_b(\zeta(\boldsymbol{x}))$ and the average kinetic energy of the bosons $(3/2)k_BT$. Accordingly, we define the rate coefficient from three-body loss, including the RKKY-interaction Λ_{RKKY} as

$$\Lambda_{\mathrm{RKKY}}(T/T_F) = \frac{\int n_{\mathrm{Na}}^2(\boldsymbol{x}) n_{\mathrm{K}}(\boldsymbol{x}) \lambda(\zeta(\boldsymbol{x})) P_T(\zeta(\boldsymbol{x})) \mathrm{d}^3\boldsymbol{x}}{\int n_{\mathrm{Na}}^2(\boldsymbol{x}) n_{\mathrm{K}}(\boldsymbol{x}) \mathrm{d}^3\boldsymbol{x}}. \tag{4.25}$$

Equation (4.25) reproduces the experimental data in the Fermi-degenerate regime without any fitting parameters, as shown in Figure 4.5a. In the deeply degenerate regime, the model predicts more than one order of magnitude reduction such that $\Lambda_{\mathrm{RKKY}}(T/T_F < 0.13) < 0.1\Lambda_{th}$ where Λ_{th} is the reduced loss coefficient in a non-degenerate thermal mixture. The suppression from the RKKY effect can be quantified by $\Lambda_f/\Lambda_{\mathrm{RKKY}}$. As shown in Figure 4.7b, the suppression factor increases with the Fermi degeneracy. At $T/T_F = 0.13$ where we predict a reduction of Λ by one order of magnitude compared to Λ_{th}, the few-body theory predicts a reduction by a factor of 2.6, and the RKKY effect suppresses the loss further by a factor of $\Lambda_f/\Lambda_{\mathrm{RKKY}} \simeq 3.7$. As T/T_F increases, the form of the mediated interaction breaks

down due to thermal fluctuations. Therefore we expect a crossover from the prediction with the mediated interactions in the Fermi-degenerate regime to the constant loss in the thermal regime.

4.2 Atom-dimer loss

Once molecules accumulate in the trap during the association process, the inelastic collisions between the molecules and the residual atoms lead to the depletion of the molecules. We characterize the collisions between the Feshbach molecules with Na atoms and K atoms, respectively. In contrast to the three-body loss presented in the previous section, where the Na-K-K collisions are suppressed by Pauli blocking, this assumption cannot be made for the atom-dimer loss since the collisions occur between distinguishable fermions.

The experiment starts with an atomic Bose–Fermi mixture in an optical dipole trap at a temperature of 250 nK. We ramp the magnetic field across the Feshbach resonance at a rate of 3.5 G/ms to produce Feshbach molecules. Afterward, we remove the unwanted atoms with a resonant light pulse on the D-lines of the respective species after we ramp the magnetic field to 50 G. At this magnetic field, the bound state is detuned from the atomic state by $\Delta = E_b \approx 2\pi \times 60\,\mathrm{MHz}$. While the Feshbach molecules are unaffected by removing the K atoms, the removal of the Na atoms leads to the loss and heating of the Feshbach molecules because the Na atoms inside the Feshbach molecules absorb some of the Na light. This is because the Na atoms have a larger natural linewidth ($\Gamma \approx 2\pi \times 10.0\,\mathrm{MHz}$ [116]) than the K atoms ($\Gamma \approx 2\pi \times 6.0\,\mathrm{MHz}$ [117]) on the transition we use for the atom removal. We mitigate the problem by transferring the residual Na atoms with a radio-frequency pulse from $|F, m_F\rangle = |1,1\rangle$ to $|2,2\rangle$ before applying the resonant clearout pulse.

For the K-NaK atom-dimer loss measurement, we typically start with 6×10^4 K atoms and 1.5×10^4 Feshbach molecules. The number of molecules is intentionally reduced to mitigate the effect of dimer-dimer collisions. In a similar spirit, in the measurements involving Na atoms colliding with Feshbach molecules, we typically start with 5×10^4 Na atoms and 1.5×10^4 Feshbach molecules. After the removal of residual atoms, we ramp the magnetic field to 75.5 G and hold the sample for 1 ms before ramping the magnetic field to the target value within 1.5 ms, where we hold the sample for a variable time. The remaining atoms and molecules are detected after time-of-flight expansion in the presence of a magnetic field gradient. Before imaging, the molecules are dissociated by ramping the magnetic field back across the Feshbach resonance. The rate coefficient between the atomic species $i = \mathrm{K}, \mathrm{Na}$ and molecules $\beta_{\mathrm{i+NaK^*}}$ are extracted by the following set of differential equations differential equation:

$$\frac{\mathrm{d}N_{\mathrm{NaK^*}}}{\mathrm{d}t} = -\beta_{i+\mathrm{NaK^*}} \int n_i(\boldsymbol{x}) n_{\mathrm{NaK^*}}(\boldsymbol{x}) \mathrm{d}^3\boldsymbol{x} - \beta_{\mathrm{NaK^*+NaK^*}} \int n^2_{\mathrm{NaK^*}}(\boldsymbol{x}) \mathrm{d}^3\boldsymbol{x} \tag{4.26}$$

$$\frac{\mathrm{d}N_i}{\mathrm{d}t} = -\beta_{i+\mathrm{NaK^*}} \int n_i(\boldsymbol{x}) n_{\mathrm{NaK^*}}(\boldsymbol{x}) \mathrm{d}^3\boldsymbol{x}, \tag{4.27}$$

respectively. We do not include a change in the temperature in the model as no significant

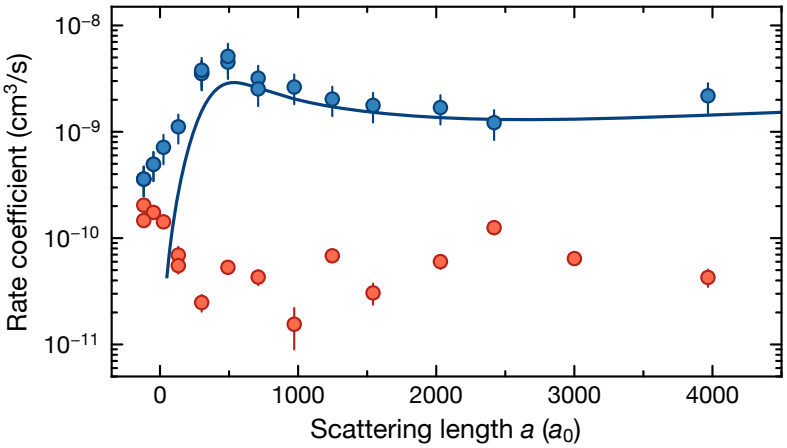

Figure 4.8 – Rate coefficients for Na-NaK* (blue) and K-NaK* (red) atom-dimer loss shown as a function of the scattering length. The solid line shows a fit of the Na-NaK* dimer loss to the zero-range theory with the inelasticity parameter $\eta = 0.1$ and the three-body parameter $R_0 = 200a_0$ [174].

heating is observed throughout the measurements. The density is extracted according to Equation (2.31) using the respective numbers, temperatures and trapping frequencies for the atoms and the Feshbach molecules. Since, at the time of the measurement, we did not have any knowledge about the dimer-dimer collisions, both $\beta_{i+\mathrm{NaK}^*}$ and $\beta_{\mathrm{NaK}^*+\mathrm{NaK}^*}$ were used as fitting parameters.

As shown in Figure 4.8, the dominating loss between Feshbach molecules results from the inelastic collisions between the molecules and Na atoms. For most scattering lengths, $\beta_{\mathrm{Na}+\mathrm{NaK}^*}$ is at least an order of magnitude larger than $\beta_{\mathrm{K}+\mathrm{NaK}^*}$. The rate-coefficient of the two atom-dimer loss processes becomes comparable only close to the zero crossing of the interspecies scattering length. The rate coefficient $\beta_{\mathrm{Na}+\mathrm{NaK}^*}$ is strongly influenced by the Efimov resonance at $a \approx 500\,a_0$ from which we determined the inelasticity parameter $\eta = 0.1$ and three-body parameter $R_0 = 200\,a_0$ using the zero-range theory with temperature averaging [152, 174]. Note, however, that the Efimov resonance belongs to a different Efimov state than the resonance determined from the three-body loss. The difference between the R_0 extracted from three-body and atom-dimer loss is within a factor of 6, which is negligible compared to the ratio between the scattering lengths of neighboring Efimov resonances, given by the Efimov scaling factor ($e^{\pi/s_0} \simeq 6 \times 10^4$). The difference between R_0 on the different sides of the Feshbach resonance could be explained by the formalism in [175].

The rate coefficient $\beta_{\mathrm{K}+\mathrm{NaK}^*}$ reasonably agrees with the naive expectation that the loss is suppressed around the resonance and increases as the Feshbach molecules become more deeply bound. The increase of the $\beta_{\mathrm{K}+\mathrm{NaK}^*}$ close to the resonance contradicts this explanation. Note that in the regime $a < 1000\,a_0$, the atom-dimer loss is the dominant loss process and the extracted $\beta_{\mathrm{K}+\mathrm{NaK}^*}$ is more trustworthy than for the measurement for $a > 1000\,a_0$ where dimer-dimer loss is the dominant loss process. In addition, close to resonance, the

measured loss coefficient might be influenced by thermal dissociation associated with additional loss processes.

4.3 Tunable p-wave collisions in fermionic Feshbach molecules

Feshbach molecules are in highly excited vibrational states close to the dissociation threshold. Nowadays, they mainly represent an intermediate product in the association of ground-state molecules. However, Feshbach molecules are interesting as they exhibit a rich collisional behavior near the Feshbach resonance. In contrast to collisions between bosons or distinguishable fermions, the dominant collisional channel of our fermionic NaK* Feshbach molecules is p-wave, leading to tunable inelastic and elastic collisions. This chapter describes the systematic investigation of p-wave collisions of Feshbach molecules.

4.3.1 Tunable Feshbach molecules: A tale of two regimes

Feshbach molecules feature tunable interactions in the vicinity of the Feshbach resonance by changing the admixture of the molecular bound state. Sufficiently close to the resonance, where coupling between the open channel and the closed channel is large, the properties of Feshbach molecules are universal with the interatomic scattering length a. The binding energy is given by $E_b = -\hbar^2/(2\mu a^2)$ where μ is the reduced mass of the atom pair, and the bond length of the molecules is given by $\langle r \rangle = a/2$. The universality results from the fact that the wavefunction of the molecules mostly lives outside the interatomic van der Waals potential such that the details of the potential do not influence the properties of the molecules. Such molecules are typically called halo dimers as the size of the molecules is larger than one would classically expect from the potential and the binding energy of the molecules. The classical turning point is typically given by $r_{\text{classical}} = ((2a_{\text{vdW}})^2 a)^{1/3}$. Here, a_{vdW} is the van der Waals length which characterizes the typical size related to the van der Waals potential. An example of the wavefunction of a helium halo dimer is shown in Figure 4.9. In contrast, the behavior of deeply bound Feshbach molecules is predominantly determined by the van der Waals potential and insensitive to changes in the scattering length, and the binding energy changes linearly with the magnetic field. We refer to this regime as the non-halo regime, where the molecular wavefunction is confined within the van der Waals potential. The size of the molecules is given by $\bar{a} = 2\pi \left(2\mu C_6/\hbar^2\right)^{1/4}/\Gamma(\frac{1}{4})^2 = 0.956\, a_{\text{vdW}}$ where $\bar{a}$ is the average scattering length, C_6 the van der Waals coefficient and $\Gamma(x)$ the gamma function [12, 176].

4.3.2 Inelastic p-wave collisions

When associating the degenerate Feshbach molecules presented in Section 5.4, we were surprised about the second-long lifetimes of the sample. On the one hand, we expected the fermionic Feshbach molecules to be long-lived as Pauli-blocking protects them from

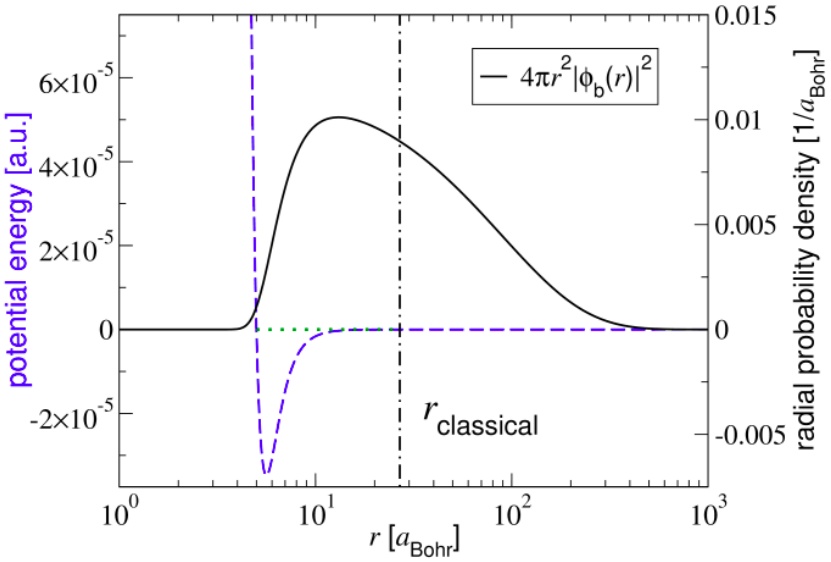

Figure 4.9 – Helium dimer interaction potential and (dashed curve) and the radial probability density of a Helium dimer (solid curve). The vertical dashed line shows $r_{\text{classical}}$ which marks the classical turning point related to the van der Waals potential. For $r > r_{\text{classical}}$, the binding energy is smaller than the potential energy and the wavefunction takes the form of an exponential decay. This figure was adapted from Ref. [176].

reaching short range. On the other hand, previous experiments have reported lifetimes of hundred milliseconds [177, 178] or even as short as a millisecond [179]. Moreover, it struck us that the lifetime of the Feshbach molecules was longer than that of the NaK molecules in the ground state, which did not fit into the naive understanding that molecules in highly vibrational states are expected to be short-lived compared to molecules in the rovibronic ground state. Intending to reduce collisional loss after the magnetoassociation and driven by the interest in understanding the collisional behavior of the Feshbach molecules, we started to investigate the inelastic collisions.

We characterize the inelastic collisions of NaK* Feshbach molecules in a crossed optical dipole trap as a function of the scattering length a and the temperature of the molecular sample T. The association of the molecules starts with a mixture of bosonic ^{23}Na and fermionic ^{40}K atoms in their respective energetically lowest hyperfine states $|F,m_F\rangle = |1,1\rangle$ and $|9/2,-9/2\rangle$. We ramp the magnetic field across the interspecies Feshbach resonance at 78.3 G. After the association, we purify the molecular sample by quickly ramping the magnetic field to 72.3 G where we remove residual atoms from the trap by applying a magnetic-field gradient of 40 G/cm. As the Feshbach molecules have a vanishing magnetic moment at this magnetic field, they are unaffected by the magnetic-field gradient. This procedure allows us to produce around 3×10^4 Feshbach molecules at a temperature of 500 nK in the 1550/1064-nm optical dipole trap with trapping frequencies $(\omega_x, \omega_y, \omega_z) = 2\pi \times (57, 91, 246)$ Hz at an effective trap depth of $U = k_B \times 6\,\mu$K. We adiabatically change the trap confinement by compression or decompression to change the temperature. This allows

us to investigate the collisional loss for temperatures ranging from 300 nK to 1000 nK. We ensure that the temperature in all spatial directions is the same by performing the compression or decompression such that the ratios of the trapping frequencies remain the same as we change the trap confinement. After adjusting the trap parameters we ramp the magnetic field within 15 ms from 72.3 G to 75.5 G. After a short hold time, we use a ramp with a duration of 1.5 ms to change the magnetic field from 75.5 G to the target magnetic field B corresponding to the scattering length a according to Equation (3.27). This ramping sequence has been implemented to reduce the effects of eddy currents, especially for the measurements close to resonance, where small magnetic field deviations result in a significant change in the scattering length. After the magnetic field B has been reached, we hold the molecules for a variable time, after which we turn off all the dipole traps, ramp the magnetic field to 72.3 G and turn on a magnetic-field gradient of 40 G/cm. After time of flight, during which the density of the molecular sample has reduced, we ramp the magnetic field back through the Feshbach resonance to dissociate the molecules with negligible loss. Finally, we detect the Feshbach molecules with absorption imaging.

The two-body inelastic collisions Feshbach molecules can be described by:

$$\frac{\mathrm{d}n}{\mathrm{d}t} = -\beta_{\mathrm{inel}} n^2 \,, \tag{4.28}$$

where β_{inel} the rate coefficient of inelastic collisions and n is the average density of the molecular sample. We obtain the rate coefficient of inelastic collisions by measuring the number of molecules over time. The molecule density in a harmonic trap follows a Gaussian distribution. Given a geometric-mean trap frequency $\bar{\omega} = (\omega_x \omega_y \omega_z)^{1/3}$ and temperature T, the average density of molecules n can related to the number of molecules N with mass m by

$$n = \left(\frac{m\bar{\omega}^2}{2\pi k_B T} \right)^{3/2} N \,, \tag{4.29}$$

thus we can rewrite Equation (4.28) in terms of the change in the number of molecules as

$$\frac{\mathrm{d}N}{\mathrm{dt}} = -\beta_{\mathrm{inel}} n N \,. \tag{4.30}$$

We observe that the heating during the measurement is insignificant in comparison to the statistical error of the temperature. We thus omit heating in the model and rewrite Equation (4.30) in terms of the number of molecules

$$\frac{\mathrm{d}N}{\mathrm{dt}} = -\beta_{\mathrm{inel}} \left(\frac{m\bar{\omega}^2}{2\pi k_B \bar{T}} \right)^{3/2} N^2 \,, \tag{4.31}$$

where $\bar{T}$ represents the average temperature during the hold time.

In p-wave dominated collisions between fermions, the centrifugal p-wave barrier reduces the probability of the molecules reaching the short-range regime and undergoing loss. The rate of inelastic collisions is determined by the probability of the molecules to tunnel through

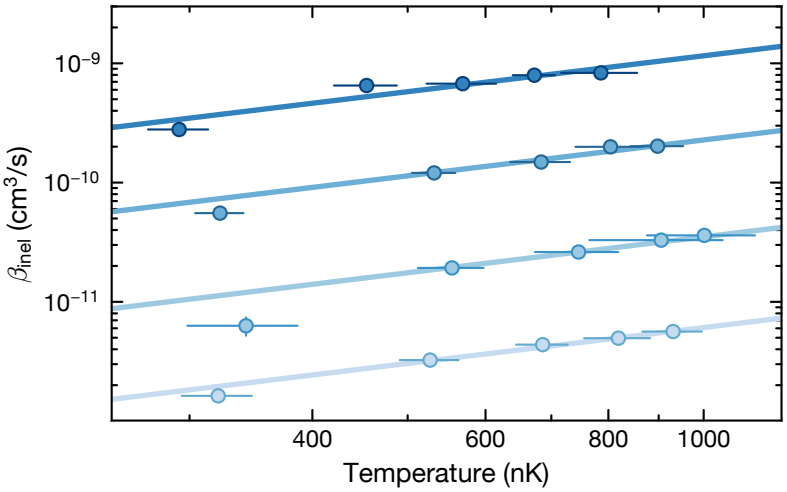

Figure 4.10 – Temperature dependence of collisional loss coefficient β_{inel} at $a = -14\,a_0$, $554\,a_0$, $1542\,a_0$, $3000\,a_0$ (from bright to dark blue). The loss coefficient obtained from the respective data sets are fitted with a linear fit (solid lines). The error in β_{inel} is given by the error of the fit. The horizontal error bars represent the statistical error of the temperature in the measurement. A systematic error of 30% in β_{inel} is expected from a 10% error in the trapping frequency.

the barrier resulting in an inelastic collision. For kinetic energies considerably smaller than the p-wave barrier, the inelastic collisions are expected to scale as $\beta_{\text{inel}} = K_{\text{inel}} T$. This linear dependence of the rate coefficient on the temperature has previously been observed for fermionic ground-state molecules [137, 180]. We check whether it also applies to Feshbach molecules. The results are summarized in Figure 4.10 showing the rate coefficient of inelastic collisions for different temperatures at four different scattering lengths ranging from the non-halo regime ($a = -14\,a_0$) to the halo regime ($3000\,a_0$). We fit the data with a linear function where the slope is the only fit parameter, and the y-intercept is forced to zero. The loss coefficient is well described with a linear temperature scaling for all measured scattering lengths.

Next, we investigate the collisional loss as a function of the interspecies scattering length a. The results are summarized in Figure 4.11a. Since each realization of the measurement was performed at a slightly different temperature, we make use of the linear temperature scaling and present the rate coefficients at a temperature of 500 nK. One can see that close to the resonance, the loss is strongest when the molecules are in the halo regime. We note however that the measured rate coefficients below the unitarity limit $\beta_{\text{unitary}} = 2\hbar\lambda_{dB}/\mu_m$, where λ_{dB} is the de Broglie wavelength and $\mu_m = m_{\text{NaK}}/2$ is the reduced mass between two molecules. At a temperature 500 nK the unitary rate coefficient is given by $\beta_{\text{inel}} = 1.77 \times 10^{-9}\,\text{cm}^3/\text{s}$. As we increase the binding energy, the rate coefficient of inelastic collisions β_{inel} changes by three orders of magnitude before it reaches a value of $\beta_{\text{inel}} = 3.3(1) \times 10^{-12}\,\text{cm}^3/\text{s}$ deep in the non-halo regime.

For the halo regime we compare our data with calculations presented in Ref. [64] predict-

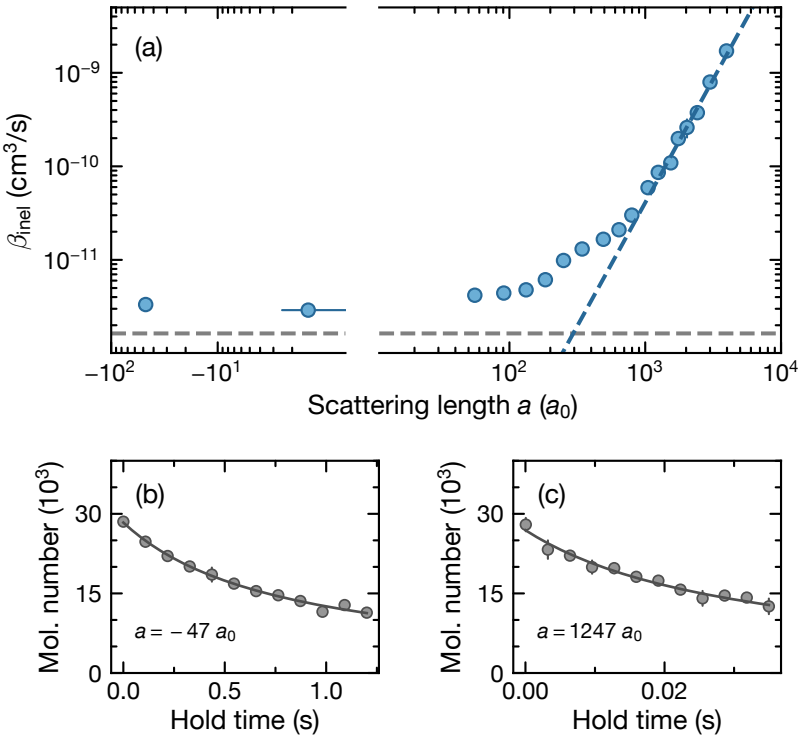

Figure 4.11 – Two-body loss coefficient β_{inel} as a function of the scattering length a for $T = 500\,\mathrm{nK}$. (a) Deep in the non-halo regime the loss approaches $\beta_{\mathrm{inel}} = 3.3(1) \times 10^{-12}\,\mathrm{cm}^3/\mathrm{s}$. The gray dashed line gives the loss coefficient of $\beta_{\mathrm{inel}} = 1.65 \times 10^{-12}\,\mathrm{cm}^3/\mathrm{s}$ predicted by MQDT calculations. For $a > 1000\,a_0$, β_{inel} is fitted with $\beta_{\mathrm{inel}}(a) = ca^l$ which yields $l = 2.58(14)$ (blue dashed line). The error in β_{inel} is given by the error of the fit. The horizontal error bars result from a 15-mG uncertainty in the magnetic field. A systematic error of 30% in β_{inel} is expected from a 10% error in the trapping frequency. (b),(c) The number of Feshbach molecules as a function of the hold time for $B = 72\,\mathrm{G}$ ($a = -47\,a_0$) and $B = 77.8\,\mathrm{G}$ ($a = 1300\,a_0$). The solid line shows the fitted molecule number from the from the two-body loss model described by Equation (4.31) assuming a constant temperature.

ing that $\beta_{\text{inel}} \propto a^3$. In these calculations, the authors assume that the dimers are composed of atoms with large mass imbalance and that the fermionic atom is the lighter atom. Hence, the motion of the light fermions can be integrated out in a Born-Oppenheimer approximation. While these assumptions are not fulfilled in our system, we check the predicted scaling by fitting the two-body loss coefficient with a polynomial of the form $\beta_{\text{inel}}(a) = ca^l$ for scattering lengths deep in the halo regime, $a > 1000\,a_0$, and obtain $l = 2.58(14)$.

In the non-halo regime, we compare our data with predictions from multichannel quantum defect theory (MQDT) which have previously reproduced the loss coefficient for molecules in rovibronic ground states [137, 181] and in high-lying vibrational states [182]. The predicted two-body loss coefficient in collisions of indistinguishable fermions [66] is given by

$$\beta_{\text{inel}}(T) = \frac{\Gamma(1/4)^6}{\Gamma(3/4)^2}\bar{a}^3\frac{k_B T}{h} = 1513\bar{a}^3\frac{k_B T}{h}. \tag{4.32}$$

We calculate the van der Waals coefficient of NaK* Feshbach molecules by approximating the long-range interaction to be the sum of the contribution from individual atoms, i.e., $C_{6,\text{FB}} = C_{6,\text{Na}} + C_{6,\text{K}} + 2C_{6,\text{Na-K}} = 10543$ where $C_{6,\text{Na}} = 1556$, $C_{6,\text{K}} = 3897$ [183] and $C_{6,\text{Na-K}} = 2454$ [184] in atomic units. We thus obtain $\bar{a} = 88.8\,a_0$. At a temperature of 500 nK, Equation (4.32) yields $1.65 \times 10^{-12}\,\text{cm}^3/\text{s}$, which is a factor two lower than our measured value in the non-halo regime.

We are not sure where the discrepancy between the data might be coming from. However, I would like to remark that the value of the MQDT calculation gives the *universal* loss rate where the probability of an inelastic collision once the molecules have tunneled through the centrifugal barrier is equal to unity. Thus, apart from systematic errors in the measurements, the discrepancy could be explained by the fact that the collisions between NaK* Feshbach molecules are not universal. However, also other systems that expect universal loss have observed a similar discrepancy from the MQDT calculations [137, 181].

In the measurement, we observe a small loss enhancement at around $a = 200\,a_0$. Such an increase in the rate coefficient could be attributed to a resonance with an Efimov trimer state. Since we do not have a model that describes the behavior between the halo and the non-halo regime, we cannot be sure whether this enhancement can be attributed to an Efimov resonance and do not undertake any further attempts to clarify this.

Let us address the collision process of the molecules once they reach the short-range regime. Works such as the ones in Ref. [185, 186] attribute their collisional loss to *vibrational relaxation*, where two molecules collide and the collisional energy suffices to transfer one dimer into a lower lying vibrational state while the other dimer gains sufficient energy to dissociate. Since the vibrational spacing is on the order of $\Delta E \sim \hbar \times 1\,\text{THz}$, the products of a collision with vibrational relaxation in the short range will have enough kinetic energy to leave the trap. However, we see that depending on the binding energy of the Feshbach molecules, the dimer-dimer collisions lead to the accumulation of K atoms in the trap. Our data suggest that the underlying loss process of two NaK Feshbach molecules colliding in the short range results in *three-body recombination*. In this process, two Na atoms and one K atom form a short-lived trimer. The remaining K atom acts as a spectator in this collision and takes away the binding energy of the Feshbach molecule $E_b = \hbar^2/(2\mu a^2)$. The break-up

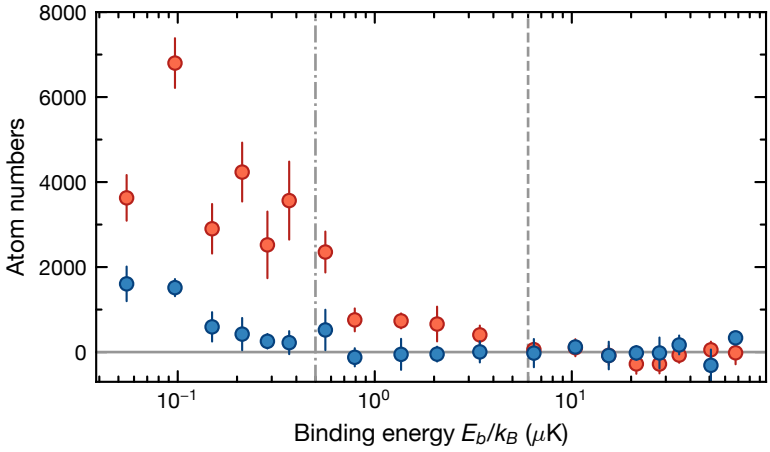

Figure 4.12 – Three-body recombination and thermal dissociation. Number of accumulated Na atoms (blue) and K atoms (red) during the loss measurements at various scattering lengths a. In each measurement, we prepare the system under the same conditions and average over the number of Na or K atoms for the respective last four holding times to obtain the numbers shown. The error bar indicates the standard deviation. The dashed line indicates $E_b = U$, where $U = k_B \times 6\,\mu\text{K}$ is the effective trap depth in the measurement. The dash-dotted line indicates $E_b = k_B T$ where $T = 500\,\text{nK}$ is the temperature of the molecular sample in the measurement.

of the Na-Na-K trimer releases the binding energy on the order of $E_b = \hbar^2/(2\mu a_{\text{vdW}}^2)$ which corresponds to temperatures on the order of hundred millikelvins which is larger than the typical trap depth. Therefore, one can assume that the Na-Na-K products will immediately leave the dipole trap. In Figure 4.12 we show the number of accumulated K atoms and Na atoms as a function of the binding energy. We can identify three regions in this plot. Na and K atoms do not accumulate in the trap for binding energies much larger than the trap depth. However, once the binding energy becomes comparable to the trap depth, the K atoms start to accumulate in the trap, and as the binding energy decreases, the number of accumulated K atoms slightly grows. In the regime where the temperature becomes comparable to the binding energy, the thermal energy is sufficient for the molecules to break apart. This process is called *thermal dissociation*.

As shown in Figure 4.8, the rate coefficient of collisions between Feshbach molecules and K atoms is more than an order of magnitude smaller than the measured dimer-dimer rate coefficient. Considering that the number of K atoms is an order of magnitude smaller than the density of Feshbach molecules, we can conclude that the K-NaK* atom-dimer loss is negligible. The regime of thermal dissociation is more critical. First, Feshbach molecules can spontaneously dissociate into atoms. In addition, since the Na-NaK* dimer loss is comparable to the measured value, the effect of Na-NaK* loss cannot be neglected. Given the order of magnitude smaller density of Na atoms and the comparable atom-dimer and dimer-dimer rate coefficients in the dissociation regime, we estimate that around 20% of the measured rate coefficient can be attributed to the thermal dissociation and Na-NaK* loss.

To our initial surprise, the rate coefficient of NaK* Feshbach molecules in the non-halo

regime is 20 times lower than that of the ground-state NaK molecules [137][1]. Since the rate coefficient for two-body loss in both those systems can be described by the MQDT calculations in Idziaszek *et al.* [66], it is only a question of the average scattering length $\bar{a} \propto C_6^{1/4}$. In essence, while the electronic contribution to the C_6 coefficient is similar for Feshbach and ground-state molecules, ground-state molecules possess a molecular-frame dipole moment which increases $\bar{a}$. For ground-state molecules, $C_{6,\mathrm{GS}} = C_{\mathrm{el,GS}} + C_{\mathrm{rot,GS}}$, where the first term is the contribution from the electronic wavefunction of the molecules and the second term is the contribution from the rotational dipole part [188]. The second term typically dominates and scales as d^4. This also means that molecules with lower dipole moment are expected to have a lower rate coefficient of inelastic collisions if universal loss applies.

4.3.3 Elastic p-wave collisions

Despite the favorable scaling of the elastic-to-inelastic collisions with $\beta_{\mathrm{el}}/\beta_{\mathrm{inel}} \propto a^3 T^{3/2}$ [64], no observation of elastic collisions in fermionic Feshbach molecules has been reported. This is probably due to disappointingly short lifetimes reported for fermionic Feshbach molecules and the prospect of more promising platforms such as ground-state molecules.

We study the elastic collisions of Feshbach molecules by observing cross-dimensional thermalization of an out-of-equilibrium molecular sample. In contrast to the previous sequence for inelastic collisions, the association of Feshbach molecules takes place in the 785-nm species dependent dipole trap. After molecule association we transfer them from the 785-nm trap into the 1550/1064-nm trap which typically results in 1×10^4 Feshbach molecules. For the measurement of the scattering-length dependence of p-wave collisions, we compress the dipole trap to obtain the trapping frequencies trapping frequencies $(\omega_x, \omega_y, \omega_z) = 2\pi \times (72, 163, 397)\,\mathrm{Hz}$, an effective trap depth of $U = k_B \times 8\,\mu\mathrm{K}$ and an initial temperature of $T_x = 350\,\mathrm{nK}$ and $T_z = T_y = 550\,\mathrm{nK}$. For the temperature dependence, we change the compression of the trap to vary the average temperature between $T_{\mathrm{avg}} = (2T_z + T_x)/3 = 300\,\mathrm{nK}$ and 1000 nK.

We obtain the elastic and inelastic collision coefficients from the following set of differential equations

$$\frac{\mathrm{d}n}{\mathrm{d}t} = -\frac{n^2}{3} K_{\mathrm{inel}} (2T_z + T_x) - \frac{n}{2T_x}\frac{\mathrm{d}T_x}{\mathrm{d}t} - \frac{n}{2T_z}\frac{\mathrm{d}T_z}{\mathrm{d}t}, \tag{4.33}$$

$$\frac{\mathrm{d}T_z}{\mathrm{d}t} = \frac{n}{12} K_{\mathrm{inel}} T_z T_x - \frac{\Gamma_{th}}{3}(T_z - T_x) + c_l, \tag{4.34}$$

$$\frac{\mathrm{d}T_x}{\mathrm{d}t} = \frac{n}{12} K_{\mathrm{inel}} (2T_z - T_x) T_x + \frac{2\Gamma_{th}}{3}(T_z - T_x) + c_l, \tag{4.35}$$

which we adopt from a model used for two-body collisions in polar molecules [180]. Here, n is the average density of the sample and $K_{\mathrm{inel}} = \beta_{\mathrm{inel}}/T$ is the temperature-independent coef-

[1] While the discussion of the loss process of ground-state molecules is mentioned only briefly in this thesis, this is currently a hot topic in the field. Our team has invested considerable time into understanding the loss process in NaK ground state molecules. Roman Bause has covered this in his Ph.D. thesis [187].

ficient of inelastic collisions. T_x and T_z are the effective temperatures of the molecules in the horizontal and vertical directions, respectively. We checked that the temperature along the direction of the imaging beam T_y is equal to T_z and assume this for all measurements. Γ_{th} is the thermalization rate given by $\Gamma_{th} = n\sigma\bar{v}/\alpha$ where σ is the cross-section of the elastic collisions which is assumed to be constant for each measurement, $\bar{v} = \sqrt{16k_B(2T_z + T_x)/(3\pi m)}$ is the average velocity of molecules and $\alpha = 4.1$ is the number of collisions needed for thermalization in p-wave collisions [5, 180]. The linear heating term c_l is introduced to phenomenologically account for isotropic heating that we observe in these measurements, but were absent in the measurements presented in the previous section. We believe that the linear heating results from the damping of collective oscillation of the cloud inside the dipole trap due to the compression. Since the heating shows a scattering length dependence, the timescale of the damping might be determined by the rate of elastic collisions. We numerically fit Eqs. (4.33)–(4.35) in the basis of the average temperature $T_{\text{avg}} = (2T_z + T_x)/3$ and the difference in temperature $\Delta T = T_z - T_x$ to reduce the common mode fluctuation in the temperatures.

The resulting coefficients of inelastic and elastic collisions, β_{inel} and $\beta_{\text{el}} = \sigma\bar{v}$, are summarized in Figure 4.13a as a function of the scattering length for a temperature of 500 nK. Since the various measurements are taken at slightly different temperatures, we scale $\bar{v}$ according to the temperature while the elastic cross-section σ is not being scaled.

Deep in the non-halo regime, collisions of Feshbach molecules predominantly result in loss such that the number of elastic collisions during the lifetime of the molecular sample is negligible. As a result, cross-dimensional thermalization is absent (see Figure 4.13b), and we only observe linear heating. The elastic collision rate increases notably faster for higher scattering lengths than the inelastic collision rate. The molecular cloud exhibits cross-dimensional thermalization, and the temperatures in the two directions approach each other during the measurement (see Figure 4.13c).

Unfortunately, our measurement does not allow us to extract the scaling of β_{el} with the scattering length a in the halo regime for the following reasons: First, while we intentionally reduced the initial molecule density to $n_0 = 0.4 \times 10^{11}\,\text{cm}^{-3}$, the elastic collision rate becomes comparable to the trap frequencies for a scattering length of $a > 2000\,a_0$. Therefore the system enters the hydrodynamic regime and the measured value of β_{el} saturates near the so-called hydrodynamic limit given by $\bar{\omega}\alpha/(2\pi n_0) = 1.71 \times 10^{-9}\,\text{cm}^3/\text{s}$ with a geometric mean trapping frequency $\bar{\omega} = 2\pi \times 167\,\text{Hz}$ [189]. We note that the measured elastic collision rate can exceed the hydrodynamic limit calculated for a constant density in the presence of strong loss as the density significantly reduces during the loss measurement. Our model, which only considers dimer-dimer elastic collisions, is only valid in deducing β_{el} for scattering lengths up to $610\,a_0$. When $a > 610\,a_0$, where the binding energy of the molecules is smaller than the trap depth, we observe an accumulation of spectator K atoms which can contribute to the cross-thermalization. Despite these limitations, this measurement shows that the rate coefficient of elastic collisions exhibits a stronger scaling with the scattering length than that of inelastic collisions.

In addition, we measure the scaling of the elastic collision rate with the temperature. To this end, we perform a compression to different trap depths that is cross-dimensionally non-

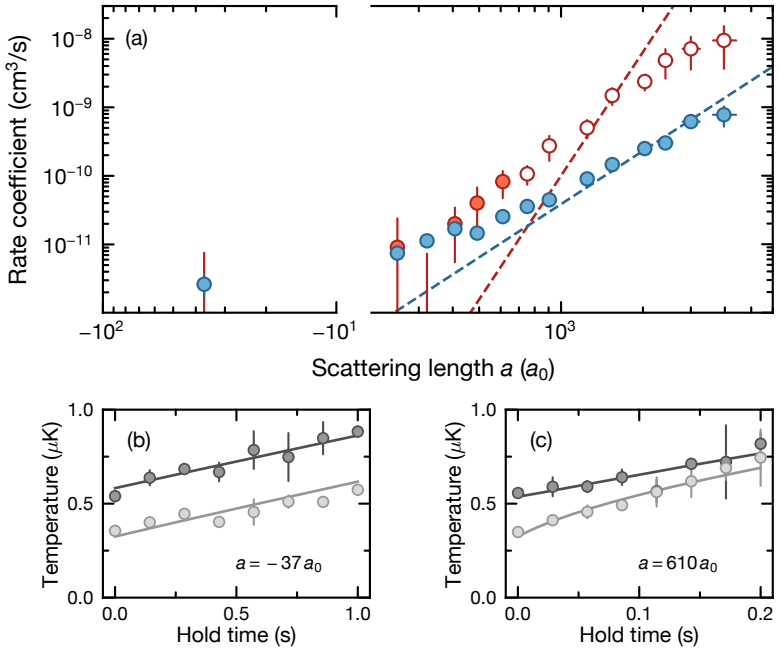

Figure 4.13 – Elastic p-wave collisions of fermionic Feshbach molecules. (a) Elastic collision coefficient β_{el} (red) and inelastic collision coefficient β_{inel} (blue) as a function of the scattering length a for a temperature $T = 500\,\mathrm{nK}$. Data points for β_{el} are marked (open symbols) when the number of K atoms increases during the measurement. The solid red line marks the onset of the hydrodynamic regime (see main text). The red dashed line shows an a^6 scaling and serves as a guide to the eye. The error of the fit gives the vertical error bars for the inelastic and elastic collision rates. The horizontal error bars result from a 15-mG uncertainty in the magnetic field. A systematic error of 30% in the collision rate coefficients is expected from a 10% error in the trapping frequency. The rate coefficient for elastic collisions for $a = -37\,a_0, 322\,a_0$ lie outside of the plotting range. (b), (c) Effective temperatures T_z (dark gray) and T_x (light gray) as a function of the hold time for magnetic fields of 72.25 G ($-37\,a_0$) 77.25 G ($610\,a_0$).

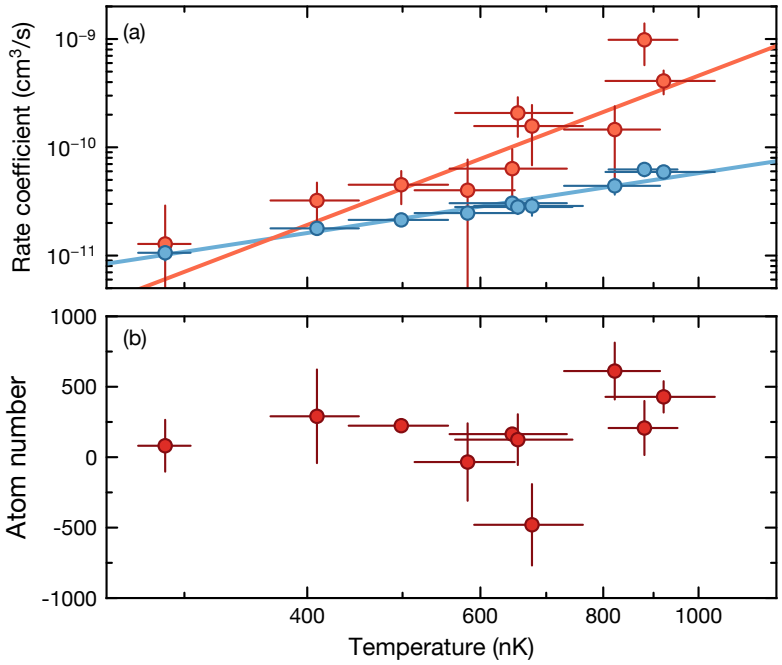

Figure 4.14 – Elastic p-wave collisions in fermionic Feshbach molecules for different temperatures. (a) Elastic collision coefficient β_{el} (red) and inelastic collision coefficient β_{inel} (blue) as a function of the temperature T for a scattering length $a = 610\,a_0$. The error of the fit gives the vertical error bars. The horizontal error bars represent the statistical error of the average temperature during the measurement. A systematic error of 30% in the collision rate is expected from a 10% error in the trapping frequency. The blue and red solid lines are the fits of the polynomial of the form cT^l where $l = 1.39(12)$ and $l = 3.46(63)$ are the exponent of the inelastic and the elastic collisions, respectively. (b) Number of K atoms accumulated in the trap by averaging over the last two hold times of each measurement. To account for a potential background reading of the number of K atoms, we subtracted the number of K atoms from the first two hold times for each respective measurement. The vertical error bar gives the standard error in the number of K atoms.

adiabatic while keeping the ratio between the trapping frequencies fixed. After the compression, the temperatures in the various spatial directions differ. To ensure that cross-dimensional thermalization results from elastic collisions between the Feshbach molecules, we measure a scattering length of $a = 610\,a_0$ where we checked that the number of K atoms does not systematically change for the different temperatures. The results are summarized in Figure 4.14. One can see that the elastic rate coefficient scales stronger with temperature compared to the inelastic one. For temperatures around $T = 300\,\text{nK}$, the rate of elastic and inelastic collisions are comparable, while for $T = 1000\,\text{nK}$, the elastic collision rate is larger by almost one order of magnitude. We fit the temperature scaling with the polynomial cT^l and obtain $l = 1.39(12)$ and $l = 3.46(63)$ for β_{inel} and β_{el}, respectively. The measured temperature scaling of the elastic collision rate agrees reasonably with the $T^{5/2}$ scaling expected for p-wave collisions.

Even in this measurement, we cannot exclude that the elastic collisions between the K atoms and the Feshbach molecules do not affect the extracted rate coefficient. However, we can argue that the main contribution to the cross-dimensional thermalization results from dimer-dimer collisions. To give an upper bound to the contribution of the K-NaK atom-dimer collisions, we note that *s*-wave collisions between distinguishable fermions follow a $T^{1/2}$ scaling. If we account for the fact that the number of detected K atoms does not increase with the temperature (see Figure 4.14b), the K-NaK collisions cannot explain the observed temperature scaling. However, it can explain why the measured temperature dependence is higher than the expected $T^{5/2}$-scaling.

Here is Edward Bear, coming down the stairs now, bump, bump, bump, on the back of his head, behind Christopher Robin. It is, as far as he knows, the only way of coming downstairs, but sometimes he feels that there really is another way, if only he could stop bumping for a moment and think of it. And then he feels that perhaps there isn't.

—A.A. Milne (Winnie-the-Pooh)

5 Production of quantum-degenerate Feshbach molecules

When I started my Ph.D. work on the NaK-machine in November 2018, we conducted our experiments with thermal ground-state molecules. In her thesis, Frauke Seeßelberg reports that the experiment produced 3×10^3 ground-state molecules at a temperature of 300 nK [113]. Around that time, the KRb team at JILA demonstrated the first degenerate molecular sample by producing deeply degenerate atoms which were associated into Feshbach molecules, followed by a transfer into the rovibronic ground state by using STIRAP [43]. As the options to evaporatively cool ground-state molecules [142, 190, 191] were not established at that time, we decided to adopt their method to demonstrate degeneracy for NaK molecules.

As of spring 2021, our experiment routinely produces around 5.0×10^4 Feshbach molecules and 2.5×10^4 ground-state molecules at a temperature of about 100 nK. In this chapter, I will discuss how the production of degenerate NaK molecules is realized in our system, which involves two main steps. First, we change the association procedure from radio-frequency association to magnetoassociation. Second, we use a species-dependent dipole trap to density-match the BEC of Na atoms with a degenerate Fermi gas. Here, I will treat the production of the degenerate gas of molecules on a technical level, while in the next chapter I will present the physical understanding of the association in terms of a phase transition. Both chapters are based on the publication in Ref. [105].

5.1 From radio-frequency association to magnetoassociation

The two most common methods to associate atoms into Feshbach molecules are radio-frequency association and magnetoassociation. For radio-frequency association, a radio-frequency π-pulse transfers the atoms from one hyperfine state directly into the molecular bound state. This method has been used by other experiments working with ^{23}Na^{40}K [47, 49, 178]. Our experiment also previously used radio-frequency association, starting from Na atoms in $|F = 1, m_F = 1\rangle$ and K atoms in $|9/2, -7/2\rangle$ trapped in a crossed optical dipole trap. Using a fast radio-frequency sweep, the atoms were transferred into the Feshbach state which is separated by 80 kHz from the bare atomic state with Na atoms in $|F = 1, m_F = 1\rangle$ and K atoms in $|9/2, -9/2\rangle$. Since radio-frequency association happens on a much faster timescale than the collisions between the particles, two atoms can only be associated into molecules if they are in the ground-state of the relative motion [176, 192]. The probability of finding

two atoms in close proximity in phase space increases for lower temperatures, and thus the association efficiency increases. However, since Na atoms and K atoms exhibit different quantum statistics, their behavior is markedly different in the quantum degenerate regime. As a result, the phase space overlap between Bose–Fermi mixtures drastically reduces once the bosons start to condense. Therefore, the optimized phase space overlap is realized for near-degenerate Bose–Fermi mixtures, namely when the temperature of the bosons is equal to the critical temperature of condensation T_c [55]. Still, the best efficiencies for NaK in this regime range from 10% to 15% when using radio-frequency association [113, 178].

In magnetoassociation, atoms are adiabatically transferred into the bound state by ramping a magnetic field over a Feshbach resonance. This transfer happens on timescales long enough for the atoms to change their momentum distribution during the association. In contrast to association by a radio-frequency pulse, magnetoassociation does not rely on the phase space distribution *at the time of association* as the atoms can redistribute in phase space during the association. The process has peviously been described by a model treating the association into the bound state as a Landau–Zener type transfer [193, 194], the magnetic-field ramp should be slow enough that the unbound state can be adiabatically transferred into the bound state with a probability of $P = 1 - e^{-2\pi\delta_{LZ}}$. The Landau–Zener coefficient $\delta_{LZ} \propto a_{bg}\Delta/\dot{B}$ scales with the width of the resonance Δ and the background scattering length a_{bg} and inversely with the ramp speed of the magnetic field $\dot{B}$ [58]. According to the Landau–Zener models, unity association efficiency can be realized for infinitely slowly magnetic field ramps. However, the strong particle loss in the unitary regime sets a lower bound on the ramp speeds. To utilize magnetoassociation to its fullest potential, one needs a suitable Feshbach resonance, fast and precise control over the magnetic fields, and knowledge of the inelastic collisions that occur in the vicinity of the Feshbach resonance. In the following, I will describe the implementation of magnetoassociation to produce NaK^*, which vastly outperforms radio-frequency association.

5.2 Feshbach association in thermal Bose–Fermi mixtures

We implement magnetoassociation for Bose–Fermi mixtures where the temperature of the bosons is above but close to critical temperature for Bose–Einstein condensation while the K atoms are already in the degenerate regime. We typically refer to these as *thermal* Bose–Fermi mixtures. Since the losses in thermal Bose–Fermi mixtures are minute, it is relatively simple to characterize the association. While we mainly use the Feshbach association of thermal Bose–Fermi mixtures as a testing ground to implement magnetoassociation, this procedure is used to create initial conditions for the loss measurements with Feshbach molecules discussed in Chapter 4.

To characterize the production of Feshbach molecules, we typically start by producing a Bose–Fermi mixture of 5×10^5 K atoms and 3.5×10^5 Na atoms in the 1550/1046-nm dipole trap with trapping frequencies of $2\pi \times (75, 120, 320)$ Hz and $2\pi \times (70, 99, 285)$ Hz for K atoms and Na atoms, respectively. The temperature of the mixture is $T = 450\,\mathrm{nK}$ such

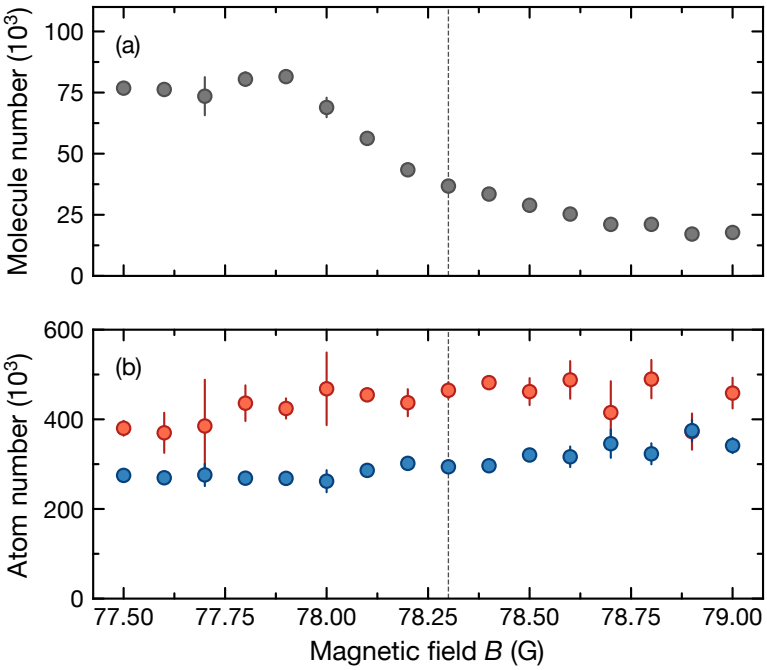

Figure 5.1 – Magnetoassociation of Feshbach molecules in thermal Bose–Fermi mixtures. (a) Number of Feshbach molecules as a function of the final magnetic field. (b) Number of K atoms (red) and Na atoms (blue) as a function of the final magnetic field of the association ramp function. The gray dashed line indicates the resonance position at 78.3 G. The error bars in the measurement are the standard deviation of the measurement with three repetitions.

that $T/T_c = 1.1$ and $T/T_F = 0.45$. After the state preparation of K atoms from $|F, m_F\rangle = |9/2, 9/2\rangle$ to $|9/2, -9/2\rangle$, we associate the molecules by ramping the magnetic field over the 78.3-G Feshbach resonance.

Our first signatures of molecule production with magnetoassociation are based on the detected loss. By ramping the magnetic field through the Feshbach resonance, we see that the number of atoms reduces as a function of the magnetic field. To distinguish the actual loss of particles due to inelastic collisions from molecule production, we probe revival in the number of atoms when ramping the magnetic field back through the Feshbach resonance. While this method indicates that molecules form, we need a better method for detection, especially if we want to perform thermometric measurements on the molecules. Thus, we implement a technique to separate Feshbach molecules and atoms with a magnetic-field gradient in time of flight before detecting the molecules and the atoms. We refer to this imaging technique as Stern–Gerlach imaging. More details on Stern–Gerlach imaging can be found in Section 3.5.2.

The optimized procedure for the Feshbach association is composed of a two-stage magnetic-field ramp. After the state preparation for the K atoms, the mixture thermalizes

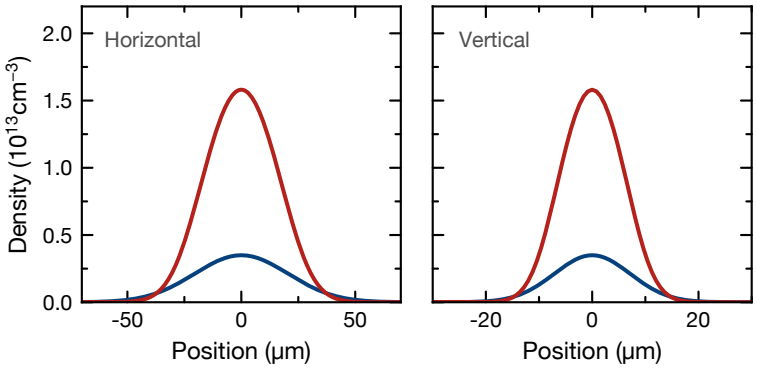

Figure 5.2 – Bose–Fermi mixture in the 1550/1064-nm dipole trap. A cut of the densities in the horizontal direction (left panel) and the vertical direction (right panel) is shown for Na atoms (blue) and K atoms (red). The horizontal direction displayed is along the direction of the Zeeman slower.

at a magnetic field of 81 G. Afterward, we ramp the magnetic field to 79 G, just above the Feshbach resonance. The second ramp from 79 G to 77.8 G serves as the association ramp. The number of associated Feshbach molecules is maximized when the association ramp is performed with a ramp speed of 1.16 G/ms. The molecules and residual atoms are detected by Stern–Gerlach imaging after quickly ramping the magnetic field to 72.3 G.

In Figure 5.1, we show a measurement of the number of molecules and atoms as a function of the endpoint of the association ramp. Once the magnetic field reaches 77.8 G, we produce around 8×10^4 Feshbach molecules. At even lower magnetic fields, the number of Feshbach molecules slightly decreases, likely due to dimer-dimer and Na-dimer inelastic collisions. It might come as a surprise that we detect around 1.5×10^4 Feshbach molecules at magnetic fields above the Feshbach resonance, where no molecules are expected. However, this finite number of detected molecules results from the fast magnetic field ramp to 72.3 G and thus over the Feshbach resonance. Since the ramp is much faster than the typical timescale for elastic collisions in the system, one could argue that the fast magnetic field ramp produces similar molecule numbers as one would expect from a radio-frequency transfer into the bound state. Under this assumption and based on the radio-frequency association performance [113], we conclude that magnetoassociation vastly outperforms radio-frequency association. We also note that the measured temperature of the Feshbach molecules in this measurement is comparable to the temperature of the atoms. We observe that the temperature of the Feshbach molecules is about 20% higher than that of the K atoms.

Changing the association procedure from radio-frequency association to magnetoassociation boosts the number of molecules by approximately a factor of five. However, the molecular sample is not in the Fermi-degenerate regime. From the number of molecules, trapping frequencies, and the temperature of the sample, we estimate that $T/T_F \sim 0.8$. This is not surprising as the atomic Fermi gas is already not deeply degenerate, and only a small fraction of the K atoms are associated into Feshbach molecules.

To characterize the association efficiency, we compare the number of Feshbach molecules

after the association to the number of atoms in minority species before the association. We see that the conversion efficiency of the Na atoms, representing the minority species, is only as large as 21%. From Figure 5.1b it is clear that interspecies loss is not the limiting factor in the association, as the overall number of atoms remains unchanged during the association. Next, we consider the spatial overlap between densities of the bosons and fermions typical to this experiment. In Figure 5.2, one can see that in the wings, the density of the bosons exceeds the density of the fermions, while in the center, the density of the K atoms is considerably higher than the Na atoms. To figure out how many Na atoms can be associated into molecules, we calculate the number of residual Na atoms N_{res} according to

$$N_{\mathrm{res}} = \int_{n_B > n_F} n_B(\boldsymbol{x}) - n_F(\boldsymbol{x})\, \mathrm{d}^3\boldsymbol{x}. \tag{5.1}$$

This tells us how many bosons are in trap regions where the density of the bosons exceeds the density of the fermions and gives an upper bound on the conversion efficiency of the minority species. Using the densities shown in Figure 5.2, we obtain $N_{\mathrm{res}} = 1.1 \times 10^5$. This means that for unity conversion efficiency, we would expect that about two-thirds of the Na atoms can be converted, which is three times larger than what we measure. Therefore, we assume that the phase space overlap represents the major limitation in the association and need to understand which strategy to employ to improve the phase space density of the molecular sample.

5.3 Thermometric considerations for magnetoassociation in NaK

To help us understand how to produce degenerate Feshbach molecules, we consider some simple thermodynamic relations between the atomic gases and molecular clouds. In our simplified treatment, the discussion boils down to relating the relevant energy scales in the system.

We consider a Na-K Bose–Fermi mixture in thermal equilibrium at a temperature T in an optical trap where $\bar{\omega}_{\mathrm{Na}}$ ($\bar{\omega}_{\mathrm{K}}$) is the geometric-mean trapping frequency for the Na (K) atoms and N_{Na} (N_{K}) is the number of bosons (fermions). After Feshbach association, we have N_{NaK^*} Feshbach molecules in an optical trap with a geometric-mean trapping frequency $\bar{\omega}_{\mathrm{NaK}^*}$. Now, we estimate the $(T/T_F)_{\mathrm{NaK}^*}$ for the measurements in the previous section based on the Equation (2.42) for the molecules. Specifically, we assume that the temperature of the molecules is equal to the temperature of the atoms such that $(T/T_F)_{\mathrm{NaK}^*} = (T/T_{F,\mathrm{K}}) \times (T_{F,\mathrm{K}}/T_{F,\mathrm{NaK}^*})$, leading to

$$\left(\frac{T}{T_F}\right)_{\mathrm{NaK}^*} = \left(\frac{\bar{\omega}_{\mathrm{K}}}{\bar{\omega}_{F,\mathrm{NaK}^*}}\right)\left(\frac{N_{\mathrm{K}}}{N_{F,\mathrm{NaK}^*}}\right)^{1/3}. \tag{5.2}$$

Based on the ratio of the trapping frequencies in the 1550/1064-nm crossed dipole trap according to Section 3.4 and that we can associate 8×10^4 molecules from 5×10^5 K atoms at

a reduced temperature of $(T/T_F)_{\mathrm{K}} = 0.45$, we obtain $(T/T_F)_{\mathrm{NaK}^*} = 0.85$.

By combining Eqs. (2.34) and (2.42), we can rewrite $(T/T_F)_{\mathrm{NaK}^*} = (T/T_c) \times (T_c/T_{F,\mathrm{K}}) \times (T_{F,\mathrm{K}}/T_{F,\mathrm{NaK}^*})$ to arrive at the following relation:

$$\left(\frac{T}{T_F}\right)_{\mathrm{NaK}^*} = 0.518(1-\beta)^{1/3} \left(\frac{\bar{\omega}_{\mathrm{Na}}}{\bar{\omega}_{F,\mathrm{NaK}^*}}\right) \left(\frac{N_{\mathrm{Na}}}{N_{F,\mathrm{NaK}^*}}\right)^{1/3}. \tag{5.3}$$

Equation (5.3) implicitly contains the degeneracy of the K atoms due to the fact that the trapping frequencies of the Feshbach molecules are related to the trapping frequencies of the atoms by Equation (3.11). Using Equation (5.3), we can first treat the case of associating Feshbach molecules from thermal bosons ($T = T_c$). We take the geometric-mean trapping frequencies from Table 3.2 and make the simplification that the entirety of the bosons can be converted into Feshbach molecules. Accordingly, the limit is $(T/T_F)_{\mathrm{NaK}^*} = 0.47$.

According to Equation (5.3), we have two possibilities to reduce $(T/T_F)_{\mathrm{NaK}^*}$. We can work with bosons below the critical temperature. However, the dependency of the reduced temperature T/T_F on the condensed fraction scales with the third root of the fraction of thermal bosons. Another parameter we can tune is $\bar{\omega}_{\mathrm{Na}}/\bar{\omega}_{F,\mathrm{NaK}^*}$. This scales linearly, and thus by having a trap that strongly compresses the Feshbach molecules, one can reduce $(T/T_F)_{\mathrm{NaK}^*}$.

Working with condensed bosons or strongly compressing the K atoms will lead to a poor spatial overlap between the bosons and the fermions and, consequently, a bad transfer efficiency. The opposite problem arises when compressing the K atoms while working with a thermal Na cloud where the number of K atoms strongly exceeds the Na cloud, effectively reducing the degeneracy of the Feshbach molecules. This discussion is limited purely to spatial overlap without considering the effect of loss. As we will see in the following section, inelastic collisions complicate this picture.

5.4 Magnetoassociation in degenerate Bose–Fermi mixtures

After implementing the magnetoassociation for thermal Bose–Fermi mixtures, we attempt to produce Feshbach molecules in double-degenerate Bose–Fermi mixtures. Based on the discussion in the previous section, the path to degeneracy constitutes creating a double-degenerate mixture where the K atoms have a considerably stronger confinement than the Na atoms. However, before discussing this scenario, we consider the case of a double-degenerate mixture in a in a crossed dipole trap, where the polarizabilities for the two species are similar (1550/1064-nm trap, see Section 3.4).

5.4.1 Feshbach association in the 1550/1064-nm trap

Starting with 1.5×10^5 Na atoms with a condensed fraction $\beta \approx 60\%$ and a degenerate Fermi gas of 3×10^5 K atoms with a $T/T_F = 0.25$, we ramp the magnetic field over the Feshbach

resonance and detect the number of Feshbach molecules and atoms using Stern–Gerlach imaging. Figure 5.3a shows a scan of the final magnetic field of the Feshbach association. The number of Feshbach molecules formed by this procedure is low, and the process is accompanied by strong loss. Overall, the number of Na atoms drops by 1.0×10^5 during the magnetic-field ramp across the resonance, whereas only 2.5×10^4 Feshbach molecules are produced.

After the association almost none of the condensed Na atoms remain. Therefore, we believe that the bosonic condensate is quickly depleted by loss during the association ramp. According to Figure 5.3, the loss of the Na atoms is correlated to the increase in the number of Feshbach molecules. Given the large Na-dimer loss coefficient measured in Section 4.2, we attribute the loss to inelastic collisions between the Na atoms in the BEC and Feshbach molecules. In an independent measurement, we test this hypothesis by preparing a Bose–Fermi mixture on the repulsive side of the 78.3-G Feshbach resonance and ramping the magnetic field to the attractive side. By ramping in this direction, we probe the loss without the contribution from Na-dimer inelastic collisions. In contrast to the measurement presented in Figure 5.3, we observe no considerable loss.

A comparison between the densities of the Bose–Fermi mixtures in Figure 5.2 and Figure 5.3b shows that the density of the condensed Na atoms is approximately an order of magnitude larger than for thermal Na atoms, while the density of the K atoms slightly reduces. We can compute the number of residual Na atoms according to Equation (5.1). Approximately half of the bosons do not have a "partner" fermion to form Feshbach molecules but can undergo loss. Since the rate coefficient for Na-dimer loss $\beta_{\mathrm{Na-NaK}}$ is almost two orders of magnitude larger than for K-dimer loss $\beta_{\mathrm{K-NaK}}$ (see Figure 4.8), strong interspecies loss arises when the Na atoms are the majority species. The typical timescale of the loss in the center of the trap is considerably faster than a millisecond.

We attempt to reduce the loss by decompressing the 1550/1064-nm dipole trap. In a more radical approach, we even try to perform the association in a crossed dipole trap formed by the lattice beams where we can achieve even lower densities. Both attempts do not prove to be successful. Due to the lower densities, we also need to reduce the ramping speed over the Feshbach resonance. This timescale scales linearly with the overlap density

$$\langle n_< \rangle = \frac{1}{N_<} \int n_B(\boldsymbol{x}) n_F(\boldsymbol{x}) \mathrm{d}^3\boldsymbol{x}\,, \tag{5.4}$$

where $N_<$ is the number of atoms in the minority species. Both, the Na-dimer loss described by Equation (4.27) and the overlap density scale linearly with $n_B(\boldsymbol{x})$. To exploit the scaling relations in our favor, we need to increase the overlap density $\langle n_< \rangle$, while reducing the density of the bosons.

5.4.2 Feshbach association in the 785-nm trap

The nice feature of a species-dependent compression for K atoms is that the ratio of the trapping frequencies $\bar{\omega}_{\mathrm{NaK}^*}/\bar{\omega}_{\mathrm{Na}}$ increases, which according to Equation (5.3), leads to a lower reduced temperature $(T/T_F)_{\mathrm{NaK}^*}$. In addition, the overlap integral between the K

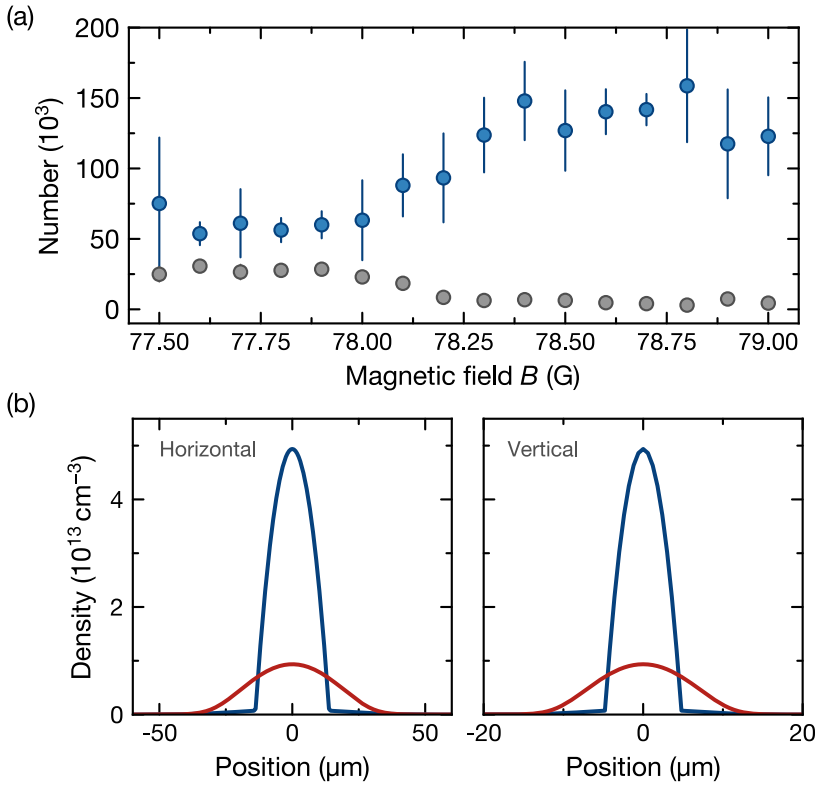

Figure 5.3 – Feshbach association in the 1550/1064-nm dipole trap with a double-degenerate Bose–Fermi mixture. (a) Number of Feshbach molecules (gray) and number of bound and unbound Na atoms (blue) as a function of the magnetic field. The error bars are given by the standard deviation. (b) Cuts of the densities in the horizontal direction (left panel) and the vertical direction (right panel) are shown for Na atoms (blue) and K atoms (red). The horizontal direction displayed is along the direction of the Zeeman slower.

atoms and the degenerate Na atoms increases such that the conversion from the minority species is expected to increase, and loss due to excess bosons to reduce.

We realize this in a 785-nm dipole trap where the trapping frequency of the K atoms is considerably larger than that of the Na atoms. It consists of a light sheet and a tightly focused laser beam compressing the K atoms in the vertical direction and the horizontal direction, respectively (see Section 3.4 for more details). We employ this trap during the optical evaporation in the 1550/1064-nm trap. After the state preparation of the K atoms, we decompress the 1550/1064-nm trap such that the 785-nm dipole trap dominates the confinement of the K and Na atoms. At these low trap depths, a magnetic field gradient is needed to levitate the mixture and compensate for the gravitational sag between the species.

We produce a density-matched mixture of 2.3×10^5 ^{40}K atoms at a temperature $T = 80\,\mathrm{nK}$ (corresponding to $T/T_F \sim 0.2$) and 8.4×10^4 ^{23}Na atoms with a condensate fraction of about 65%. The trapping frequencies in the (x,y,z)-direction are $2\pi \times (72, 90, 187)\,\mathrm{Hz}$ and $2\pi \times (23, 28, 61)\,\mathrm{Hz}$ for K atoms and Na atoms, respectively. For Feshbach association, we employ a series of magnetic-field ramps. First, the magnetic field is quickly ramped to 78.6 G, followed by the association ramp across the Feshbach resonance at 78.3 G with a ramp speed of 3.5 G/ms. This slower ramp stops at 77.8 G where the formation of Feshbach molecules saturates as shown in Figure 5.4a. We then ramp the magnetic field to 72.3 G for Stern–Gerlach separation before imaging.

Following our association procedure, we detect around 5×10^4 Feshbach molecules while observing almost no loss during the association. As shown in Figure 5.4a, the total number of Na atoms does not drop within the error bars of the measurement. We only observe considerable loss due to dimer-dimer and Na-dimer inelastic collisions once the association ramp stops at magnetic fields below 77.8 G. We attribute the improved association to an increase in the density overlap shown in Figure 5.4b combined with a reduced loss because of the low density of residual Na atoms present.

Overall, we can associate 60% of the Na atoms into molecules. Due to the species-dependent trap, the K atoms are predominantly overlapped with the condensed Na atoms, from which can convert 80% into molecules reducing the fraction of residual Na atoms in the BEC to only 7%. If we assume that the residual Na atoms will undergo loss with Feshbach molecules during the formation process, almost the entirety of the BEC can be converted into molecules without such excess bosons. The previously highest conversion efficiencies were achieved in K-Rb mixtures at JILA [43] where less than half of the minority species was converted into molecules. In that experiment, the Bose–Fermi mixture was prepared in a dipole trap where the polarizabilities of the two species were comparable. This means the density-mismatch limits their conversion efficiencies. To improve the density-matching, a fermion-to-boson ratio of 7:1 is used. Due to the ten times lower atom-dimer loss [153, 177], the atoms can be associated efficiently despite the considerably larger density of the Rb-BEC. The high conversion efficiencies obtained in our experiment are also interesting in the sense that they strongly contradict the historical perception that once the bosons condense, the association efficiency is strongly suppressed [57, 58].

At last, I would like to quickly discuss how versatile this method is and how other experiments can use it to achieve degenerate molecules. Extending the technique to other

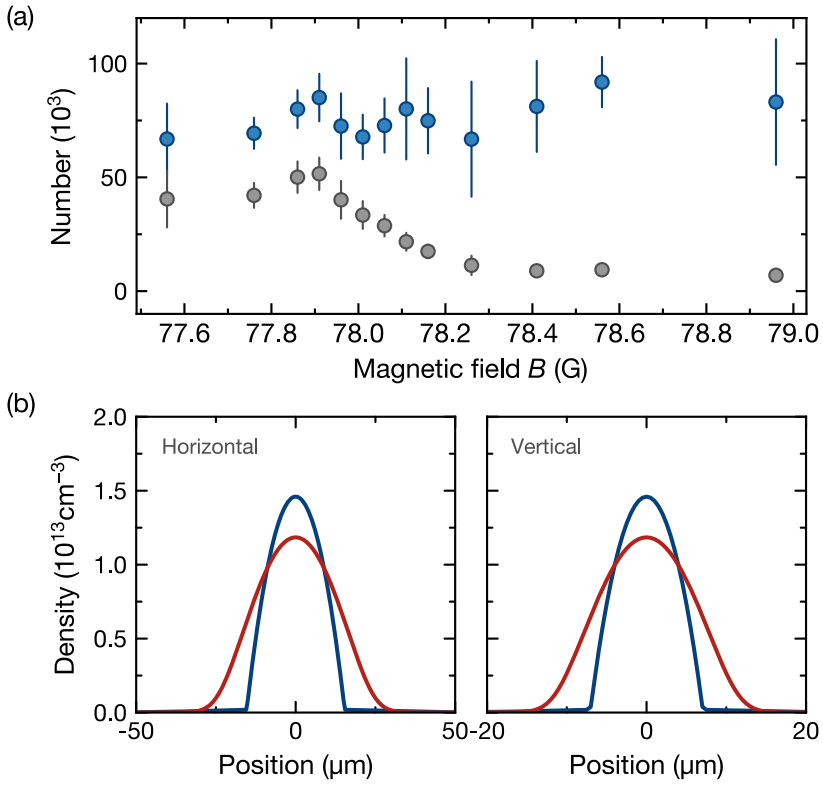

Figure 5.4 – Feshbach association in the 785-nm species-selective dipole trap with a double-degenerate Bose–Fermi mixture. (a) Number of Feshbach molecules (gray) and number of bound and unbound Na atoms (blue). The error bars are given by the standard deviation. (b) Cuts of the densities in the horizontal direction (left panel) and the vertical direction (right panel) is shown for Na atoms (blue) and K atoms (red) before the association. The horizontal direction displayed is along the direction of the Zeeman slower.

Bose–Fermi mixtures seems relatively straightforward. For example, in KRb one could employ a species-dependent dipole trap using a laser that is red-detuned from the *D*-lines of the K atoms and blue detuned from the *D*-lines (or even in-between the *D*-lines) of Rb atoms. Hence, a strong imbalance in the number of bosons and fermions is not needed. It is possible to perform the association with fewer K atoms while increasing the number of Rb atoms and the overlap density, thus increasing the number of Feshbach molecules. Since loss between Feshbach molecules and Rb atoms does not represent a significant problem, the increase in the overlap will lead to an improved association. While our method is particularly powerful in Bose–Fermi mixtures, where the density-mismatch results from the different quantum statistics of the atoms, it can also be beneficial in other experimental setups such as the Li-Cr Fermi–Fermi mixture in Florence. In their case, the lithium and chromium atoms are confined in a bichromatic dipole trap. The laser that traps the chromium with a wavelength of 532 nm light leads to an anti-confinement of the lithium atoms. In this trap configuration, the Fermi gas of lithium is about two to three times larger than that of chromium. Using an additional infrared beam, they compress the lithium axially and density-match it with the chromium [195].

5.5 Transfer to the rovibronic ground state

Once we have produced degenerate NaK* Fesbach molecules, we need to find a way to transfer them into the rovibronic ground state, where the molecules exhibit a large dipole moment. In contrast to the previous section, where we immediately turned off the dipole traps and ramped the magnetic field to 72.3 G for Stern–Gerlach imaging, now, we need to prepare the Feshbach molecular sample before the STIRAP, while maintaining the degeneracy of the molecular gas. This involves a clear out of the residual atoms and compressing the dipole trap to larger trap depths. These steps require some hold time for the Feshbach molecules, for which the sequence needs to be carefully designed to avoid loss and heating of the molecular sample before the transfer to the ground state.

To clear out the atoms, we need the magnetic field to be such that the magnetic moment between the atoms and the molecules is significantly different. Since the association takes place in a trap that is too shallow to hold the molecules without magnetic levitation, ramping to 72.3 G is not an option as the molecules do not possess a magnetic moment at this magnetic field (see Figure 3.10). Instead, we ramp the magnetic field to 75 G where the molecules possess a magnetic moment of $h \times 0.3\,\mathrm{MHz/G}$ and increase the magnetic field gradient to 40 G/cm. Hence, the molecules can be levitated against gravity. At the same time, the gradient is strong enough to remove the residual atoms, which exhibit a considerably stronger magnetic moment, from the trap. It should be noted that choosing a magnetic field of 75 G is a compromise between being able to levitate the molecules and minimizing inelastic collisions between the Feshbach molecules (see Section 4.3.2 for more details of the dimer-dimer inelastic collisions).

We simultaneously ramp the magnetic field and the magnetic-field gradient to levitate the Feshbach molecules at all times. However, the imperfect timing of the ramps as well as eddy currents lead to a temporary tilt of the trap, which induces collective oscillations

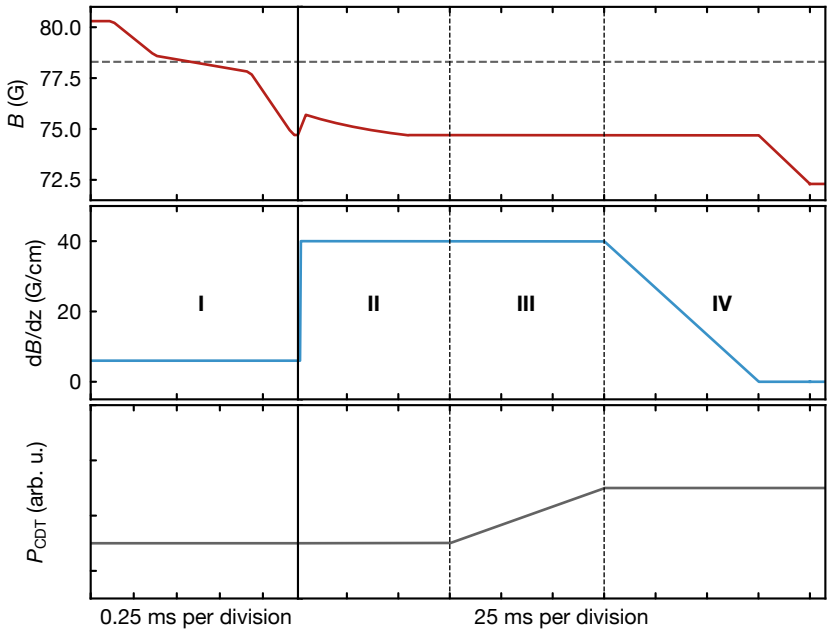

Figure 5.5 – Typical timing sequence for the association of ground-state molecules showing ramps of the magnetic field (red), its gradient (blue) and the power of the 1550/1064-nm trap (gray). I. Association of Feshbach molecules by three-staged magnetic field ramp. II. Removal of unassociated atoms. III. Compression of the 1550/1064-nm trap while the power of the 785-nm trap remains unchanged. IV. Removal of the levitation gradient for subsequent STIRAP pulses. The black vertical solid and dashed lines separate different stages of the sequence. The horizontal gray dashed line marks the Feshbach resonance at 78.3 G.

of the molecular cloud. We minimize the collective oscillations by carefully programming the magnetic field, and subsequently, the magnetic force on the molecules over the course of approximately 25 ms as shown in Figure 5.5. We call this stage "Tai chi" because it is similar to catching and maneuvering a flying ball with gentle movements. Once the collective oscillations have stopped, we compress the 1550/1064-nm trap within 30 ms. Now the trap is deep enough to hold the molecules without magnetic-field levitation, and the magnetic-field gradient is ramped down within 30 ms followed by a magnetic-field ramp to 72.3 G at which the magnetic moment of Feshbach molecules vanishes. After this procedure, the Feshbach molecules are transferred into the rovibronic ground state by Stimulated Raman Adiabatic Passage (STIRAP) with an efficiency of up to 80% [196]. We perform the STIRAP at a magnetic field of 72.3 G, such that the STIRAP pulses are not sensitive to changes in the magnetic field.

After STIRAP, we are left with about 3×10^4 ground-state NaK molecules. Now, that we have found a way to transfer the majority of the Feshbach molecules into the rovibronic ground state, we determine the degeneracy of the molecules to see whether the Feshbach molecules have inherited the degeneracy of the atoms and how the loss of Feshbach molecules affects the degeneracy of the ground-state molecules.

5.6 Fermi-degeneracy of molecules

The quantum degeneracy of the molecular gases is determined by time-of-flight imaging. For Feshbach molecules, we wait for 100 ms after the association to ensure that collective oscillations induced during the association dampen out. During this time, the number of Feshbach molecules reduces by 1×10^4 due to inelastic collisions. However, this waiting time is crucial for fitting the fugacity of the molecular Fermi gas, which is characterized by a small deviation from a Gaussian distribution, as shown in Figure 5.6. Effects on the cloud shape, such as collective oscillations, can influence the extracted fugacity. To extract the reduced temperature T/T_F, we fit the images with the Fermi–Dirac distribution in Equation (3.21) as described in Section 3.5.6.

In Figure 5.6a, we show the radial profile of the Feshbach molecules and ground-state molecules after time of flight. The images are fitted with a Gaussian distribution (red) and Fermi–Dirac distribution (blue). Compared to a Gaussian distribution, the data show a higher occupation at larger momentum which is characteristic of the Fermi pressure in degenerate Fermi gases. From the Fermi–Dirac fit, we obtain a reduced temperature of the Feshbach molecules of $(T/T_F)_{\mathrm{NaK}^*} = 0.28(1)$ and a reduced temperature of the ground-state molecules of $(T/T_F)_{\mathrm{NaK}} = 0.24(4)$.

To the expert reader, this will immediately seem contradictory. How is it possible that the reduced temperature of the Feshbach and ground-state molecules is the same despite a finite STIRAP efficiency of about 80%? It can be explained as follows: As the STIRAP efficiency does not depend on the momentum, the momentum distribution remains unchanged in the absence of elastic collisions. Consequently, while the fugacity of the molecules seems to be high, the system is actually not in thermal equilibrium. Therefore, the fit extracts a seeming reduced temperature which we shall denote as $(T/T_F)^*$. This naturally raises the question of

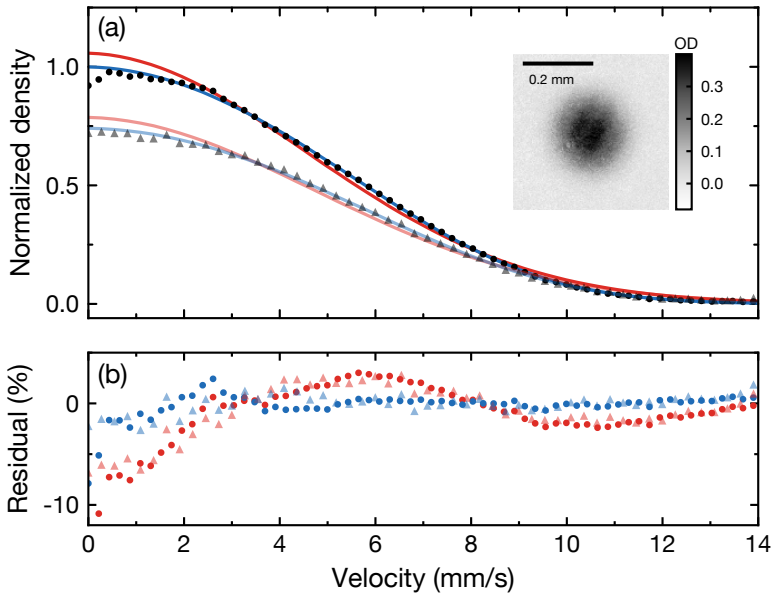

Figure 5.6 – Quantum degeneracy of molecules. (a) Velocity distribution of Feshbach molecules and ground-state molecules. The black points (transparent triangles) show the azimuthal integral of an average of fifteen images (six images) with a time of flight of 15 ms (12 ms) for Feshbach (ground-state) molecules. For the respective species the average image molecules was fitted with a Fermi–Dirac (blue lines) and a Gaussian distribution (red lines). The fit of the Fermi–Dirac distribution results in a fitted $(T/T_F)^*_{\mathrm{NaK}^*} = 0.28(1)$ and $(T/T_F)^*_{\mathrm{NaK}} = 0.24(4)$. The inset shows the averaged absorption image for Feshbach molecules. (b) Azimuthal integral of the residuals for Feshbach molecules (points) and ground-state molecules (triangles).

whether we can even rely on the fitted reduced temperature of the Feshbach molecules, given that these also undergo loss. The underlying assumption is that Feshbach molecules remain in thermal equilibrium during the magnetoassociation [43]. Tobias *et al.* [197] estimate from the elastic collision rate between Feshbach molecules and atomic fermions that the Feshbach molecules are in thermal equilibrium, which also applies in our case. However, once we remove the residual atoms, inelastic loss will lead to the presence of holes in the Fermi sea. If we assume that the loss does not depend on the momentum of the colliding particles, and since the inelastic collision rate is expected to be much larger than the elastic one at 75 G (see Figure 4.13a), the loss of Feshbach molecules should not affect the momentum distribution. Thus, our measurement of the reduced temperature $(T/T_F)^*_{\mathrm{NaK}^*} = 0.28(1)$ which was measured 100 ms after the association, captures the conditions *right after the association*. As a sanity check, we can estimate the expected degeneracy of the Feshbach molecules by considering that the K atoms before the association had a temperature of $T \sim 0.15\ T_F$. Using our experimental conditions, we can obtain $(T/T_F)_{\mathrm{NaK}^*} \sim 0.29$ using Equation (5.2) which reasonably agrees. In the following, we will see how we can estimate the effects of particle loss and finite STIRAP efficiency.

5.7 Thermometry of noninteracting Fermi gases

In this section, I will elaborate on why simply fitting a Fermi–Dirac distribution to extract the degeneracy of a noninteracting Fermi gas can lead to wrong results and which alternative methods can be used. Let us consider a simple thought experiment shown in Figure 5.7, where a deeply degenerate Fermi gas of Feshbach molecules in a harmonic trap is transferred into the rovibronic ground state. For simplicity, we assume that the trap is the same for Feshbach and ground-state molecules and that no other loss processes occur, except a finite STIRAP efficiency $\eta < 1$. In addition, we assume that the transfer efficiency is independent of the momentum of the fermions. Thus, whether a Feshbach molecule gets transferred into the ground-state is simply given by the probability η. Last, we make the simplification that no heating is associated with the transfer to the ground state. Thus, the finite transfer efficiency will lead to holes in the Fermi sea of ground-state molecules and thus increase T/T_F.

In the published work on the first production of degenerate molecules by De Marco *et al.* [43], where the authors claim a reduced temperature of $T/T_F = 0.33(3)$, the effects from the finite STIRAP efficiency have not been accounted for. A difference between their method and ours is that they associate the Feshbach molecules in a trap with a corrugated lattice potential. The purpose is to minimize oscillations after the association and to reduce the effect of the momentum transferred during the STIRAP sequence [43]. Consequently, the Feshbach molecules can be instantly transferred into the ground state after the Feshbach association. Nevertheless, the finite STIRAP efficiency produces holes in the Fermi sea, which do not alter the momentum distribution of the Fermi gas. This means that the reduced temperature that was reported in Ref. [43] for ground-state molecules is the reduced temperature of the Feshbach molecules. I suspect that this issue would be evident if the authors had reported their measured reduced temperature for Feshbach and ground-state molecules.

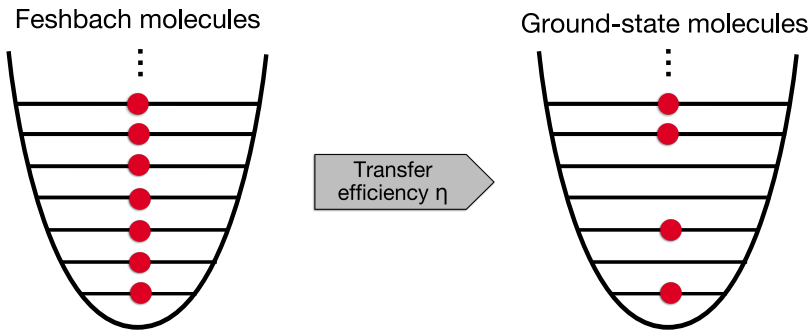

Figure 5.7 – A thought experiment: A deeply degenerate Fermi gas is transferred into the ground state with a finite STIRAP efficiency creating holes in the Fermi sea.

Indeed, in Ref. [197], the authors clarify their results in Ref. [43] by using auxiliary methods to determine the degeneracy of their molecular samples. One method involves probing the number fluctuations between different absorption images for the same experimental condition. The number fluctuations are expected to follow a sub-Poissonian distribution in the degenerate regime, while Poissionian number fluctuations are expected for thermal samples. This method has been established to probe the fugacity of atomic Fermi gases [198]. While the momentum distribution is unaffected by the finite STIRAP efficiency, the finite STIRAP efficiency can be accounted for in the number fluctations. Based on this method, the authors in Ref. [197] report a reduced temperature of $(T/T_F)_{\mathrm{KRb}^*} = 0.35(2)$ and $(T/T_F)_{\mathrm{KRb}} = 0.44(2)$.

This method is quite involved as the images need to be well calibrated to account for image shot noise, atom shot noise, nonlinear effects, finite resolution, etc. The authors also present a method to estimate the degeneracy from the peak fugacity. Here, one relies on the knowledge of the Feshbach molecules' degeneracy and calculates the ground-state molecules' degeneracy based on the transfer efficiency. To illustrate this, we consider the probability distribution $f(\zeta, E)$ in Equation (2.39). We define the lowest state in the harmonic oscillator to have an energy $E = 0$, such that the peak occupancy in terms of the fugacity ζ is given by

$$f(\zeta, E = 0) = (\zeta^{-1} + 1)^{-1}. \tag{5.5}$$

The effect of the finite STIRAP efficiency can be considered to be a random process such that $f(\zeta', E = 0) = \eta \cdot f(\zeta, E = 0)$. Thus, given the occupancy probability of the lowest excited state, one can obtain a new fugacity ζ' from which one can estimate an effective reduced temperature according to Equation (3.22) which is illustrated in Figure 5.8a. Close to the deeply degenerate regime, a small reduction in $f(\zeta, E = 0)$ leads to a rapid increase in $(T/T_F)^*$.

We have decided to estimate the degeneracy of the Fermi gas of ground-state molecules based on the peak fugacity rather than from the number fluctuations. While both methods seem to give similar results, the reduced temperature of the molecular sample can only be truly determined once the sample thermalizes, and the effort associated with measuring the

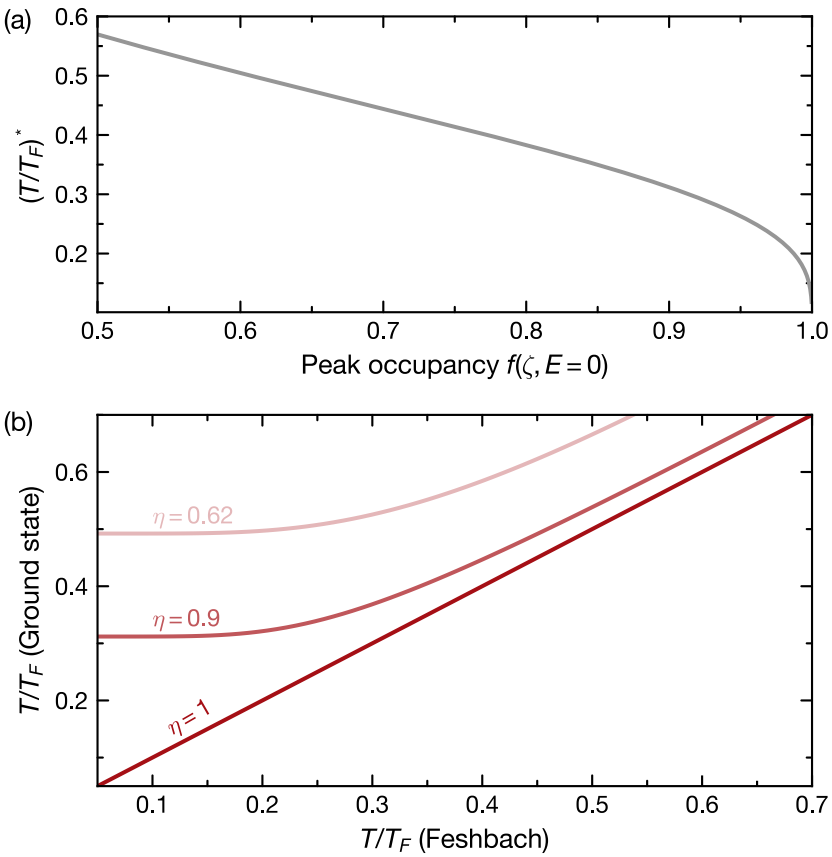

Figure 5.8 – Estimating the reduced temperature of a noninteracting Fermi gas in the presence of loss. (a) Effective reduced temprature $(T/T_F)^*$ with respect to the peak occupancy according to Equation (5.5). (b) Reduced temperature T/T_F of the ground-state molecules based on reduced temperature of the Feshbach molecules according to Equation (5.5) for an ideal transfer $\eta = 1$, the transfer efficiency in the KRb experiment [43] of $\eta = 90\%$ and our experiment in Ref. [105] of $\eta = 62\%$ (from dark to bright red).

number fluctuations is disproportionally more involved. In Figure 5.8b, the effective reduced temperature as a function of the reduced temperature of the Feshbach molecules for the KRb experiment in JILA and for our experiment. As mentioned before, the limiting factor in Refs. [43, 197] is the STIRAP efficiency of $\eta = 90\%$ and 85%, respectively. Depending on the conditions in the respective publication, the degeneracy of the ground-state ranges between $0.37 \leq (T/T_F)_{\mathrm{KRb}} \leq 0.44$. In our experiment, the overall transfer efficiency is given by $\eta = 62\%$ due to a 20%-loss in Feshbach molecules and a STIRAP efficiency of 78%. Given that the initial reduced temperature of the Feshbach molecules is $(T/T_F)_{\mathrm{NaK}^*} = 0.28(1)$, the effective reduced temperature of the ground-state molecules is $(T/T_F)^*_{\mathrm{NaK}} = 0.52(2)$.

5.8 Ground-state molecules in thermal equilibrium

Shortly after successfully creating a quantum-degenerate sample of ground-state molecules with an effective reduced temperature $(T/T_F)^*_{\mathrm{NaK}} = 0.52(2)$, our lab has implemented a technique to do efficient evaporative cooling with ground-state NaK molecules. A circularly polarized microwave shields the inelastic collisions by coupling rotation states, effectively creating a repulsive barrier in all directions. At the same time, the elastic collisions are enhanced by the dipole moment induced by the microwave field. This technique was implemented successfully for the first time in CaF molecules [199], where the authors demonstrate shielding from inelastic collisions between the molecules. Andreas Schindewolf and Roman Bause predominantly performed this work. The details of this project are summarized in Ref. [141] and Roman Bause's Ph.D. thesis [187]. Here, I will only focus on the thermometric analysis performed in this project.

The starting conditions for the evaporation is to produce a noninteracting sample of ground-state molecules at an effective reduced temperature of $(T/T_F)^* \sim 0.5$, as described in Section 5.7. After transferring to the ground state, the power of the microwave is linearly ramped with a voltage-controlled attenuator to prepare the dressed state within 100 μs. After the sample thermalizes, the molecules are evaporated by exponentially ramping the dipole trap to various trap depths. Since technical noise limits the lifetime of the molecules to 600 ms, the timescale of the evaporation is chosen to be 150 ms. In contrast, the final trap depth is varied between the experimental runs. Figure 5.9a shows the measured (T/T_F) as a function of the detected number of molecules. The condition marked with (I) shows a measurement where the trap depth remains constant in the presence of the microwave field, resulting in $T/T_F = 1.0$ (Figure 5.9b). As the final trap depth is being reduced, the reduced temperature decreases, and so does the number of molecules. At best, $T/T_F = 0.47$ with $\sim 4 \times 10^3$ molecules is reached (Figure 5.9c). The evaporation ramp producing condition (II), followed by a plain evaporation of 150 ms leads to condition (III) where we detect $\sim 1 \times 10^3$ molecules with $T/T_F = 0.36$.

Since the microwave allows for the molecular sample to thermalize, we can finally characterize the degeneracy of the molecules. Note, however, that the condition (I) does not

strictly represent the measurement where we estimated $(T/T_F)_{\mathrm{NaK}} = 0.52(2)$ since we hold the molecules for 150 ms where the additional loss occurs. Suppose we account for the additional loss and consider the momentum kick of the STIRAP, which, after thermalizing, will increase the temperature. In that case, we expect $T/T_F \simeq 0.85$ from the peak occupancy argument, which is not far from the measured value. To provide additional proof for the conditions presented in Ref. [105], we could make use of the microwave to thermalize the molecular sample within 10 ms and measure the sample's degeneracy.

While the efficient molecule association can produce large and cold samples, the loss due to the transfer into the ground-state will always remain a strong limit to reducing the degeneracy. Using our molecule association procedure combined with microwave shielding is our experiment's route to obtain deeply degenerate molecular samples.

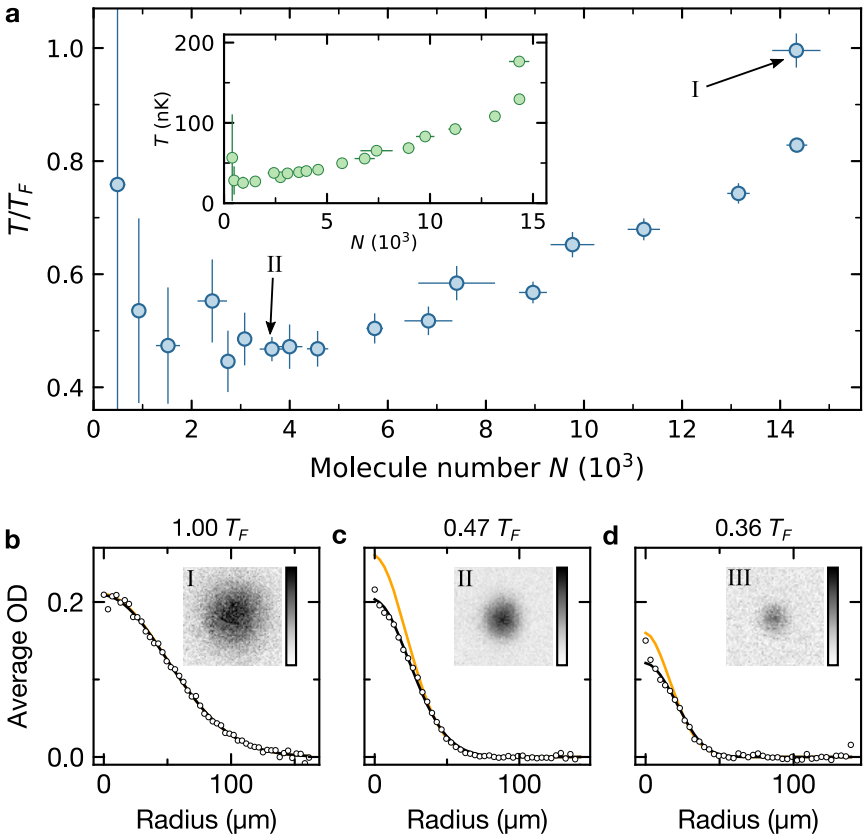

Figure 5.9 – Evaporation of microwave-shielded ground-state molecules (a) T/T_F and T (inset) against the remaining number of molecules N after 150 ms evaporative cooling for various final trap depths. The error bars of N are the standard error of the mean of 5–20 repetitions. The error bars of T are the standard deviation from the fit to the averaged images. (b)–(d) Azimuthally averaged optical density of the samples after 10 ms time of flight. The samples are prepared under the evaporation conditions I (b), II (c), and III (d). Condition III was measured at the same trap depth as condition II followed by plain evaporation for 150 ms The images of the samples are averages from 5 (d), 20 (e), or 6 individual images (f). The black lines show polylogarithmic fit functions, while the orange lines are fits of a Gaussian to the thermal wings of the sample.

As Abraham said: "I am a stranger in a strange land".
—Tevya (Fiddler on the Roof)

6 From weakly-interacting Bose–Fermi mixtures to a degenerate Fermi gas of molecules

After the first attempts to associate Feshbach molecules in Bose–Fermi mixtures, it was believed that the association efficiency depends on the phase-space overlap between the species. In the same publication, phenomenological models to describe the association of Feshbach molecules based on stochastic phase-space sampling (SPSS) further supported this interpretation and showed good agreement with the experimental data [57]. Accordingly, it was believed that a poor phase-space overlap between a BEC and a degenerate Fermi gas was responsible for the low association efficiency [55, 58]. However, as demonstrated for the first time in Ref. [43], the association can be efficient. Moreover, as shown in the previous chapter, the association of Feshbach molecules from degenerate Bose–Fermi mixtures can be highly efficient when the mixture is *spatially* overlapping, and when the interspecies loss can be mitigated.

Given this strong contradiction between the idea that the phase-space overlap determines the association efficiency and our observations, we tried to understand molecule production from a different point of view. In light of previous theoretical investigations of the phase diagram of Bose–Fermi mixtures and their prediction of a phase transition in density-balanced Bose–Fermi mixtures, we investigated this scenario of a quantum phase transition (QPT). This chapter is based on the publication Ref. [105].

6.1 Simplified phase diagram

Since superconductivity was understood to arise from the effective attraction between electrons mediated by phonons, mixtures of interacting bosons and fermions have been the subject of intense research. In solid-state materials, the coupling between electrons (fermions) and phonons (bosons) is captured by Fröhlich or Holstein models [80, 81]. However, these models do not include the possibility of a binding mechanism between bosons and fermions into molecules. As observed in systems such as ultracold atoms [12] and van-der-Waals materials [200] it is possible to realize Bose–Fermi mixtures that are governed by beyond-Fröhlich physics, where bosons and fermions can bind to fermionic molecules [58, 201]. The competition between this novel bound-state physics and mediated interactions leads to an enriched phase diagram potentially featuring supersolidity and charge-density-wave phases [86, 202–204], molecular Fermi liquids [88, 106–108, 110, 205], and unconventional boson-induced superconductivity [85, 206].

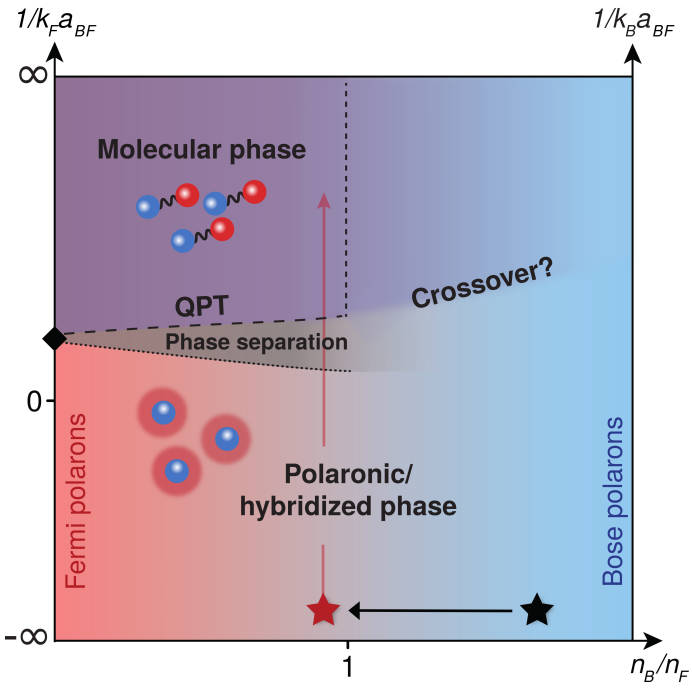

Figure 6.1 – Quantum phase transition in a density-matched Bose–Fermi mixture. Phase diagram of degenerate Bose–Fermi mixtures as a function of the density ratio n_B/n_F and the dimensionless interaction strength $(k_i a_{BF})^{-1}$. For $n_B/n_F \to 0$, one attains the Fermi-polaron limit featuring a polaron-to-molecule transition (black diamond), while for $n_B/n_F \to \infty$, the Bose polaron limit with a smooth crossover is reached when tuning $(k_i a_{BF})^{-1}$. For $n_B < n_F$, a QPT between a Polaronic and a Molecular phase of either first-order with phase separation or second-order is expected. The long-dashed line marks the complete depletion of the condensate $(k_F a_{BF})_c^{-1}$ and, in the case of phase separation, the dotted line marks its onset at $(k_F a_{BF})_{\text{mix}}^{-1}$. The vertical short-dashed line marks a possible further QPT of unknown order.

A simplified phase diagram of homogeneous Bose–Fermi mixtures featuring bound-state physics is illustrated in Figure 6.1 as a function of the boson-to-fermion density ratio n_B/n_F and the dimensionless interaction strength $1/k_i a_{BF}$. Here, a_{BF} denotes the boson-fermion scattering length and the wave vector k_i is determined by the interparticle spacing of the majority species $k_i = (6\pi^2 n_i)^{1/3}$ where i denotes B(F) for $n_B > n_F$ ($n_B < n_F$). We simplify the phase diagram by considering phases at sufficiently high temperatures accessible in our experiment. We ignore for example charge-density waves [86, 202–204] and superfluid s/p-wave fermion pairing mediated by the bosons [85, 86, 206] or bipolaron formation [207]. Also, any phases involving bound states of more than one boson are ignored as these are intrinsically unstable due to fast recombination loss.

Qualitatively, the phase diagram in Figure 6.1 can then be divided into two regimes. In the limit of vanishing Bose–Fermi attraction, $(k_i a_{BF})^{-1} \to -\infty$, bosons and fermions decouple and form a BEC along with a Fermi sea. As attractive interactions are switched

on, fermions and bosons modify each other's properties, leading to quasiparticle formation. Due to the polaronic character of this interaction, we denote the resulting phase as the *Polaronic phase*. This phase is characterized by the existence of a bosonic condensate, thus it is also sometimes denoted as the superfluid polaronic phase [109]. Depending on the ratio of bosons to fermions, the Polaronic phase is either dominated by Bose polarons, where the fermionic impurities are dressed by the bosons, or Fermi polarons, where bosonic impurities are dressed by the Fermi gas. In the limit of strong attraction[1], realized at $(k_i a_{BF})^{-1} \to \infty$, and for $n_B/n_F < 1$, binding of all bosons to fermions leads to a Fermi sea of molecules coexisting with an atomic Fermi sea. In the special case of equal density, only the Fermi sea of molecules exists as all fermionic atoms are bound into molecules. We denote this phase as the *Molecular phase*. In the Molecular phase, the condensate fraction which is the order parameter of this transition has completely vanished. For $n_B/n_F < 1$, the Polaronic and Molecular phase are predicted to be either separated by a first-order QPT with phase separation or by a second-order QPT [76, 106–110].

When tuning the density ratio across $n_B/n_F \approx 1$ in the regime of strong attraction, an additional phase transition, where a condensate reappears, is speculated in Ref. [106], however, as the authors remark, it is not clear whether this phase transition exists or is an artifact of the calculations. For $n_B/n_F \gtrsim 1$, the phase featuring molecules and an excess condensate is predicted to cross over into the Polaronic phase [106].

Most experiments have investigated the far left- or the far right-hand side of the phase diagram. Recently, Bose polarons were observed in the limit of fermionic impurities in a bosonic bath [208, 209], while the existence of a transition from Fermi polarons to molecules has by now been firmly established for impurities immersed in a Fermi sea [98, 99, 103, 104]. In both cases, the density of at least one species is low enough that even for strong interactions, the signatures of the experiments are not masked by strong particle loss. In the case where both species are degenerate, the phase diagram has so far not been explored outside the impurity limits. It is interesting to see how the behavior of Bose–Fermi mixtures changes outside the impurity limits, especially in the equal-density regime where none of the species can be regarded as a quantum impurity. Moreover, this regime is of practical interest to produce a large and degenerate sample of molecules since in the ideal case the number of associated molecules is limited by the number of atoms in the minority species. While the equal-density regime has been investigated by several theoretical works, no experiment has accessed this regime.

The challenge with trapped Bose–Fermi mixtures is that once the bosons condense, their density strongly increases and exceeds the density of the degenerate Fermi gas. Thus, so far, such mixtures have been restricted to the regime of $n_B > n_F$, where it is expected that a crossover from the Polaronic phase to the Molecular phase with excess condensate will occur, which might be accompanied by strong interspecies loss. As discussed in the previous chapter, we can employ a species-dependent trap to change the densities of the mixture from the regime $n_B > n_F$ (indicated by the black star in Figure 6.1) to $n_B \lesssim n_F$ (indicated by the

[1] It is a common perception that the $(k_i a_{BF})^{-1} > 0$ refers to repulsive interactions. However, the molecular phase is characterized by strong attractive interactions given by the binding energy. Whether the interactions are attractive or repulsive depends on whether one is in the attractive or repulsive branch.

red star in Figure 6.1). This allows us to mitigate the loss during the Feshbach association, efficiently associate molecules and study the association procedure.

6.2 Scenario of a quantum phase transition

6.2.1 The measurement

We start the experiment by producing a density-matched mixture of 1.8×10^5 ^{40}K atoms at a temperature $T = 80\,\mathrm{nK}$ (corresponding to $T/T_F \sim 0.2$) and 8.4×10^4 ^{23}Na atoms with a condensate fraction of about 65% in a harmonic trap. The trapping frequencies in the (x, y, z)-direction are $2\pi \times (72, 90, 187)\,\mathrm{Hz}$ and $2\pi \times (23, 28, 61)\,\mathrm{Hz}$ for K atoms and Na atoms, respectively. The corresponding density profiles are shown in Figure 5.4b.

We probe the behavior of the association by ramping the magnetic field across the resonance starting from 79.0 G. To this end, we employ a single magnetic field ramp with a speed of 3.5 G/ms that is terminated at the desired magnetic field close to a Feshbach resonance at 78.3 G [68, 143]. After the target magnetic field has been reached, we then quench the magnetic field to 72.3 G which projects the system onto free atoms and deeply bound molecules to perform Stern–Gerlach separation of the atoms and molecules followed by absorption imaging as shown in Figure 6.2a.

We describe the association process in terms of the dimensionless interaction strength $(k_i a_{BF})^{-1}$. In particular, we make use of the fermionic wave vector $k_i = k_F$ since we work in the regime $n_B \leq n_F$. For the experimental conditions reported above we obtain $k_F = 2\pi \times (1.5 \times 10^6)\,\mathrm{m}^{-1}$. We get the interspecies scattering length a_{BF} between bosons and fermions from Equation (3.27). Due to the small effective-range parameter $k_F R^* = 0.08$ of this broad Feshbach resonance, the Bose–Fermi interactions are well characterized by the single parameter $(k_F a_{BF})^{-1}$ [68]. During the association process the Bose–Bose interaction is weakly repulsive and remains constant $a_{BB} = 53\,a_0$ [68] during the sweep of the magnetic field.

For each measured interaction strength, we fit the images of the Na atoms and the images of the Feshbach molecules with a bimodal distribution and a Gaussian distribution, respectively. As described in Section 3.5, from the fits, we obtain the number of condensed bosons N_{BEC} and the number of thermal bosons N_{th} as well as the number of Feshbach molecules N_{mol}. As shown in Figure 6.2b, the bosonic condensate depletes when the interaction strength increases, accompanied by the emergence of Feshbach molecules. In particular, when $(k_F a_{BF})^{-1} > 0$, the condensate is strongly depleted until it vanishes and the number of Feshbach molecules reaches its maximum. When further increasing the interaction strength, the number of Feshbach molecules decreases, which we attribute to the loss of the Feshbach molecules due to dimer-dimer and Na-dimer inelastic collisions.

6.2.2 Stability of the Bose–Fermi mixture

During the magnetic field ramp over the Feshbach resonance, we strongly change the interspecies interaction a_{BF} in magnitude and sign, while the Bose–Bose interaction a_{BB} re-

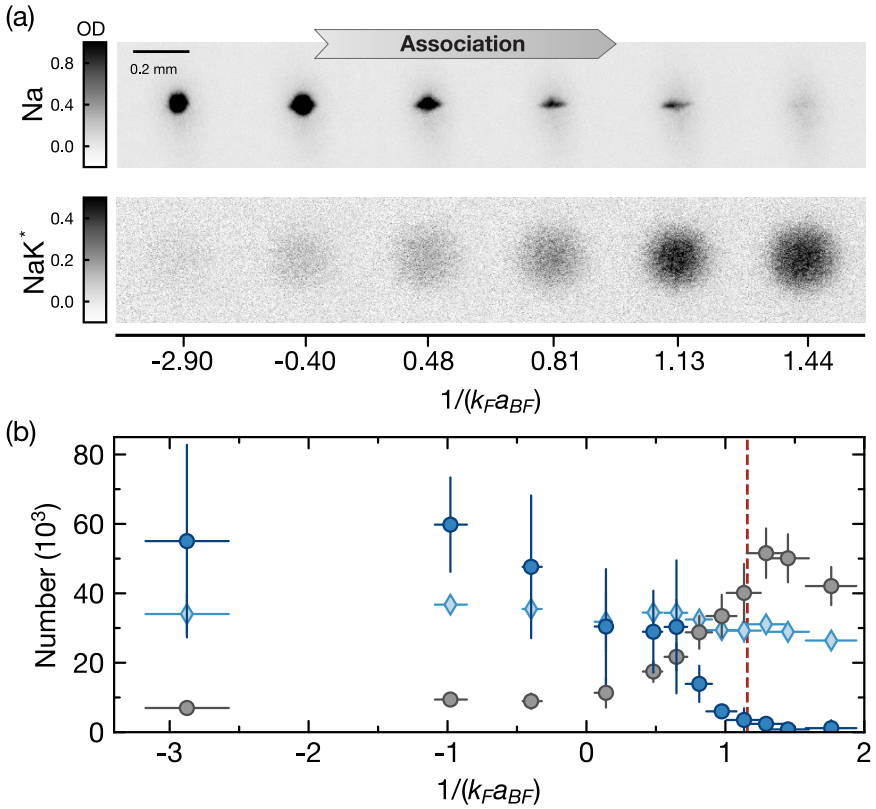

Figure 6.2 – Association process of degenerate Feshbach molecules. (a) Absorption images of Na atoms (Na) and Feshbach molecules (NaK*) after 18 ms time of flight during the association ramp from the polaronic BEC to the Molecular phase. (b) Production of Feshbach molecules. Numbers of condensed Na atoms (dark blue points), thermal Na atoms (light blue diamonds) and Feshbach molecules (gray points) are shown as a function of $(k_F a_{BF})^{-1}$. The red line indicates the polaron-to-molecule transition at $(k_F a_{BF})^{-1} = 1.16$ in the Fermi-polaron problem.

mains weak and repulsive. As pointed out by previous theoretical and experimental works, Bose–Fermi mixtures can undergo collapse or become immiscible in the strongly interacting regime [73, 75–77].

When the interactions between bosons and fermions are attractive and much larger than the stabilizing Bose–Bose repulsion, for $(a_{BF}/a_{BB}) \ll -1$, collapse of the Bose–Fermi mixture is expected. As observed in ^{87}Rb $-^{40}$K mixtures, the strong attraction leads to an enhancement of the density of the mixture and an enhanced particle loss in both species [181]. However, for collapse to occur the mixture needs to undergo global mass transport which happens on the timescale of the trapping period [79]. In our experiment, the trapping period set by the highest trap frequency for bosons (for fermions) is 16 ms (5 ms), which significantly exceeds the timescale of our magnetic-field ramp of less than 1 ms. As shown in Figure 5.4a, we do not observe strong interspecies loss during the magnetic field ramp, which would experimentally signify a collapse in our system. Thus, while collapse does in principle occur in our system it does not represent a problem on the timescales of the experiment.

In the case where the repulsion between bosons and fermions is much larger than the Bose–Bose repulsion, namely for $(a_{BF}/a_{BB}) \gg 1$, the mixture can experience immiscibility, that is, a spatial separation into purely bosonic and fermionic phases that coexist. In contrast to experiments where immiscibility has been observed in Bose–Fermi mixtures at $a_{BF} > 0$ [79], we note that we prepare the system at $1/(k_F a_{BF}) < 0$. As we ramp over the Feshbach resonance, consequently we ramp the mixture along the attractive branch such that the mixture always experiences attractive interspecies interactions. Thus, immiscibility is not expected to pose an issue in our experiment. Moreover, a signature of immiscibility would be that Feshbach-molecule formation is hindered by the spatial separation of the two species. In clear contrast, we show that we can convert $\approx 80\%$ of the BEC into Feshbach molecules, providing direct experimental evidence to rule out immiscibility.

6.2.3 Theoretical models

As previously discussed, the behavior of the Bose–Fermi mixture changes with the interaction strength. A signature of these interactions is the depletion of the condensed bosons, which can be quantified by the condensate fraction n_0/n_B. Here n_0 is the density of the condensed bosons, and n_B is the total density of the bosons. While several publications discuss the association process in the equal-density regime, many of the predictions cannot be used to compare our data with. For example, the works in Ref. [108] study the phase transition in terms of the interaction strength $(a_{BF}/a_{BB}) = \text{const}$, while in our experiment $a_{BB} = \text{const}$. The investigations in Ref. [76, 106] consider the phase transition for a narrow Feshbach resonance which does not apply in our experiment.

In the following, we will compare the change in the condensate fraction to two different calculations. One is based on a non-self-consistent T-matrix (NSCT) theory approach presented in Ref. [110]. In this approach, the authors compute the condensate fraction as a function of $(k_F a_{BF})^{-1}$ for different boson-to-fermion density ratios n_B/n_F up to the equal-density regime where our experiment was performed. A particularly interesting result from this calculation is that the condensate depletion as a function of the interaction strength only

shows a weak dependence on n_B/n_F, and this universality with n_B/n_F extends even down to the Fermi-polaron limit $n_B/n_F \to 0$. Accordingly, the authors establish the relation between the condensate fraction and the quasiparticle weight Z of a single bosonic impurity immersed in the Fermi sea. A disadvantage of the NSCT calculation is that the predicted polaron-to-molecule transition point is not expected to be accurate. This is due to the fact that modifications of the binding energy of the molecules inside the many-body environment are underestimated.

In addition, we compare our data with a calculation of a single bosonic impurity from a self-consistent functional renormalization group (fRG) approach, which accounts for an infinite number of particle-hole excitations in the Fermi sea [94, 210]. Here, we justify comparing an equal-density measurement to an impurity calculation based on the universality of the condensate depletion with n_B/n_F. In the fRG approach, we expect that the polaron-to-molecule transition point is computed more precisely than that from the NSCT approach. This can be attributed to the fact that both the molecule and the polaron are treated on equal footing, such that the *relative* energies between the polaron and molecule are captured more accurately than in an NSCT approach [94, 211]. Unfortunately, the fRG approach to Bose–Fermi mixtures has not yet been developed at finite boson density, and, hence, we have to rely purely on the NSCT prediction in this regime.

In Figure 6.3 we compare the NSCT approach in the impurity limit (black dashed) and in the polaron limit (black solid) and the fRG approach (red solid). One can see that the difference between the two calculations in the impurity limit leads to a difference in the estimated transition point, signified by a jump in the quasiparticle weight Z. The NSCT approach predicts the polaron-to-molecule transition to occur at $(k_F a_{BF})^{-1} = 1.60$ [110] while the fRG approach yields a polaron-to-molecule transition at $(k_F a_{BF})^{-1} = 1.16$. While this seems like a large difference in the predicted transition point, it is important to note that the energies of the attractive Fermi-polaron branch and the molecular branch cross at a rather shallow angle. As a result, the relative underestimation of the molecule energy in the NSCT approach is the main reason for the difference in the predicted location of the polaron-to-molecule transition. Otherwise, the predictions of the quasiparticle weight of a bosonic impurity from both approaches yield similar results. The NSCT calculation at equal density shows a similar depletion behavior of the condensed fraction as the impurity calculations for most of the interaction. Instead of a discontinuity as in the impurity case, the condensed fraction approaches zero continuously, vanishing at the transition point $(k_F a_{BF})_c^{-1} = 2.02$.

6.2.4 Evidence for a quantum phase transition

To characterize the phase transition quantitatively, we define the normalized order parameter

$$\phi = N_{\mathrm{BEC}}/(N_{\mathrm{m}} + N_{\mathrm{BEC}}), \tag{6.1}$$

which describes the depletion of the condensate fraction due to the excitation of bosons to finite-momentum states by quantum fluctuations. These quantum fluctuations are dominated by the build-up of pairing correlations. Said differently, the interactions of the fermions with the bosons lead to a depletion of the bosons in the condensate to occupy finite-momentum

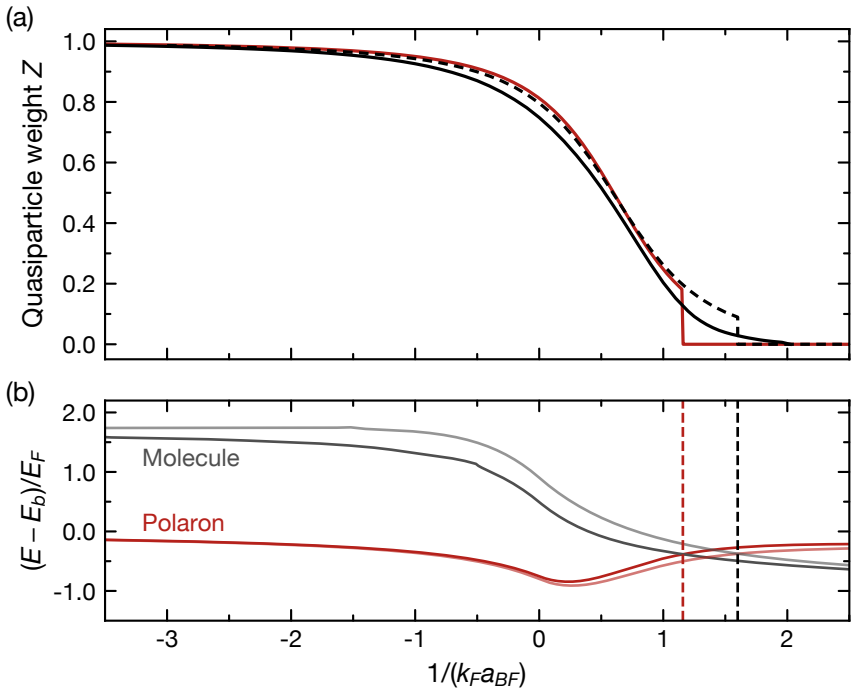

Figure 6.3 – Comparison between fRG and NSCT approach. (a) The quasiparticle weight of the bosonic impurity as a function of the interaction strength is shown as obtained from the fRG (red, solid) and the NSCT approach (black, dashed). While both methods yield similar results, they differ in predicting the point where the polaron-to-molecule transition occurs, beyond which the occupied quasiparticle weight drops to zero. To indicate the effect of finite boson density, the condensate fraction of the mixture computed in NSCT is shown for $n_B/n_F = 1$ (black, solid). (b) Energy spectrum of the zero-momentum Fermi polaron (red lines) and the zero-momentum molecule (gray lines) for a single bosonic impurity obtained from the fRG (solid) and the NSCT (transparent) calculation. The energies cross at the polaron-to-molecule transition $(k_F a_{BF})_c^{-1} = 1.16$ (red dashed line) for the fRG and at $(k_F a_{BF})_c^{-1} = 1.6$ (black dashed line) for the NSCT calculation. For $a_{BF} > 0$, the binding energy $E_b = -\hbar^2/2\mu a_{BF}^2$ is subtracted where μ is the reduced mass.

states, which are then projected onto the deeply bound molecular state.

In order to make a meaningful comparison between the order parameter ϕ according to Equation (6.1) and the condensate fraction or the quasiparticle weight of a single bosonic impurity, we remark that in the definition of ϕ we disregard thermal Na atoms whose number does not change considerably across the full interaction range and whose density is an order of magnitude smaller than that of the BEC. Furthermore, the definition of ϕ is only meaningful if the interspecies loss is small, which is true for the density-matched case as shown in Figure 5.4a.

We have summarized the measured order parameter ϕ as a function of the interaction parameter $(k_F a_{BF})^{-1}$ for two different density ratios $\bar{n}_B/\bar{n}_F$ in Figure 6.4a. Here, $\bar{n}_B/\bar{n}_F$ denotes the ratio of the average boson and fermion density in parts of the trap with a finite condensate fraction in the weakly interacting regime. Specifically, $\bar{n}_B/\bar{n}_F$ is given by

$$\frac{\bar{n}_B}{\bar{n}_F} = \frac{N_F}{N_B} \frac{\int_{n_0>0} n_B^2(\boldsymbol{x})\,\mathrm{d}^3\boldsymbol{x}}{\int_{n_0>0} n_F^2(\boldsymbol{x})\,\mathrm{d}^3\boldsymbol{x}}, \tag{6.2}$$

where the N_F and N_B are the number of fermions and bosons, respectively. The densities of the bosons $n_B(\boldsymbol{x})$ and fermions $n_F(\boldsymbol{x})$ are calculated from the measured conditions before the association process where $n_B(\boldsymbol{x})$ is assumed to be a bimodal distribution and $n_F(\boldsymbol{x})$ is a Fermi–Dirac profile. The order parameter for $\bar{n}_B/\bar{n}_F = 0.7$ (blue) follows from the measured atom numbers shown in Figure 6.2b. The measurement for $\bar{n}_B/\bar{n}_F = 0.4$ (orange) has been performed in the same manner however with fewer Na atoms such that the density of the BEC is reduced.

One can see that in the weakly interacting regime, when the bosons are condensed, the order parameter is largest. As $(k_F a_{BF})^{-1}$ is increased in the regime $(k_F a_{BF})^{-1} < 0$, ϕ only shows a small decrease. Once the scattering length is positive, ϕ decreases rapidly and vanishes in the regime beyond $(k_F a_{BF})^{-1} = 1.44(15)$ ($\bar{n}_B/\bar{n}_F = 0.7$) and $(k_F a_{BF})^{-1} = 1.75(18)$ ($\bar{n}_B/\bar{n}_F = 0.4$) where the residual condensate fraction is comparable to the uncertainty of the measurement.

We observe that both data sets overlap within error bars, providing support for the predicted universality of the condensate depletion for varying n_B/n_F [110]. This universality justifies comparing the theoretical predictions in a homogeneous system with our in-trap experiment where the boson-to-fermion density n_B/n_F changes depending on the position in the trap. Moreover, it legitimizes the comparison of the equal-density regime with the impurity calculations if we assume that the universality does indeed extend to the impurity limit.

Our measurements qualitatively agree well with the predicted condensate fraction from the NSCT approach throughout the entire interaction regime and also show a remarkable agreement with the quasiparticle weight of a single impurity from the fRG approach (solid red line) in most of the interaction regime except close to the phase transition.

We attribute the discrepancy between the data and theoretical predictions in the weakly interacting regime to the projective measurement when jumping the field across the Feshbach resonance. Since it is impossible in our measurement to perform the time of flight and

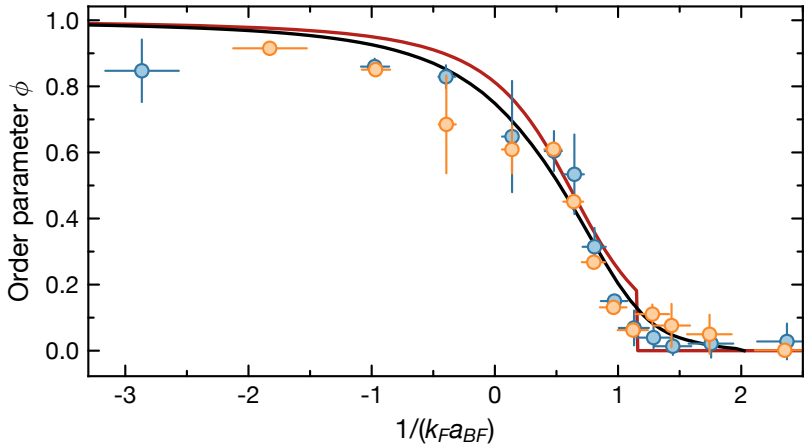

Figure 6.4 – Order parameter ϕ as a function of $(k_F a_{BF})^{-1}$ for the boson-fermion average-density ratio $\bar{n}_B/\bar{n}_F = 0.4$ (orange points) and $\bar{n}_B/\bar{n}_F = 0.7$ (blue points). The error bars in $(k_F a_{BF})^{-1}$ result from the magnetic field uncertainty of 15 mG and an error of 10 % in the average trapping frequency. The vertical error bars represent the standard error. The black solid line shows the order parameter from zero-temperature theory in Ref. [110] predicting the QPT to occur at $(k_F a_{BF})_c^{-1} = 2.02$ for ideal bosons interacting with a Fermi gas at $n_B/n_F = 1$. The red solid line shows the quasiparticle weight of a bosonic impurity in a Fermi gas obtained from a self-consistent functional renormalization group (fRG) calculation that predicts the polaron-to-molecule transition to occur at $(k_F a_{BF})_c^{-1} = 1.16$.

the imaging at any specific interaction strength, we project the system onto deeply bound Feshbach molecules. However, due to eddy currents, the jump of the magnetic field cannot be performed infinitely fast, and as a result, we associate a finite number of Feshbach molecules. In contrast, according to Bogoliubov theory, the condensate fraction expected to scale as $n_0/n = 1 - 8/3(\eta/\pi)^{1/2} \approx 1$ [212]. Here, η is the interaction parameter off the bosons given by $\eta = \bar{n}_B a_{BB}^3 \sim 10^{-7}$. Accordingly, ϕ is expected to be at unity which is reproduced by the NSCT calculations [110].

6.2.5 Determination of the transition point

As part of investigating the quantum phase transition, we try to obtain the transition point $(k_F a_{BF})_c$, namely the interaction parameter when the condensate completely vanishes. As previously mentioned, for $\bar{n}_B/\bar{n}_F = 0.7$ the condensate vanishes at $(k_F a_{BF})^{-1} = 1.44(15)$, and for $\bar{n}_B/\bar{n}_F = 0.4$ at $(k_F a_{BF})^{-1} = 1.75(18)$. However, it is quite difficult to determine the transition point from the experimentally determined condensate fraction for two reasons: First, this quantity only slowly approaches zero. Second, several factors such as the presence of excess bosons or particle loss can shift the experimentally determined transition point. While are working in the regime where $\bar{n}_B/\bar{n}_F < 1$, where on average the density of the bosons is smaller than the fermions, the density of the bosons can exceed the density of the fermions in the center of the trap. For $\bar{n}_B/\bar{n}_F = 0.7$, one expects the fraction of excess bosons to be as large as 7%. These excess bosons cannot be converted into molecules and

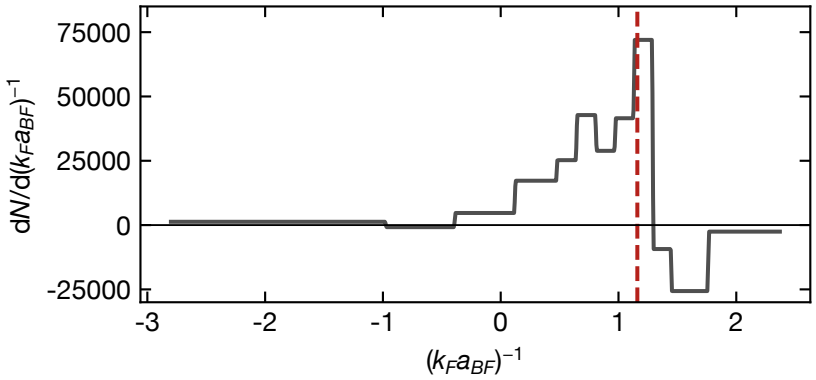

Figure 6.5 – Molecule production in the association process. The change in the number of molecules is extracted from the data in Figure 6.2b. To this end, we have performed a linear interpolation between the data points and extracted the derivative. The red dashed line indicates the transition point in the impurity limit from the fRG calculation.

thus the experimentally determined transition point would be overestimated. On the other hand, there is particle loss which can lead to the depletion of the condensate and might underestimate the transition point. In addition, shot-to-shot fluctuations in the number of Na and K atoms can lead to fluctuations in the number of condensate atoms, and when $\bar{n}_B/\bar{n}_F \lesssim 1$, these fluctuations can lead to a systematic overestimation of the transition point $(k_F a_{BF})_c$. In essence, the vanishing condensate fraction, we cannot judge whether our data are in closer agreement with the transition point $(k_F a_{BF})_c = 1.16$ from the fRG approach or $(k_F a_{BF})_c = 2.02$ from the NSCT approach in the equal-density regime.

To estimate the transition point independently from the slowly varying order parameter, we consider the projected Feshbach molecule number shown in Figure 6.2b as a measure of existing boson-fermion pairing correlations. As $(k_F a_{BF})^{-1}$ increases, so do the pairing correlations (including potential fermion-molecule mixing [106]) until they saturate when the bosons are fully bound into molecules. We extract the transition point $(k_F a_{BF})^{-1} = 1.29(14)$ where the number of detected molecules saturates. Moreover, the behavior in the growth of the molecules changes abruptly, as shown in Figure 6.5. While below the transition point, the growth rate of the molecules increases with the interaction strength, the growth rate becomes negative once $(k_F a_{BF})^{-1} = 1.29(14)$.

The extracted value of the transition point from the change in the number of molecules seems to be in reasonable agreement with $(k_F a_{BF})_c = 1.16$ from the fRG calculations, considering that we compare a measurement at finite bosons density to the Fermi-polaron limit. As explicitly shown in [88, 103, 110, 213] and suggested by mean-field arguments [88], one expects the transition to shift to larger values of $(k_F a_{BF})^{-1}$ as the boson density increases. Moreover, from investigations of two-component Fermi gases (and as we see from the NSCT calculations), it is expected that the discontinuity from the fRG calculations will be smoothened out due to finite boson density, temperature, or combinations thereof [103, 213]. Hence, the value of $(k_F a_{BF})^{-1} = 1.16$ obtained from the fRG in the impurity limit can be regarded as a lower bound on the actual location of the quantum phase transition at

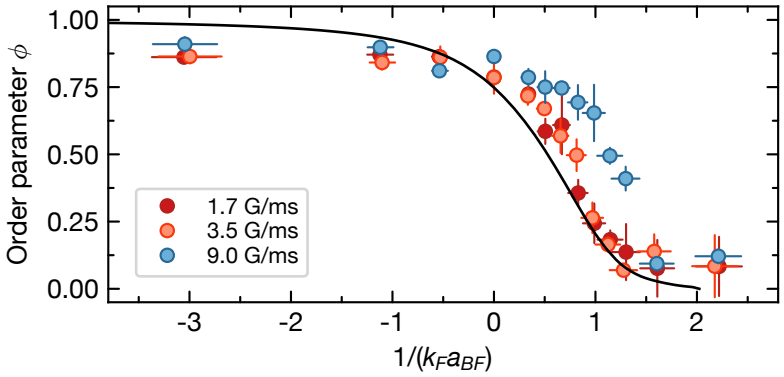

Figure 6.6 – Feshbach association at various ramp speeds. Order parameter ϕ as a function of $(k_F a_{BF})^{-1}$ at ramp speeds of 1.7 G/ms (dark red points), 3.5 G/ms (light red points) and 9 G/ms (blue points).

$(k_F a_{BF})_c$.

At last, I would like to remark on the adiabaticity of the association ramp. With a ramp speed of 3.5 G/ms the timescale of the ramp is long enough to accommodate several atom-dimer collisions in the strongly interacting regime such that the Feshbach molecules are in thermal equilibrium with the atoms [197]. However, the time scale is too short for the system to be in global thermal equilibrium given by the trapping period. Moreover, as shown in Figure 6.4b, the energies of the polaron and the molecule at the transition point are gapless such that adiabaticity is only guaranteed for an infinetly slowly magnetic field ramp. To verify that our chosen ramp speed does not shift the transition point, we measure ϕ as a function of $(k_F a_{BF})^{-1}$ for three different ramp speeds as shown in Figure 6.6. For the ramp speeds of 1.7 G/ms and 3.5 G/ms we observe the same behavior in the condensate depletion. Only for the fastest ramp speed of 9 G/ms the depletion is shifted towards higher $(k_F a_{BF})^{-1}$.

6.2.6 Reversal of the phase transition

We investigate the reversal of the phase transition. After the association ramp reaches $(k_F a_{BF})^{-1} = 1.3$, the magnetic field is again ramped back over the resonance to dissociate the molecules. The dissociation ramp is again followed by a magnetic-field quench to 72.3 G for detection. As can be seen from the time-of-flight images in Figure 6.7a, the number of projected Feshbach molecules decreases, while a finite BEC fraction is recovered. In particular, we show that the number of Na atoms in the BEC can be increased from $3(2) \times 10^3$ to $8(1) \times 10^3$ (see Figure 6.7b). Heating after the dissociation is evident in the form of an increase of thermal Na atoms which we attribute to the non-adiabatic nature of the magnetic field ramps near the transition point. Due to the changing number of Na atoms in the thermal wings, we cannot characterize the reversal of the phase transition with the order parameter ϕ as done in the association ramp. Nonetheless, the partial restoration of the BEC highlights the coherence preserved in our experiment and is a striking example of how bosons that were bound to fermionic molecules in finite-momentum states are converted back into their

motional ground state.

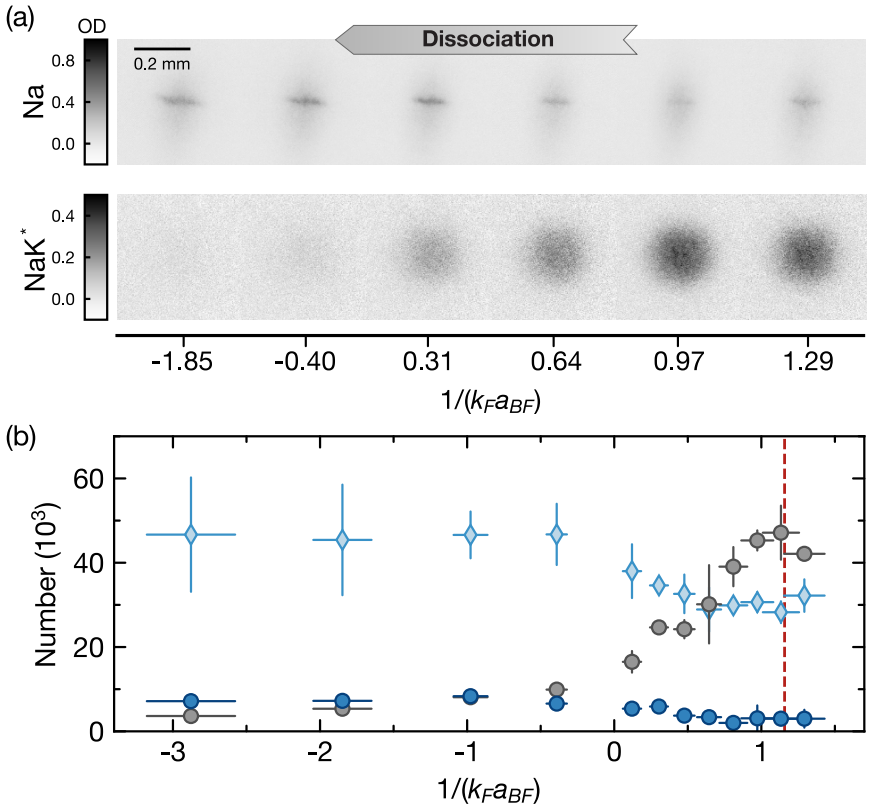

Figure 6.7 – Association process of degenerate Feshbach molecules. (a) Absorption images of Na atoms (Na) and Feshbach molecules (NaK^*) after 18 ms time of flight during the association ramp from the polaronic BEC to the Molecular phase. (b) Production of Feshbach molecules. Numbers of condensed Na atoms (dark blue points), thermal Na atoms (light blue diamonds) and Feshbach molecules (gray points) are shown as a function of $(k_F a_{BF})^{-1}$ for $\bar{n}_B/\bar{n}_F = 0.7$. The red line indicates the polaron-to-molecule transition at $(k_F a_{BF})^{-1} = 1.16$ in the Fermi-polaron problem.

6.3 A first step in understanding the QPT

We have investigated the association of Feshbach molecules in an equal-density Bose–Fermi mixture. We see that the data agree with the scenario of a quantum phase transition. In particular, we have seen that the condensate depletion reasonably agrees with the NSCT calculation and even with the quasiparticle weight of a single bosonic impurity in a fermionic bath.

The universality of the condensate depletion with the boson-to-fermion density indicates that, despite having a large boson density, the system can be well described as a condensate of polaronically dressed bosons. Moreover, the association in equal-density Bose–Fermi

mixtures can be understood in the Fermi-polaron picture. A possible explanation for the universality is, as recently observed, that the interactions between the polarons are weak [104]. From theory and experiment, it is not clear whether or how far the universality exceeds beyond $n_B/n_F > 1$. As a consequence of the universality, probing the condensate fraction as a function of the dimensionless interaction represents an alternative way to obtain the quasiparticle weight of one boson immersed into a Fermi sea. While this method might not be as accurate as radio-frequency spectroscopy [99] or Raman spectroscopy [103], it is also considerably less involved.

This work provides a first step toward understanding the phase diagram in the equal-density regime. Many open questions remain to be answered, most prominently the order of the phase transition. Theoretical investigations suggest that a first-order transition accompanied by phase separation is expected for weak repulsion, while for stronger repulsion a second-order transition is expected [108]. Revealing the nature of this quantum phase transition in our experiment is complicated by the accessible observables. For instance, we can only measure the global but not a locally resolved condensate fraction. As a result, we expect to observe a trap-averaged and thus continuously measured condensate fraction as a function of $1/k_F a_{BF}$ *both* for a first-order transition featuring phase separation and for a second-order transition. While for a second-order phase transition, a continuous condensate fraction is expected, for a first-order phase transition in a homogeneous system, the condensate fraction would jump locally as a result of phase separation. However, since we only have access to the globally averaged quantities, these discontinuities are smoothened out by looking at the global condensate fraction. Probing the order of the phase transition could be done by trying to measure hysteresis. Our data in Figure 6.2b and Figure 6.7b actually suggest such a hysteresis. The Feshbach molecule formation and dissociation seem to be systematically shifted. This needs to be investigated in more detail. For example, the magnetic field needs to be precisely checked when performing the dissociation. A complementary method to identify the order of the transition is by measuring in a box trap where the density of the mixture is homogeneous. This provides a better chance to see whether the condensate fraction shows a discontinuous behavior.

Also, similar to the superfluid-to-Mott-insulator quantum phase transition [214], it would be interesting to characterize the temperature dependence of the phase transition as done in Ref. [215]. Thus, one can obtain the critical temperatures where the Polaronic or the Molecular phase exists. Furthermore, it would be possible to obtain critical exponents for the transition. This is an involved task as the experimental parameters need to be calibrated for each different temperature at which the experiment is performed while ensuring that the overlap between the species is maintained.

7 Conclusion and outlook

In this thesis, I have described the process for creating ground-state NaK molecules in the quantum-degenerate regime. The bottleneck and thus focus of this work lies in the association of the Feshbach molecules in degenerate atomic Bose–Fermi mixtures. Based on the experience from other mixture experiments and our observations, we concluded that radio-frequency association does not allow to associate atoms into molecules with sufficiently high efficiency, especially when the atoms are degenerate. Therefore, we implemented magnetoassociation into our setup, which involved the characterization of the interspecies Feshbach resonance at a magnetic field of 78.3 G. We used thermal Bose–Fermi mixtures as a testing ground for the magnetoassociation and demonstrated that it vastly outperforms the previously used radio-frequency association and allows us to produce around 8×10^4 Feshbach molecules at a temperature close to the Fermi temperature. We also studied the various loss processes in the proximity of the 78.3-G Feshbach resonance identifying that three-body and Na-dimer collisions significantly contribute to particle loss close to unitarity. By associating double-degenerate Bose–Fermi mixtures, where the density of the bosons vastly exceeded the density of the fermions, we found a strong loss of Na atoms within the BEC during the molecule-formation process. We developed a method to mitigate the strong interspecies loss by density-matching the double-degenerate mixture using a species-dependent dipole trap that predominantly confines the Fermi gas of K atoms. In density-matched Bose–Fermi mixtures, we demonstrated an overall conversion efficiency of the Na atoms into Feshbach molecules of 60% and negligible loss. We showed that the Feshbach molecules have a reduced temperature of $(T/T_F) \approx 0.3$ and the ground-state molecules have an effective reduced temperature of $(T/T_F) \approx 0.5$. In this context, we discussed methods to approximate the degeneracy of noninteracting Fermi gases in the presence of loss. In the last section, we addressed the nature of the association process. By converting around 80% of the Na atoms in the BEC into molecules, we demonstrated that the association of condensed atoms into Feshbach molecules is possible and highly efficient. Moreover, we showed that the production of molecules in Bose–Fermi mixtures can be understood as a phase transition from a phase featuring a condensate to a phase featuring a Fermi sea of Feshbach molecules.

This work provides essential insights into creating degenerate ground-state molecules from Bose–Fermi mixtures. In contrast to previous observations doubting the possibility of efficient association when the bosons condense [58, 177], we observe close-to-unity association efficiencies of the condensed bosons limited by residual density mismatch. Since our method relies on the simple idea of density-matching the mixture with a dual-color dipole trap, I believe that our technique will prove to be useful in reaching quantum degeneracy in other polar-molecule experiments. Furthermore, our work provides a first step in exploring strong-correlation physics in degenerate Bose–Fermi systems away from the impurity limits and serves as a benchmark for their theoretical understanding. Our data suggest that

the condensate depletion is accompanied by the build-up of pairing correlations between the bosons and fermions, which ultimately leads to the formation of molecules. In particular, the depletion of the order parameter agrees with the scenario of a quantum phase transition which is closely linked to the polaron-to-molecule transition in the Fermi-polaron problem. The investigation of the order of the transition through the observation hysteresis [108], or absence thereof, is an intriguing venue for future research. Studies on the temperature dependence of the critical point and on the quantum critical dynamics [216] will shed further light on the nature of this transition. Given that the theoretical predictions of the phase transition are limited to densities $n_B \leq n_F$, explorations of the phase diagram for $n_B \gtrsim n_F$ will be very interesting to see whether the quantum phase transition persists for $n_B > n_F$, given that a crossover is expected in the Bose-polaron limit.

Our experiment has finally reached the status of studying dipolar physics with ultracold molecules. With the recent progress in creating degenerate molecules with the method presented here and microwave-assisted evaporation [141], we can create a thousand ground-state molecules at a temperature of $T = 0.36T_F$, which to date is the most degenerate sample of interacting polar molecules in three dimensions. Upgrading the microwave system will further improve the performance of the evaporation. We have developed additional features for the setup in the past years, such as optical lattices and rotational-state dependent potentials. With these tools and due to the strong intrinsic dipole moment of 2.7 Debye in NaK, we expect a plethora of fascinating phenomena predicted in dipolar systems.

We recently observed anisotropic expansion of the polar molecules due to the dipolar interactions in time of flight. To show the dipolar interactions in degenerate polar molecules, one could study the deformation of the Fermi surface [217], which has previously been observed in magnetic atoms of Erbium [218]. Our molecules exhibit a stronger dipole moment than magnetic atoms, so we expect a substantially larger deformation. This would be the first many-body effect observed in degenerate molecules with dipolar interactions.

A more challenging but feasible project would be the observation of a condensate of rotational excitation, where the rotating molecules synchronize their rotation in an optical lattice. This idea was predicted in Refs. [219, 220]. To observe this effect, the molecules need to be loaded into an optical lattice and be brought into a superposition between the rotational ground state and the first excited rotational state. If the loading in the lattice is very small, one expects that the rotations will dephase. However, if the filling in the lattice is sufficiently high, the molecules feel the presence of the neighboring dipoles and rotate in phase. Observing this phenomenon requires a filling of about 15% of the molecules in the lattice, which corresponds to the filling we have achieved recently. This number can be improved with the recent upgrades to the microwave system. To see a signature of the condensate of rotational excitations, we would perform Ramsey spectroscopy on the ground-state molecules for different lattice fillings. The coherence time of the rotations should qualitatively change once the critical lattice filling of 15% is reached.

At last, we can dream a bit: An interesting idea is to use microwaves and tune the scattering between the ground-state molecules [221]. If the microwave is strong enough, one can modify the attractive potential of the intramolecular potential to host a bound state. In analogy to Feshbach resonances discussed in this thesis, one can modify the scattering length of

the molecules. Moreover, one can transfer the molecules into a tetramers which condense if the sample is sufficiently cold and long-lived.

Bibliography

1. Anderson, M. H., Ensher, J. R., Matthews, M. R., Wieman, C. E. & Cornell, E. A. Observation of Bose-Einstein Condensation in a Dilute Atomic Vapor. *Science* **269,** 198–201 (1995) (cit. on p. 1).
2. Davis, K. B., Mewes, M.-O., Andrews, M. R., van Druten, N. J., Durfee, D. S., Kurn, D. M. & Ketterle, W. Bose-Einstein Condensation in a Gas of Sodium Atoms. *Phys. Rev. Lett.* **75,** 3969–3973 (1995) (cit. on p. 1).
3. Andrews, M. R., Townsend, C. G., Miesner, H.-J., Durfee, D. S., Kurn, D. M. & Ketterle, W. Observation of Interference Between Two Bose Condensates. *Science* **275,** 637–641 (1997) (cit. on p. 1).
4. Bloch, I., Hänsch, T. W. & Esslinger, T. Measurement of the Spatial Coherence of a Trapped Bose Gas at the Phase Transition. *Nature* **403,** 166–170 (2000) (cit. on p. 1).
5. DeMarco, B., Bohn, J. L., Burke, J. P., Holland, M. & Jin, D. S. Measurement of *p*-Wave Threshold Law Using Evaporatively Cooled Fermionic Atoms. *Phys. Rev. Lett.* **82,** 4208–4211 (1999) (cit. on pp. 1, 6, 75).
6. Truscott, A. G., Strecker, K. E., McAlexander, W. I., Partridge, G. B. & Hulet, R. G. Observation of Fermi Pressure in a Gas of Trapped Atoms. *Science* **291,** 2570–2572 (2001) (cit. on p. 1).
7. Schreck, F., Khaykovich, L., Corwin, K. L., Ferrari, G., Bourdel, T., Cubizolles, J. & Salomon, C. Quasipure Bose-Einstein Condensate Immersed in a Fermi Sea. *Phys. Rev. Lett.* **87,** 080403 (2001) (cit. on p. 1).
8. Greiner, W., Neise, L. & Stöcker, H. in *Thermodynamics and Statistical Mechanics* 341–386 (Springer Science & Business Media, 2012) (cit. on p. 1).
9. Grimm, R., Weidemüller, M. & Ovchinnikov, Y. B. in *Advances in Atomic, Molecular, and Optical Physics* (eds Bederson, B. & Walther, H.) 95–170 (Academic Press, 2000) (cit. on pp. 1, 26, 28).
10. Jaksch, D. Optical Lattices, Ultracold Atoms and Quantum Information Processing. *Contemp. Phys.* **45,** 367–381 (2004) (cit. on p. 1).
11. Bloch, I., Dalibard, J. & Zwerger, W. Many-Body Physics with Ultracold Gases. *Rev. Mod. Phys.* **80,** 885–964 (2008) (cit. on p. 1).
12. Chin, C., Grimm, R., Julienne, P. & Tiesinga, E. Feshbach Resonances in Ultracold Gases. *Rev. Mod. Phys.* **82,** 1225–1286 (2010) (cit. on pp. 1, 11, 67, 99).
13. Schreck, F. & van Druten, K. Laser Cooling for Quantum Gases. *Nat. Phys.* **17,** 1296–1304 (2021) (cit. on p. 1).

14. Bakr, W. S., Gillen, J. I., Peng, A., Fölling, S. & Greiner, M. A Quantum Gas Microscope for Detecting Single Atoms in a Hubbard-regime Optical Lattice. *Nature* **462,** 74–77 (2009) (cit. on p. 1).

15. Barredo, D., Lienhard, V., de Léséleuc, S., Lahaye, T. & Browaeys, A. Synthetic Three-Dimensional Atomic Structures Assembled Atom by Atom. *Nature* **561,** 79–82 (2018) (cit. on p. 1).

16. Aveline, D. C., Williams, J. R., Elliott, E. R., Dutenhoffer, C., Kellogg, J. R., Kohel, J. M., Lay, N. E., Oudrhiri, K., Shotwell, R. F., Yu, N. & Thompson, R. J. Observation of Bose–Einstein Condensates in an Earth-orbiting Research Lab. *Nature* **582,** 193–197 (2020) (cit. on p. 1).

17. Griesmaier, A., Werner, J., Hensler, S., Stuhler, J. & Pfau, T. Bose-Einstein Condensation of Chromium. *Phys. Rev. Lett.* **94,** 160401 (2005) (cit. on p. 1).

18. Lu, M., Youn, S. H. & Lev, B. L. Trapping Ultracold Dysprosium: A Highly Magnetic Gas for Dipolar Physics. *Phys. Rev. Lett.* **104,** 063001 (2010) (cit. on p. 1).

19. Aikawa, K., Frisch, A., Mark, M., Baier, S., Rietzler, A., Grimm, R. & Ferlaino, F. Bose-Einstein Condensation of Erbium. *Phys. Rev. Lett.* **108,** 210401 (2012) (cit. on p. 1).

20. Baier, S., Mark, M. J., Petter, D., Aikawa, K., Chomaz, L., Cai, Z., Baranov, M., Zoller, P. & Ferlaino, F. Extended Bose-Hubbard Models with Ultracold Magnetic Atoms. *Science* **352,** 201–205 (2016) (cit. on p. 1).

21. Saffman, M., Walker, T. G. & Mølmer, K. Quantum Information with Rydberg Atoms. *Rev. Mod. Phys.* **82,** 2313–2363 (2010) (cit. on p. 1).

22. Baranov, M. A., Mar'enko, M. S., Rychkov, V. S. & Shlyapnikov, G. V. Superfluid Pairing in a Polarized Dipolar Fermi Gas. *Phys. Rev. A* **66,** 013606 (2002) (cit. on p. 1).

23. Cooper, N. R. & Shlyapnikov, G. V. Stable Topological Superfluid Phase of Ultracold Polar Fermionic Molecules. *Phys. Rev. Lett.* **103,** 155302 (2009) (cit. on p. 1).

24. Shi, T., Zhang, J.-N., Sun, C.-P. & Yi, S. Singlet and Triplet Bardeen-Cooper-Schrieffer Pairs in a Gas of Two-Species Fermionic Polar Molecules. *Phys. Rev. A* **82,** 033623 (2010) (cit. on p. 1).

25. Wu, Z., Block, J. K. & Bruun, G. M. Liquid Crystal Phases of Two-Dimensional Dipolar Gases and Berezinskii-Kosterlitz-Thouless Melting. *Sci. Rep.* **6,** 19038 (2016) (cit. on p. 1).

26. Bruun, G. M. & Taylor, E. Quantum Phases of a Two-Dimensional Dipolar Fermi Gas. *Phys. Rev. Lett.* **101,** 245301 (2008) (cit. on p. 1).

27. Matveeva, N. & Giorgini, S. Liquid and Crystal Phases of Dipolar Fermions in Two Dimensions. *Phys. Rev. Lett.* **109,** 200401 (2012) (cit. on p. 1).

28. Baranov, M. A., Dalmonte, M., Pupillo, G. & Zoller, P. Condensed Matter Theory of Dipolar Quantum Gases. *Chem. Rev.* **112,** 5012–5061 (2012) (cit. on p. 1).

29. DeMille, D. Quantum Computation with Trapped Polar Molecules. *Phys. Rev. Lett.* **88,** 067901 (2002) (cit. on p. 1).

30. Yelin, S. F., Kirby, K. & Côté, R. Schemes for Robust Quantum Computation with Polar Molecules. *Phys. Rev. A* **74,** 050301 (2006) (cit. on p. 1).

31. Ni, K.-K., Rosenband, T. & Grimes, D. D. Dipolar Exchange Quantum Logic Gate with Polar Molecules. *Chem. Sci.* **9,** 6830–6838 (2018) (cit. on p. 1).

32. Safronova, M. S., Budker, D., DeMille, D., Kimball, D. F. J., Derevianko, A. & Clark, C. W. Search for New Physics with Atoms and Molecules. *Rev. Mod. Phys.* **90,** 025008 (2018) (cit. on p. 1).

33. Weinstein, J. D., deCarvalho, R., Guillet, T., Friedrich, B. & Doyle, J. M. Magnetic Trapping of Calcium Monohydride Molecules at Millikelvin Temperatures. *Nature* **395,** 148–150 (1998) (cit. on p. 2).

34. Takekoshi, T., Patterson, B. M. & Knize, R. J. Observation of Optically Trapped Cold Cesium Molecules. *Phys. Rev. Lett.* **81,** 5105–5108 (1998) (cit. on p. 2).

35. Tokunaga, S. K., Dyne, J. M., Hinds, E. A. & Tarbutt, M. R. Stark Deceleration of Lithium Hydride Molecules. *New J. Phys.* **11,** 055038 (2009) (cit. on p. 2).

36. Wall, T. E., Kanem, J. F., Dyne, J. M., Hudson, J. J., Sauer, B. E., Hinds, E. A. & Tarbutt, M. R. Stark Deceleration of CaF Molecules in Strong- and Weak-Field Seeking States. *Phys. Chem. Chem. Phys.* **13,** 18991–18999 (2011) (cit. on p. 2).

37. Vanhaecke, N., Meier, U., Andrist, M., Meier, B. H. & Merkt, F. Multistage Zeeman Deceleration of Hydrogen Atoms. *Phys. Rev. A* **75,** 031402 (2007) (cit. on p. 2).

38. Lavert-Ofir, E., Gersten, S., Henson, A. B., Shani, I., David, L., Narevicius, J. & Narevicius, E. A Moving Magnetic Trap Decelerator: A New Source of Cold Atoms and Molecules. *New J. Phys.* **13,** 103030 (2011) (cit. on p. 2).

39. Lavert-Ofir, E., David, L., Henson, A. B., Gersten, S., Narevicius, J. & Narevicius, E. Stopping Paramagnetic Supersonic Beams: The Advantage of a Co-Moving Magnetic Trap Decelerator. *Phys. Chem. Chem. Phys.* **13,** 18948–18953 (2011) (cit. on p. 2).

40. Hutzler, N. R., Lu, H.-I. & Doyle, J. M. The Buffer Gas Beam: An Intense, Cold, and Slow Source for Atoms and Molecules. *Chem. Rev.* **112,** 4803–4827 (2012) (cit. on p. 2).

41. Fitch, N. J. & Tarbutt, M. R. in *Advances In Atomic, Molecular, and Optical Physics* (eds Dimauro, L. F., Perrin, H. & Yelin, S. F.) 157–262 (Academic Press, 2021) (cit. on p. 2).

42. Wu, Y., Burau, J. J., Mehling, K., Ye, J. & Ding, S. High Phase-Space Density of Laser-Cooled Molecules in an Optical Lattice. *Phys. Rev. Lett.* **127,** 263201 (2021) (cit. on p. 2).

43. De Marco Luigi, L. D., Valtolina, G., Matsuda, K., Tobias, W. G., Covey, J. P. & Ye, J. A Degenerate Fermi Gas of Polar Molecules. *Science* **363,** 853–856 (2019) (cit. on pp. 2, 3, 33, 79, 87, 93–96, 99).

44. Ni, K.-K., Ospelkaus, S., de Miranda, M. H. G., Pe'er, A., Neyenhuis, B., Zirbel, J. J., Kotochigova, S., Julienne, P. S., Jin, D. S. & Ye, J. A High Phase-Space-Density Gas of Polar Molecules. *Science* **322,** 231–235 (2008) (cit. on p. 2).

45. Takekoshi, T., Reichsöllner, L., Schindewolf, A., Hutson, J. M., Le Sueur, C. R., Dulieu, O., Ferlaino, F., Grimm, R. & Nägerl, H.-C. Ultracold Dense Samples of Dipolar RbCs Molecules in the Rovibrational and Hyperfine Ground State. *Phys. Rev. Lett.* **113,** 205301 (2014) (cit. on p. 2).

46. Molony, P. K., Gregory, P. D., Ji, Z., Lu, B., Köppinger, M. P., Le Sueur, C. R., Blackley, C. L., Hutson, J. M. & Cornish, S. L. Creation of Ultracold $^{87}Rb^{133}Cs$ Molecules in the Rovibrational Ground State. *Phys. Rev. Lett.* **113,** 255301 (2014) (cit. on p. 2).

47. Park, J. W., Will, S. A. & Zwierlein, M. W. Ultracold Dipolar Gas of Fermionic $^{23}Na^{40}K$ Molecules in Their Absolute Ground State. *Phys. Rev. Lett.* **114,** 205302 (2015) (cit. on pp. 2, 79).

48. Seeßelberg, F., Buchheim, N., Lu, Z.-K., Schneider, T., Luo, X.-Y., Tiemann, E., Bloch, I. & Gohle, C. Modeling the Adiabatic Creation of Ultracold Polar $^{23}Na^{40}K$ Molecules. *Phys. Rev. A* **97,** 013405 (2018) (cit. on p. 2).

49. Liu, L., Zhang, D.-C., Yang, H., Liu, Y.-X., Nan, J., Rui, J., Zhao, B. & Pan, J.-W. Observation of Interference between Resonant and Detuned Stirap in the Adiabatic Creation of $^{23}Na^{40}K$ Molecules. *Phys. Rev. Lett.* **122,** 253201 (2019) (cit. on pp. 2, 79).

50. Guo, M., Zhu, B., Lu, B., Ye, X., Wang, F., Vexiau, R., Bouloufa-Maafa, N., Quéméner, G., Dulieu, O. & Wang, D. Creation of an Ultracold Gas of Ground-State Dipolar $^{23}Na^{87}Rb$ Molecules. *Phys. Rev. Lett.* **116,** 205303 (2016) (cit. on p. 2).

51. Rvachov, T. M., Son, H., Sommer, A. T., Ebadi, S., Park, J. J., Zwierlein, M. W., Ketterle, W. & Jamison, A. O. Long-Lived Ultracold Molecules with Electric and Magnetic Dipole Moments. *Phys. Rev. Lett.* **119,** 143001 (2017) (cit. on p. 2).

52. Voges, K. K., Gersema, P., Meyer zum Alten Borgloh, M., Schulze, T. A., Hartmann, T., Zenesini, A. & Ospelkaus, S. Ultracold Gas of Bosonic $^{23}Na^{39}K$ Ground-State Molecules. *Phys. Rev. Lett.* **125,** 083401 (2020) (cit. on p. 2).

53. Cairncross, W. B., Zhang, J. T., Picard, L. R. B., Yu, Y., Wang, K. & Ni, K.-K. Assembly of a Rovibrational Ground State Molecule in an Optical Tweezer. *Phys. Rev. Lett.* **126,** 123402 (2021) (cit. on p. 2).

54. Stevenson, I., Lam, A. Z., Bigagli, N., Warner, C., Yuan, W., Zhang, S. & Will, S. *Ultracold Gas of Dipolar NaCs Ground State Molecules* 2022. arXiv: 2206.00652 (cit. on p. 2).

55. Zirbel, J. J., Ni, K.-K., Ospelkaus, S., Nicholson, T. L., Olsen, M. L., Julienne, P. S., Wieman, C. E., Ye, J. & Jin, D. S. Heteronuclear Molecules in an Optical Dipole Trap. *Phys. Rev. A* **78,** 013416 (2008) (cit. on pp. 2, 80, 99).

56. Ni, K.-K. The Quest for Quantum Degeneracy. *Nat. Phys.* **15,** 526–527 (2019) (cit. on p. 3).

57. Hodby, E., Thompson, S. T., Regal, C. A., Greiner, M., Wilson, A. C., Jin, D. S., Cornell, E. A. & Wieman, C. E. Production Efficiency of Ultracold Feshbach Molecules in Bosonic and Fermionic Systems. *Phys. Rev. Lett.* **94,** 120402 (2005) (cit. on pp. 3, 87, 99).

58. Cumby, T. D., Shewmon, R. A., Hu, M.-G., Perreault, J. D. & Jin, D. S. Feshbach-Molecule Formation in a Bose-Fermi Mixture. *Phys. Rev. A* **87,** 012703 (2013) (cit. on pp. 3, 80, 87, 99, 113).

59. Moses, S. A., Covey, J. P., Miecnikowski, M. T., Yan, B., Gadway, B., Ye, J. & Jin, D. S. Creation of a Low-Entropy Quantum Gas of Polar Molecules in an Optical Lattice. *Science* **350,** 659–662 (2015) (cit. on p. 3).

60. Reichsöllner, L., Schindewolf, A., Takekoshi, T., Grimm, R. & Nägerl, H.-C. Quantum Engineering of a Low-Entropy Gas of Heteronuclear Bosonic Molecules in an Optical Lattice. *Phys. Rev. Lett.* **118,** 073201 (2017) (cit. on pp. 3, 33).

61. Geist, W., You, L. & Kennedy, T. A. B. Sympathetic Cooling of an Atomic Bose-Fermi Gas Mixture. *Phys. Rev. A* **59,** 1500–1508 (1999) (cit. on p. 6).

62. Top, F. Ç. p-*Wave Collisions in Ultracold Fermions* PhD thesis (Massachusetts Institute of Technology, Cambridge, 2020) (cit. on p. 7).

63. Idziaszek, Z. Analytical Solutions for Two Atoms in a Harmonic Trap: *p*-Wave Interactions. *Phys. Rev. A* **79,** 062701 (2009) (cit. on p. 7).

64. Marcelis, B., Kokkelmans, S. J. J. M. F., Shlyapnikov, G. V. & Petrov, D. S. Collisional Properties of Weakly Bound Heteronuclear Dimers. *Phys. Rev. A* **77,** 032707 (2008) (cit. on pp. 7, 8, 70, 74).

65. Hutson, J. M. Feshbach Resonances in Ultracold Atomic and Molecular Collisions: Threshold Behaviour and Suppression of Poles in Scattering Lengths. *New J. Phys.* **9,** 152–152 (2007) (cit. on p. 8).

66. Idziaszek, Z. & Julienne, P. S. Universal Rate Constants for Reactive Collisions of Ultracold Molecules. *Phys. Rev. Lett.* **104,** 113202 (2010) (cit. on pp. 8, 72, 74).

67. Simonucci, S., Pieri, P. & Strinati, G. C. Broad vs. Narrow Fano-Feshbach Resonances in the BCS-BEC Crossover with Trapped Fermi Atoms. *EPL* **69,** 713 (2005) (cit. on p. 11).

68. Viel, A. & Simoni, A. Feshbach Resonances and Weakly Bound Molecular States of Boson-Boson and Boson-Fermion NaK Pairs. *Phys. Rev. A* **93,** 042701 (2016) (cit. on pp. 11, 46, 48, 49, 102).

69. Butts, D. A. & Rokhsar, D. S. Trapped Fermi Gases. *Phys. Rev. A* **55,** 4346–4350 (1997) (cit. on p. 12).

70. Pethick, C. & Smith, H. in *Bose-Einstein Condensation in Dilute Gases* 16–39 (Cambridge University Press, Cambridge ; New York, 2002) (cit. on pp. 13, 14).

71. Dalfovo, F., Giorgini, S., Pitaevskii, L. P. & Stringari, S. Theory of Bose-Einstein Condensation in Trapped Gases. *Rev. Mod. Phys.* **71,** 463–512 (1999) (cit. on p. 14).

72. Ketterle, W. & Zwierlein, M. W. Making, Probing and Understanding Ultracold Fermi Gases. *La Rivista del Nuovo Cimento* **31,** 247–422 (2008) (cit. on p. 15).

73. Mølmer, K. Bose Condensates and Fermi Gases at Zero Temperature. *Phys. Rev. Lett.* **80,** 1804–1807 (1998) (cit. on pp. 15, 104).

74. Ospelkaus, C. *Fermi-Bose Mixtures - From Mean-Field Interactions to Ultracold Chemistry* PhD thesis (Universität Hamburg, Hamburg, 2006) (cit. on p. 17).

75. Viverit, L., Pethick, C. J. & Smith, H. Zero-Temperature Phase Diagram of Binary Boson-Fermion Mixtures. *Phys. Rev. A* **61,** 053605 (2000) (cit. on pp. 16, 104).

76. Marchetti, F. M., Mathy, C. J. M., Huse, D. A. & Parish, M. M. Phase Separation and Collapse in Bose-Fermi Mixtures with a Feshbach Resonance. *Phys. Rev. B* **78,** 134517 (2008) (cit. on pp. 16, 101, 104).

77. Yu, Z.-Q., Zhang, S. & Zhai, H. Stability Condition of a Strongly Interacting Boson-Fermion Mixture across an Interspecies Feshbach Resonance. *Phys. Rev. A* **83,** 041603 (2011) (cit. on pp. 16, 104).

78. Ospelkaus, C., Ospelkaus, S., Sengstock, K. & Bongs, K. Interaction-Driven Dynamics of ^{40}K-^{87}Rb Fermion-Boson Gas Mixtures in the Large-Particle-Number Limit. *Phys. Rev. Lett.* **96,** 020401 (2006) (cit. on p. 16).

79. Zaccanti, M., D'Errico, C., Ferlaino, F., Roati, G., Inguscio, M. & Modugno, G. Control of the Interaction in a Fermi-Bose Mixture. *Phys. Rev. A* **74,** 041605 (2006) (cit. on pp. 16, 104).

80. Fröhlich, H. Electrons in Lattice Fields. *Adv. Phys.* **3,** 325–361 (1954) (cit. on pp. 16, 99).

81. Holstein, T. Studies of Polaron Motion. *Ann. Phys.* **8,** 325–389 (1959) (cit. on pp. 16, 99).

82. Tempere, J., Casteels, W., Oberthaler, M. K., Knoop, S., Timmermans, E. & Devreese, J. T. Feynman Path-Integral Treatment of the BEC-impurity Polaron. *Phys. Rev. B* **80,** 184504 (2009) (cit. on p. 16).

83. Casteels, W., Van Cauteren, T., Tempere, J. & Devreese, J. T. Strong Coupling Treatment of the Polaronic System Consisting of an Impurity in a Condensate. *Laser Phys.* **21,** 1480 (2011) (cit. on p. 16).

84. Shashi, A., Grusdt, F., Abanin, D. A. & Demler, E. Radio-Frequency Spectroscopy of Polarons in Ultracold Bose Gases. *Phys. Rev. A* **89,** 053617 (2014) (cit. on p. 16).

85. Kinnunen, J. J., Wu, Z. & Bruun, G. M. Induced *p*-Wave Pairing in Bose-Fermi Mixtures. *Phys. Rev. Lett.* **121,** 253402 (2018) (cit. on pp. 16, 99, 100).

86. Enss, T. & Zwerger, W. Superfluidity near Phase Separation in Bose-Fermi Mixtures. *Eur. Phys. J. B* **68,** 383–389 (2009) (cit. on pp. 16, 99, 100).

87. Watanabe, T., Suzuki, T. & Schuck, P. Bose-Fermi Pair Correlations in Attractively Interacting Bose-Fermi Atomic Mixtures. *Phys. Rev. A* **78,** 033601 (2008) (cit. on p. 18).

88. von Milczewski, J., Rose, F. & Schmidt, R. Functional-Renormalization-Group Approach to Strongly Coupled Bose-Fermi Mixtures in Two Dimensions. *Phys. Rev. A* **105,** 013317 (2022) (cit. on pp. 18, 99, 109).

89. Landau, L. D. Über Die Bewegung Der Elektronen in Kristallgitter. *Phys. Z. Sowjetunion* **3,** 644–645 (1933) (cit. on p. 18).

90. Chevy, F. & Mora, C. Ultra-Cold Polarized Fermi Gases. *Rep. Prog. Phys.* **73,** 112401 (2010) (cit. on p. 18).

91. Massignan, P., Zaccanti, M. & Bruun, G. M. Polarons, Dressed Molecules and Itinerant Ferromagnetism in Ultracold Fermi Gases. *Rep. Prog. Phys.* **77,** 034401 (2014) (cit. on p. 18).

92. Levinsen, J. & Parish, M. M. in Madison, K. W., Bongs, K., Carr, L. D., Rey, A. M. & Zhai, H. *Annual Review of Cold Atoms and Molecules* 1–75 (World Scientific, 2015) (cit. on p. 18).

93. Chevy, F. Universal Phase Diagram of a Strongly Interacting Fermi Gas with Unbalanced Spin Populations. *Phys. Rev. A* **74,** 063628 (2006) (cit. on p. 19).

94. Schmidt, R. & Enss, T. Excitation Spectra and Rf Response near the Polaron-to-Molecule Transition from the Functional Renormalization Group. *Phys. Rev. A* **83,** 063620 (2011) (cit. on pp. 19, 20, 105).

95. Nascimbène, S., Navon, N., Jiang, K. J., Tarruell, L., Teichmann, M., McKeever, J., Chevy, F. & Salomon, C. Collective Oscillations of an Imbalanced Fermi Gas: Axial Compression Modes and Polaron Effective Mass. *Phys. Rev. Lett.* **103,** 170402 (2009) (cit. on p. 20).

96. Scazza, F., Valtolina, G., Massignan, P., Recati, A., Amico, A., Burchianti, A., Fort, C., Inguscio, M., Zaccanti, M. & Roati, G. Repulsive Fermi Polarons in a Resonant Mixture of Ultracold ^{6}Li Atoms. *Phys. Rev. Lett.* **118,** 083602 (2017) (cit. on p. 20).

97. Kohstall, C., Zaccanti, M., Jag, M., Trenkwalder, A., Massignan, P., Bruun, G. M., Schreck, F. & Grimm, R. Metastability and Coherence of Repulsive Polarons in a Strongly Interacting Fermi Mixture. *Nature* **485,** 615–618 (2012) (cit. on p. 20).

98. Koschorreck, M., Pertot, D., Vogt, E., Fröhlich, B., Feld, M. & Köhl, M. Attractive and Repulsive Fermi Polarons in Two Dimensions. *Nature* **485,** 619–622 (2012) (cit. on pp. 20, 101).

99. Schirotzek, A., Wu, C.-H., Sommer, A. & Zwierlein, M. W. Observation of Fermi Polarons in a Tunable Fermi Liquid of Ultracold Atoms. *Phys. Rev. Lett.* **102,** 230402 (2009) (cit. on pp. 20, 101, 112).

100. Yan, Z., Patel, P. B., Mukherjee, B., Fletcher, R. J., Struck, J. & Zwierlein, M. W. Boiling a Unitary Fermi Liquid. *Phys. Rev. Lett.* **122,** 093401 (2019) (cit. on p. 20).

101. Navon, N., Nascimbène, S., Chevy, F. & Salomon, C. The Equation of State of a Low-Temperature Fermi Gas with Tunable Interactions. *Science* **328,** 729–732 (2010) (cit. on p. 20).

102. Cetina, M., Jag, M., Lous, R. S., Fritsche, I., Walraven, J. T. M., Grimm, R., Levinsen, J., Parish, M. M., Schmidt, R., Knap, M. & Demler, E. Ultrafast Many-Body Interferometry of Impurities Coupled to a Fermi Sea. *Science* **354,** 96–99 (2016) (cit. on p. 20).

103. Ness, G., Shkedrov, C., Florshaim, Y., Diessel, O. K., von Milczewski, J., Schmidt, R. & Sagi, Y. Observation of a Smooth Polaron-Molecule Transition in a Degenerate Fermi Gas. *Phys. Rev. X* **10,** 041019 (2020) (cit. on pp. 20, 101, 109, 112).

104. Fritsche, I., Baroni, C., Dobler, E., Kirilov, E., Huang, B., Grimm, R., Bruun, G. M. & Massignan, P. Stability and Breakdown of Fermi Polarons in a Strongly Interacting Fermi-Bose Mixture. *Phys. Rev. A* **103,** 053314 (2021) (cit. on pp. 21, 101, 112).

105. Duda, M., Chen, X.-Y., Schindewolf, A., Bause, R., von Milczewski, J., Schmidt, R., Bloch, I. & Luo, X.-Y. *Transition from a Polaronic Condensate to a Degenerate Fermi Gas of Heteronuclear Molecules* 2021. arXiv: 2111.04301 (cit. on pp. 21, 35, 79, 95, 97, 99).

106. Powell, S., Sachdev, S. & Büchler, H. P. Depletion of the Bose-Einstein Condensate in Bose-Fermi Mixtures. *Phys. Rev. B* **72,** 024534 (2005) (cit. on pp. 21, 99, 101, 104, 109).

107. Fratini, E. & Pieri, P. Pairing and Condensation in a Resonant Bose-Fermi Mixture. *Phys. Rev. A* **81,** 051605 (2010) (cit. on pp. 21, 99, 101).

108. Ludwig, D., Floerchinger, S., Moroz, S. & Wetterich, C. Quantum Phase Transition in Bose-Fermi Mixtures. *Phys. Rev. A* **84,** 033629 (2011) (cit. on pp. 21, 22, 99, 101, 104, 112, 114).

109. Bertaina, G., Fratini, E., Giorgini, S. & Pieri, P. Quantum Monte Carlo Study of a Resonant Bose-Fermi Mixture. *Phys. Rev. Lett.* **110,** 115303 (2013) (cit. on pp. 21, 22, 101).

110. Guidini, A., Bertaina, G., Galli, D. E. & Pieri, P. Condensed Phase of Bose-Fermi Mixtures with a Pairing Interaction. *Phys. Rev. A* **91,** 023603 (2015) (cit. on pp. 21, 22, 99, 101, 104, 105, 107–109).

111. Buchheim, N. W. *Dual-species apparatus for creating a dipolar quantum gas of $^{23}Na^{40}K$ molecules* PhD thesis (Ludwig-Maximilians-Universität München, Munich, 2015) (cit. on pp. 23, 32).

112. Lu, Z. *Towards many body physics with ultracold NaK molecules* PhD thesis (Ludwig-Maximilians-Universität München, 2016) (cit. on p. 23).

113. Seeßelberg, F. *Interacting Gases of Ultracold Polar Molecules* PhD thesis (Ludwig-Maximilians-Universität München, Munich, 2019) (cit. on pp. 23, 79, 80, 82).

114. Colzi, G., Durastante, G., Fava, E., Serafini, S., Lamporesi, G. & Ferrari, G. Sub-Doppler Cooling of Sodium Atoms in Gray Molasses. *Phys. Rev. A* **93,** 023421 (2016) (cit. on p. 25).

115. Chu, S., Hollberg, L., Bjorkholm, J. E., Cable, A. & Ashkin, A. Three-Dimensional Viscous Confinement and Cooling of Atoms by Resonance Radiation Pressure. *Phys. Rev. Lett.* **55,** 48–51 (1985) (cit. on p. 25).

116. Steck, D. *Sodium D Line Data* (Accessed on 2022-03-23). https://steck.us/alkalidata/sodiumnumbers.pdf (cit. on pp. 28, 35, 40, 51, 65).

117. Tiecke, T. G. *Properties of Potassium* (Accessed on 2022-03-23). https://www.tobiastiecke.nl/archive/PotassiumProperties.pdf (cit. on pp. 28, 40, 51, 65).

118. Vexiau, R., Borsalino, D., Lepers, M., Orbán, A., Aymar, M., Dulieu, O. & Bouloufa-Maafa, N. Dynamic Dipole Polarizabilities of Heteronuclear Alkali Dimers: Optical Response, Trapping and Control of Ultracold Molecules. *Int. Rev. Phys. Chem.* **36,** 709–750 (2017) (cit. on pp. 28, 29, 34, 35).

119. Bouloufa-Maafa, N. Private Communication (2019) (cit. on pp. 29, 36).

120. Greiner, M., Bloch, I., Hänsch, T. W. & Esslinger, T. Magnetic Transport of Trapped Cold Atoms over a Large Distance. *Phys. Rev. A* **63,** 031401 (2001) (cit. on p. 29).

121. Lewandowski, H. J., Harber, D. M., Whitaker, D. L. & Cornell, E. A. Simplified System for Creating a Bose–Einstein Condensate. *J. Low Temp. Phys.* **132,** 309–367 (2003) (cit. on p. 29).

122. Gustavson, T. L., Chikkatur, A. P., Leanhardt, A. E., Görlitz, A., Gupta, S., Pritchard, D. E. & Ketterle, W. Transport of Bose-Einstein Condensates with Optical Tweezers. *Phys. Rev. Lett.* **88,** 020401 (2001) (cit. on p. 29).

123. Couvert, A., Kawalec, T., Reinaudi, G. & Guéry-Odelin, D. Optimal Transport of Ultracold Atoms in the Non-Adiabatic Regime. *Europhys. Lett.* **83,** 13001 (2008) (cit. on p. 29).

124. Zimmermann, B., Müller, T., Meineke, J., Esslinger, T. & Moritz, H. High-Resolution Imaging of Ultracold Fermions in Microscopically Tailored Optical Potentials. *New J. Phys.* **13,** 043007 (2011) (cit. on p. 29).

125. Léonard, J., Lee, M., Morales, A., Karg, T. M., Esslinger, T. & Donner, T. Optical Transport and Manipulation of an Ultracold Atomic Cloud Using Focus-Tunable Lenses. *New J. Phys.* **16,** 093028 (2014) (cit. on p. 29).

126. Schmid, S., Thalhammer, G., Winkler, K., Lang, F. & Denschlag, J. H. Long Distance Transport of Ultracold Atoms Using a 1D Optical Lattice. *New J. Phys.* **8,** 159–159 (2006) (cit. on p. 29).

127. Middelmann, T., Falke, S., Lisdat, C. & Sterr, U. Long-Range Transport of Ultracold Atoms in a Far-Detuned One-Dimensional Optical Lattice. *New J. Phys.* **14,** 073020 (2012) (cit. on p. 29).

128. Klostermann, T., Cabrera, C. R., von Raven, H., Wienand, J. F., Schweizer, C., Bloch, I. & Aidelsburger, M. Fast Long-Distance Transport of Cold Cesium Atoms. *Phys. Rev. A* **105,** 043319 (2022) (cit. on p. 29).

129. Gross, C., Gan, H. C. J. & Dieckmann, K. All-Optical Production and Transport of a Large ^{6}Li Quantum Gas in a Crossed Optical Dipole Trap. *Phys. Rev. A* **93,** 053424 (2016) (cit. on p. 29).

130. Eustice, S. *Ultracold NaK Molecules in a 3D Optical Lattice* MA thesis (Ludwig-Maximilians-Universität München, Munich) (cit. on p. 29).

131. Ippen, E. & Stolen, R. Stimulated Brillouin Scattering in Optical Fibers. *Appl. Phys. Lett.* **21,** 539–541 (1972) (cit. on p. 30).

132. Moses, S. A., Covey, J. P., Miecnikowski, M. T., Jin, D. S. & Ye, J. New Frontiers for Quantum Gases of Polar Molecules. *Nat. Phys.* **13,** 13–20 (2017) (cit. on p. 33).

133. Aymar, M. & Dulieu, O. Calculations of Transition and Permanent Dipole Moments of Heteronuclear Alkali Dimers NaK, NaRb and NaCs. *Mol. Phys.* **105,** 1733–1742 (2007) (cit. on p. 35).

134. Park, J. W., Will, S. A. & Zwierlein, M. W. Two-Photon Pathway to Ultracold Ground State Molecules of ^{23}Na^{40}K. *New J. Phys.* **17,** 075016 (2015) (cit. on pp. 35, 36).

135. Demtröder, W. *Molekülphysik: Theoretische Grundlagen und experimentelle Methoden* (Oldenbourg Wissenschaftsverlag, 2013) (cit. on p. 35).

136. Tao, R. *Near-Resonant Dipole Traps and Lattices for Ultracold Molecules* MA thesis (Ludwig-Maximilians-Universität München, Munich) (cit. on p. 37).

137. Bause, R., Schindewolf, A., Tao, R., Duda, M., Chen, X.-Y., Quéméner, G., Karman, T., Christianen, A., Bloch, I. & Luo, X.-Y. Collisions of Ultracold Molecules in Bright and Dark Optical Dipole Traps. *Phys. Rev. Res.* **3,** 033013 (2021) (cit. on pp. 37, 70, 72, 74).

138. Reinaudi, G., Lahaye, T., Wang, Z. & Guéry-Odelin, D. Strong Saturation Absorption Imaging of Dense Clouds of Ultracold Atoms. *Opt. Lett.* **32,** 3143–3145 (2007) (cit. on p. 39).

139. Dürr, S., Volz, T. & Rempe, G. Dissociation of Ultracold Molecules with Feshbach Resonances. *Phys. Rev. A* **70,** 031601 (2004) (cit. on p. 43).

140. Szczepkowski, J., Gartman, R., Witkowski, M., Tracewski, L., Zawada, M. & Gawlik, W. Analysis and Calibration of Absorptive Images of Bose-Einstein Condensate at Nonzero Temperatures. *Rev. Sci. Instrum.* **80,** 053103 (2009) (cit. on p. 43).

141. Schindewolf, A., Bause, R., Chen, X.-Y., Duda, M., Karman, T., Bloch, I. & Luo, X.-Y. *Evaporation of Microwave-Shielded Polar Molecules to Quantum Degeneracy* 2022. arXiv: 2201.05143 (cit. on pp. 44, 96, 114).

142. Valtolina, G., Matsuda, K., Tobias, W. G., Li, J.-R., De Marco, L. & Ye, J. Dipolar Evaporation of Reactive Molecules to below the Fermi Temperature. *Nature* **588,** 239–243 (2020) (cit. on pp. 45, 79).

143. Chen, X.-Y., Duda, M., Schindewolf, A., Bause, R., Bloch, I. & Luo, X.-Y. Suppression of Unitary Three-Body Loss in a Degenerate Bose-Fermi Mixture. *Phys. Rev. Lett.* **128,** 153401 (2022) (cit. on pp. 46, 49, 53, 102).

144. Park, J. W., Wu, C.-H., Santiago, I., Tiecke, T. G., Will, S., Ahmadi, P. & Zwierlein, M. W. Quantum Degenerate Bose-Fermi Mixture of Chemically Different Atomic Species with Widely Tunable Interactions. *Phys. Rev. A* **85,** 051602 (2012) (cit. on p. 46).

145. Breit, G. & Rabi, I. I. Measurement of Nuclear Spin. *Phys. Rev.* **38,** 2082–2083 (1931) (cit. on pp. 46, 51).

146. Klempt, C., Henninger, T., Topic, O., Scherer, M., Kattner, L., Tiemann, E., Ertmer, W. & Arlt, J. J. Radio-Frequency Association of Heteronuclear Feshbach Molecules. *Phys. Rev. A* **78,** 061602 (2008) (cit. on p. 46).

147. Chin, C. & Julienne, P. S. Radio-Frequency Transitions on Weakly Bound Ultracold Molecules. *Phys. Rev. A* **71,** 012713 (2005) (cit. on p. 47).

148. Lange, A. D., Pilch, K., Prantner, A., Ferlaino, F., Engeser, B., Nägerl, H.-C., Grimm, R. & Chin, C. Determination of Atomic Scattering Lengths from Measurements of Molecular Binding Energies near Feshbach Resonances. *Phys. Rev. A* **79,** 013622 (2009) (cit. on pp. 47, 49).

149. Tiemann, E. Private Communication (2019) (cit. on p. 49).

150. Duda, M., Chen, X.-Y., Bause, R., Schindewolf, A., Bloch, I. & Luo, X.-Y. *Long-Lived Fermionic Feshbach Molecules with Tunable* p*-Wave Interactions* 2022. arXiv: 2202.06940 (cit. on p. 53).

151. Weber, T., Herbig, J., Mark, M., Nägerl, H.-C. & Grimm, R. Three-Body Recombination at Large Scattering Lengths in an Ultracold Atomic Gas. *Phys. Rev. Lett.* **91,** 123201 (2003) (cit. on p. 54).

152. Helfrich, K., Hammer, H.-W. & Petrov, D. S. Three-Body Problem in Heteronuclear Mixtures with Resonant Interspecies Interaction. *Phys. Rev. A* **81,** 042715 (2010) (cit. on pp. 55, 57, 59, 66).

153. Bloom, R. S., Hu, M.-G., Cumby, T. D. & Jin, D. S. Tests of Universal Three-Body Physics in an Ultracold Bose-Fermi Mixture. *Phys. Rev. Lett.* **111,** 105301 (2013) (cit. on pp. 56, 87).

154. Luiten, O. J., Reynolds, M. W. & Walraven, J. T. M. Kinetic Theory of the Evaporative Cooling of a Trapped Gas. *Phys. Rev. A* **53,** 381–389 (1996) (cit. on p. 57).

155. Eismann, U., Khaykovich, L., Laurent, S., Ferrier-Barbut, I., Rem, B. S., Grier, A. T., Delehaye, M., Chevy, F., Salomon, C., Ha, L. C. & Chin, C. Universal Loss Dynamics in a Unitary Bose Gas. *Phys. Rev. X* **6,** 021025 (2016) (cit. on pp. 57, 60).

156. Mosk, A., Kraft, S., Mudrich, M., Singer, K., Wohlleben, W., Grimm, R. & Weidemüller, M. Mixture of Ultracold Lithium and Cesium Atoms in an Optical Dipole Trap. *Appl. Phys. B* **73,** 791–799 (2001) (cit. on p. 57).

157. Petrov, D. S. & Werner, F. Three-Body Recombination in Heteronuclear Mixtures at Finite Temperature. *Phys. Rev. A* **92,** 022704 (2015) (cit. on pp. 57, 59).

158. Greene, C. H., Esry, B. D. & Suno, H. A Revised Formula for 3-Body Recombination That Cannot Exceed the Unitarity Limit. *Nucl. Phys. A* **737,** 119–124 (2004) (cit. on p. 59).

159. Wang, Y. & Julienne, P. S. Universal van Der Waals Physics for Three Cold Atoms near Feshbach Resonances. *Nat. Phys.* **10,** 768–773 (2014) (cit. on p. 60).

160. Langmack, C., Schmidt, R. & Zwerger, W. Efimov States near a Feshbach Resonance and the Limits of van Der Waals Universality at Finite Background Scattering Length. *Phys. Rev. A* **97,** 033623 (2018) (cit. on p. 60).

161. Pricoupenko, A. & Petrov, D. S. Three-Body Interaction near a Narrow Two-Body Zero Crossing. *Phys. Rev. A* **100,** 042707 (2019) (cit. on p. 60).

162. Ulmanis, J., Häfner, S., Pires, R., Werner, F., Petrov, D. S., Kuhnle, E. D. & Weidemüller, M. Universal Three-Body Recombination and Efimov Resonances in an Ultracold Li-Cs Mixture. *Phys. Rev. A* **93,** 022707 (2016) (cit. on p. 60).

163. Burt, E. A., Ghrist, R. W., Myatt, C. J., Holland, M. J., Cornell, E. A. & Wieman, C. E. Coherence, Correlations, and Collisions: What One Learns about Bose-Einstein Condensates from Their Decay. *Phys. Rev. Lett.* **79,** 337–340 (1997) (cit. on p. 60).

164. Söding, J., Guéry-Odelin, D., Desbiolles, P., Chevy, F., Inamori, H. & Dalibard, J. Three-Body Decay of a Rubidium Bose–Einstein Condensate. *Appl. Phys. B* **69,** 257–261 (1999) (cit. on p. 60).

165. Haller, E., Rabie, M., Mark, M. J., Danzl, J. G., Hart, R., Lauber, K., Pupillo, G. & Nägerl, H.-C. Three-Body Correlation Functions and Recombination Rates for Bosons in Three Dimensions and One Dimension. *Phys. Rev. Lett.* **107,** 230404 (2011) (cit. on p. 60).

166. Ottenstein, T. B., Lompe, T., Kohnen, M., Wenz, A. N. & Jochim, S. Collisional Stability of a Three-Component Degenerate Fermi Gas. *Phys. Rev. Lett.* **101,** 203202 (2008) (cit. on p. 60).

167. Huckans, J. H., Williams, J. R., Hazlett, E. L., Stites, R. W. & O'Hara, K. M. Three-Body Recombination in a Three-State Fermi Gas with Widely Tunable Interactions. *Phys. Rev. Lett.* **102,** 165302 (2009) (cit. on p. 60).

168. DeSalvo, B. J., Patel, K., Cai, G. & Chin, C. Observation of Fermion-Mediated Interactions between Bosonic Atoms. *Nature* **568,** 61–64 (2019) (cit. on pp. 63, 64).

169. Edri, H., Raz, B., Matzliah, N., Davidson, N. & Ozeri, R. Observation of Spin-Spin Fermion-Mediated Interactions between Ultracold Bosons. *Phys. Rev. Lett.* **124,** 163401 (2020) (cit. on pp. 63, 64).

170. Ruderman, M. A. & Kittel, C. Indirect Exchange Coupling of Nuclear Magnetic Moments by Conduction Electrons. *Phys. Rev.* **96,** 99–102 (1954) (cit. on p. 63).

171. De, S. & Spielman, I. B. Fermion-Mediated Long-Range Interactions between Bosons Stored in an Optical Lattice. *Appl. Phys. B* **114,** 527–536 (2014) (cit. on p. 63).

172. MacNeill, D. J. & Zhou, F. Pauli Blocking Effect on Efimov States near a Feshbach Resonance. *Phys. Rev. Lett.* **106,** 145301 (2011) (cit. on p. 63).

173. Quéméner, G. *Ultracold Collisions of Molecules* 2017. arXiv: 1703.09174 (cit. on p. 64).

174. Petrov, D. S. Private Communication (2020) (cit. on p. 66).

175. Huang, B., O'Hara, K. M., Grimm, R., Hutson, J. M. & Petrov, D. S. Three-Body Parameter for Efimov States in ^{6}Li. *Phys. Rev. A* **90,** 043636 (2014) (cit. on p. 66).

176. Köhler, T., Góral, K. & Julienne, P. S. Production of Cold Molecules via Magnetically Tunable Feshbach Resonances. *Rev. Mod. Phys.* **78,** 1311–1361 (2006) (cit. on pp. 67, 68, 79).

177. Zirbel, J. J., Ni, K.-K., Ospelkaus, S., D'Incao, J. P., Wieman, C. E., Ye, J. & Jin, D. S. Collisional Stability of Fermionic Feshbach Molecules. *Phys. Rev. Lett.* **100,** 143201 (2008) (cit. on pp. 68, 87, 113).

178. Wu, C.-H., Park, J. W., Ahmadi, P., Will, S. & Zwierlein, M. W. Ultracold Fermionic Feshbach Molecules of ^{23}Na^{40}K. *Phys. Rev. Lett.* **109,** 085301 (2012) (cit. on pp. 68, 79, 80).

179. Heo, M.-S., Wang, T. T., Christensen, C. A., Rvachov, T. M., Cotta, D. A., Choi, J.-H., Lee, Y.-R. & Ketterle, W. Formation of Ultracold Fermionic NaLi Feshbach Molecules. *Phys. Rev. A* **86,** 021602 (2012) (cit. on p. 68).

180. Ni, K.-K., Ospelkaus, S., Wang, D., Quéméner, G., Neyenhuis, B., de Miranda, M. H. G., Bohn, J. L., Ye, J. & Jin, D. S. Dipolar Collisions of Polar Molecules in the Quantum Regime. *Nature* **464,** 1324–1328 (2010) (cit. on pp. 70, 74, 75).

181. Ospelkaus, S., Ni, K.-K., Wang, D., de Miranda, M. H. G., Neyenhuis, B., Quéméner, G., Julienne, P. S., Bohn, J. L., Jin, D. S. & Ye, J. Quantum-State Controlled Chemical Reactions of Ultracold Potassium-Rubidium Molecules. *Science* **327,** 853–857 (2010) (cit. on pp. 72, 104).

182. Hudson, E. R., Gilfoy, N. B., Kotochigova, S., Sage, J. M. & DeMille, D. Inelastic Collisions of Ultracold Heteronuclear Molecules in an Optical Trap. *Phys. Rev. Lett.* **100,** 203201 (2008) (cit. on p. 72).

183. Derevianko, A., Babb, J. F. & Dalgarno, A. High-Precision Calculations of van Der Waals Coefficients for Heteronuclear Alkali-Metal Dimers. *Phys. Rev. A* **63,** 052704 (2001) (cit. on p. 72).

184. Mitroy, J. & Bromley, M. W. J. Semiempirical Calculation of van Der Waals Coefficients for Alkali-Metal and Alkaline-Earth-Metal Atoms. *Phys. Rev. A* **68,** 052714 (2003) (cit. on p. 72).

185. Ferlaino, F., Knoop, S., Mark, M., Berninger, M., Schöbel, H., Nägerl, H.-C. & Grimm, R. Collisions between Tunable Halo Dimers: Exploring an Elementary Four-Body Process with Identical Bosons. *Phys. Rev. Lett.* **101,** 023201 (2008) (cit. on p. 72).

186. Jag, M., Cetina, M., Lous, R. S., Grimm, R., Levinsen, J. & Petrov, D. S. Lifetime of Feshbach Dimers in a Fermi-Fermi Mixture of ^{6}Li and ^{40}K. *Phys. Rev. A* **94,** 062706 (2016) (cit. on p. 72).

187. Bause, R. *Understanding and Controlling the Collisions of Ultracold Molecules* PhD thesis (Ludwig-Maximilians-Universität München, Munich) (cit. on pp. 74, 96).

188. Julienne, P. S., Hanna, T. M. & Idziaszek, Z. Universal Ultracold Collision Rates for Polar Molecules of Two Alkali-Metal Atoms. *Phys. Chem. Chem. Phys.* **13,** 19114–19124 (2011) (cit. on p. 74).

189. Ma, Z.-Y., Thomas, A. M., Foot, C. J. & Cornish, S. L. The Evaporative Cooling of a Gas of Caesium Atoms in the Hydrodynamic Regime. *J. Phys. B: At. Mol. Opt. Phys.* **36,** 3533–3540 (2003) (cit. on p. 75).

190. Matsuda, K., De Marco, L., Li, J.-R., Tobias, W. G., Valtolina, G., Quéméner, G. & Ye, J. Resonant Collisional Shielding of Reactive Molecules Using Electric Fields. *Science* **370,** 1324–1327 (2020) (cit. on p. 79).

191. Li, J.-R., Tobias, W. G., Matsuda, K., Miller, C., Valtolina, G., De Marco, L., Wang, R. R. W., Lassablière, L., Quéméner, G., Bohn, J. L. & Ye, J. Tuning of Dipolar Interactions and Evaporative Cooling in a Three-Dimensional Molecular Quantum Gas. *Nat. Phys.* **17,** 1144–1148 (2021) (cit. on p. 79).

192. Yamakoshi, T., Watanabe, S., Zhang, C. & Greene, C. H. Stochastic and Equilibrium Pictures of the Ultracold Fano-Feshbach-resonance Molecular Conversion Rate. *Phys. Rev. A* **87,** 053604 (2013) (cit. on p. 79).

193. Mies, F. H., Tiesinga, E. & Julienne, P. S. Manipulation of Feshbach Resonances in Ultracold Atomic Collisions Using Time-Dependent Magnetic Fields. *Phys. Rev. A* **61,** 022721 (2000) (cit. on p. 80).

194. Góral, K., Köhler, T., Gardiner, S. A., Tiesinga, E. & Julienne, P. S. Adiabatic Association of Ultracold Molecules via Magnetic-Field Tunable Interactions. *J. Phys. B: At. Mol. Opt. Phys.* **37,** 3457–3500 (2004) (cit. on p. 80).

195. Zaccanti, M. Private Communication (2022) (cit. on p. 89).

196. Bause, R., Kamijo, A., Chen, X.-Y., Duda, M., Schindewolf, A., Bloch, I. & Luo, X.-Y. Efficient Conversion of Closed-Channel-Dominated Feshbach Molecules of ^{23}Na^{40}K to Their Absolute Ground State. *Phys. Rev. A* **104,** 043321 (2021) (cit. on p. 91).

197. Tobias, W. G., Matsuda, K., Valtolina, G., De Marco, L., Li, J.-R. & Ye, J. Thermalization and Sub-Poissonian Density Fluctuations in a Degenerate Molecular Fermi Gas. *Phys. Rev. Lett.* **124,** 033401 (2020) (cit. on pp. 93, 94, 96, 110).

198. Sanner, C., Su, E. J., Keshet, A., Gommers, R., Shin, Y.-i., Huang, W. & Ketterle, W. Suppression of Density Fluctuations in a Quantum Degenerate Fermi Gas. *Phys. Rev. Lett.* **105,** 040402 (2010) (cit. on p. 94).

199. Anderegg, L., Burchesky, S., Bao, Y., Yu, S. S., Karman, T., Chae, E., Ni, K.-K., Ketterle, W. & Doyle, J. M. Observation of Microwave Shielding of Ultracold Molecules. *Science* **373,** 779–782 (2021) (cit. on p. 96).

200. Sidler, M., Back, P., Cotlet, O., Srivastava, A., Fink, T., Kroner, M., Demler, E. & Imamoglu, A. Fermi Polaron-Polaritons in Charge-Tunable Atomically Thin Semiconductors. *Nat. Phys.* **13,** 255–261 (2017) (cit. on p. 99).

201. Mak, K. F., He, K., Lee, C., Lee, G. H., Hone, J., Heinz, T. F. & Shan, J. Tightly Bound Trions in Monolayer MoS_2. *Nat. Mater.* **12,** 207–211 (2013) (cit. on p. 99).

202. Matuszewski, M., Taylor, T. & Kavokin, A. V. Exciton Supersolidity in Hybrid Bose-Fermi Systems. *Phys. Rev. Lett.* **108,** 060401 (2012) (cit. on pp. 99, 100).

203. Shelykh, I. A., Taylor, T. & Kavokin, A. V. Rotons in a Hybrid Bose-Fermi System. *Phys. Rev. Lett.* **105,** 140402 (2010) (cit. on pp. 99, 100).

204. Cotleţ, O., Zeytinoğlu, S., Sigrist, M., Demler, E. & Imamoğlu, A. Superconductivity and Other Collective Phenomena in a Hybrid Bose-Fermi Mixture Formed by a Polariton Condensate and an Electron System in Two Dimensions. *Phys. Rev. B* **93,** 054510 (2016) (cit. on pp. 99, 100).

205. Suzuki, K., Miyakawa, T. & Suzuki, T. *p*-Wave Superfluid and Phase Separation in Atomic Bose-Fermi Mixtures. *Phys. Rev. A* **77,** 043629 (2008) (cit. on p. 99).

206. Laussy, F. P., Kavokin, A. V. & Shelykh, I. A. Exciton-Polariton Mediated Superconductivity. *Phys. Rev. Lett.* **104,** 106402 (2010) (cit. on pp. 99, 100).

207. Camacho-Guardian, A., Peña Ardila, L. A., Pohl, T. & Bruun, G. M. Bipolarons in a Bose-Einstein Condensate. *Phys. Rev. Lett.* **121,** 013401 (2018) (cit. on p. 100).

208. Hu, M.-G., Van de Graaff, M. J., Kedar, D., Corson, J. P., Cornell, E. A. & Jin, D. S. Bose Polarons in the Strongly Interacting Regime. *Phys. Rev. Lett.* **117,** 055301 (2016) (cit. on p. 101).

209. Yan, Z. Z., Ni, Y., Robens, C. & Zwierlein, M. W. Bose Polarons near Quantum Criticality. *Science* **368,** 190–194 (2020) (cit. on p. 101).

210. von Milczewski, J., Durst, A. & Schmidt, R. Fermi Polaron Lifetimes at Finite Momentum from a Functional-Renormalization-Group Approach (in preparation) (cit. on p. 105).

211. Prokof'ev, N. & Svistunov, B. Fermi-Polaron Problem: Diagrammatic Monte Carlo Method for Divergent Sign-Alternating Series. *Phys. Rev. B* **77,** 020408 (2008) (cit. on p. 105).

212. Bogolubov, N. On the Theory of Superfluidity. *J. Phys.* **11,** 23–32 (1947) (cit. on p. 108).

213. Parish, M. M., Adlong, H. S., Liu, W. E. & Levinsen, J. Thermodynamic Signatures of the Polaron-Molecule Transition in a Fermi Gas. *Phys. Rev. A* **103,** 023312 (2021) (cit. on p. 109).

214. Greiner, M., Mandel, O., Esslinger, T., Hänsch, T. W. & Bloch, I. Quantum Phase Transition from a Superfluid to a Mott Insulator in a Gas of Ultracold Atoms. *Nature* **415,** 39–44 (2002) (cit. on p. 112).

215. Trotzky, S., Pollet, L., Gerbier, F., Schnorrberger, U., Bloch, I., Prokof'ev, N. V., Svistunov, B. & Troyer, M. Suppression of the Critical Temperature for Superfluidity near the Mott Transition. *Nat. Phys.* **6,** 998–1004 (2010) (cit. on p. 112).

216. Witczak-Krempa, W., Sørensen, E. S. & Sachdev, S. The Dynamics of Quantum Criticality Revealed by Quantum Monte Carlo and Holography. *Nature Phys* **10,** 361–366 (2014) (cit. on p. 114).

217. Miyakawa, T., Sogo, T. & Pu, H. Phase-Space Deformation of a Trapped Dipolar Fermi Gas. *Phys. Rev. A* **77,** 061603 (2008) (cit. on p. 114).

218. Aikawa, K., Baier, S., Frisch, A., Mark, M., Ravensbergen, C. & Ferlaino, F. Observation of Fermi Surface Deformation in a Dipolar Quantum Gas. *Science* **345,** 1484–1487 (2014) (cit. on p. 114).

219. Kwasigroch, M. P. & Cooper, N. R. Bose-Einstein Condensation and Many-Body Localization of Rotational Excitations of Polar Molecules Following a Microwave Pulse. *Phys. Rev. A* **90,** 021605 (2014) (cit. on p. 114).

220. Kwasigroch, M. P. & Cooper, N. R. Synchronization Transition in Dipole-Coupled Two-Level Systems with Positional Disorder. *Phys. Rev. A* **96,** 053610 (2017) (cit. on p. 114).

221. Lassablière, L. & Quéméner, G. Controlling the Scattering Length of Ultracold Dipolar Molecules. *Phys. Rev. Lett.* **121,** 163402 (2018) (cit. on p. 114).

Acknowledgments

I have had a great time during my Ph.D., met interesting people, went through very difficult times, and also had a lot of fun. Luckily, I was never alone and could share my troubles and successes with an awesome team and a great group. I want to start thanking the (former) members of the Molecules lab:

Roman, thank you for being my brother-in-science and friend. You accompanied me through the Ph.D. from day one. Together, we struggled with the machine, cursed at it and fixed it until it broke again. During all this time, I could rely on you, ask for help and get your mental support when it was needed most. I am really thankful for all the advice and discussions that often started with the two words "Roman, question." I hope that your future plans will work out but actually I am sure. Since I never said it in words, let me say it on paper but don't get cocky: You are the best all-rounder physicist that I have ever met!

Xingyan, you came as a theoretician and grew to become a master of the machine. Thank you for the great time we had in the lab together. We shared a lot of difficult and frustrating moments while trying to repeatedly measure all kinds of losses. One very memorable moment is the day, when we were measuring three-body loss for almost twenty-four hours, and because I was so tired, you suggested that we would do some Tai chi to stay awake. During all the time we worked together, I have learned a lot from you because honestly, deep in your heart, there is still a little theoretician. I admire that you understand complex physical phenomena in no time with such ease. For the rest of the Ph.D., I hope that you don't have to suffer anymore. Good luck and all the best for the future.

Andreas, you have eyes for the details and you are the person of wisdom. I have learned a lot from you on all kinds of topics. You have the ability to spot the misconceptions and the patience to explain the right picture. Importantly, let us not forget the great time we had climbing. I wish you all the best for the future, and hope to read about the Schindewolf-resonance at some point.

Xinyu, my Sensei, the man of the thousand plans. Thank you for letting me join the molecules lab and being part of this success story, and always believing in me. As Roman said in his acknowledgments, you are the visionary of the team and I can only agree with that. You have been of great help throughout my Ph.D., no matter the time of day. You are the devil on my shoulder who says "Are you sure the data is consistent? How about this point? Try to think about this!", and as often as I got annoyed with you or disagreed with you, in retrospect, ... and it is hard to admit ... you were always right! I started working with you shortly after you became the PI in the molecules lab, and I think you have by now become an old driver at this! Good job, continue!

Sebb, thank you for being such a team player. From day one, you kept your eyes open for projects to help others and were always involved. I think that as the "new computer guy" you will be very valuable to the lab. Together with ...

Shreshta, you will have great opportunities in the lab. I wish you all the best for the future in progressing the molecules lab.

Benedikt, you are more of a molecule than most of us. You have started to work in our lab on a frustrating project, and still, you crazy person came back to us, and luckily so. You had your hands in so many projects, may it be the STIRAP, high voltage amplifiers, the DMD project, and who knows what I forgot. I hope that you will have a great Ph.D. in Amsterdam, they are lucky to have such a dedicated student! By the way, did you find a place that sells Brezen and Spezi?

Immanuel, thank you for all the support I have received from you, for example, when the K-Rydberg lab moved to Tübingen. The day I wanted to ask you whether I could continue in Munich, I came to your office three times and turned around midway because I thought this would be a "difficult" discussion. Instead, you welcomed me and granted me the wish to join the molecules. Also, thank you for having our back in difficult times, showing me that you care about us as a team and also for us as individuals!

Next, I would like to thank the QPT-team Richard and Jonas. Without you guys, we would have still been in the dark about the molecule-formation process. You taught us how to think about it the many-body way and I am happy that you did! Richard, thanks for the nightly calls we had before the submission of the paper and the time you invested in this project. A special thanks goes to Jonas for answering all the stupid experimenter questions about polarons and computational methods. Every time I had a question and expected a short answer, you took the time to explain to me whatever I wanted to know. The words "Puhhhh, gute Frage" were followed by several paragraphs with detailed information. Also, thanks for the positivity and the commitment to the QPT paper.

Next, I would like to thank the Bloch group. Special thanks goes to Sarah Hirthe for baby-sitting Livi, reading my thesis and emotional support. Thanks to Simon Hollerith for being my former homework buddy and getting me into the ultracold-atoms field. Thanks to all members of "Quantum Pogodynamics" for the great time we had playing music and releasing aggression doing so. Thanks to Niko, Kathrin and Jonas for reading my thesis, job advice, climbing and companionship. Thanks, Jan Trautmann, for reading my thesis and co-tutoring Quantum Optics 2 with me, and special thanks to his girlfriend Sarah Neumahr for assisting in bringing Livi to this world.

I would like to dedicate this section to the people that make sure that everything at MPQ works and nothing collapses. First, Ildiko Kecskesi, Doreen Seidl and of course Kristina Schuldt, for the support with any administrative problems but also the emotional support that you give us as Ph.D. students. Next, I would like to thank Karsten, Olivia and Anton for all the technical support. Special thanks goes to Anton for the day-to-day advice also on things outside of work like Einbauspülmaschinen.

Outside of MPQ, I would like to thank Christian Groß for having been a great supervisor during my time as Ph.D. student in the K-Rydberg lab, Dmitry Petrov for the discussions on few-body physics, Pierbiagio Pieri for the discussions on the polaron-to-molecule transition, the dipolar quantum gases team in Innsbruck for hosting me.

Next up, my family. I would like to thank my parents for their life-long support of my choices irrespective of whether you agreed or not. I would like to thank my parents-in-law

for taking care of Livi even shortly before the submission. I would like to thank my big sister Patrizia for the needed perspective in the difficult moments of my Ph.D., and her husband Voni for the “No-nonsense woodwork for exhausted physicists”.

Second to last and surely not least, I want to thank my wife Denise for her continuous support. She has truly seen the worst of me when I had doubts about myself, my choices, faced setbacks and all the other experiences a Ph.D. entails. She endured it and supported me within the chaos of a small household with a talkative cat and a baby that has tooth pain, development boosts and 1-millihertz-frequency mood swings. Thank you for all of this, I love you!

I also thank Livi-Asafine-Piranha for the constant distractions.